UNIVERSITY OF LEICESTER

Characterisation of fluorescence imaging and silicon photomultiplier based gamma camera

A thesis submitted for the degree of

Doctor of Philosophy

by

Awad Mohammed Almarhaby

Space Research Centre

Department of Physics and Astronomy

February 2021

Characterisation of fluorescence imaging and silicon photomultiplier based gamma camera

Awad Mohammed Almarhaby

Abstract

To date, surgery is the most common method to treat cancer. Complete tumour resection, however, can be challenging as it relies on the surgeon's ability to visually discriminate healthy from diseased tissues. Additional contrast mechanisms are needed to further guide cancer identification during surgery.

Small field of view (SFOV) gamma imaging has been widely introduced for image-guided cancer surgery. A novel SFOV hybrid gamma camera (HGC) has been developed, at the University of Leicester, that is capable of providing co-aligned images from optical and gamma modalities simultaneously. The HGC has the potential to enhance tumour localisation intraoperatively.

In this thesis, a dedicated near infrared fluorescence imaging (NIRFI) systems have been characterised for combination with the HGC. The performance of two NIRF imaging systems using phantom studies, various fluorophores and different experimental configurations was evaluated. Bespoke lymph node phantoms simulating metastases and tissue-like layers were constructed to evaluate the detection capability. The threshold detectable concentration of both dyes were investigated for both systems. The maximum depth at which NIRF targets could be distinguished was determined for both systems.

Silicon photomultiplier (SiPM) is a novel photon sensing device, with potential applications in medical gamma imaging. This thesis also characterised different parameters of the SiPM under different operating conditions. Better knowledge of the SiPM technology was obtained to exploit its advantages in an introperative SFOV gamma imaging system.

This work also reported the performance of gamma detectors comprising SiPM detector optically coupled to a monolithic GAGG:Ce and a columnar CsI:TI scintillators. A thin layer of both scintillators was investigated in order to determine their performance features such as linearity, intrinsic energy resolution and detection efficiency when combined to a SiPM.

Acknowledgements

There are many great people who I would like to thank for their support throughout my PhD studies. First and foremost I am extremely grateful to my supervisors, Prof John Lees and Dr Sarah Bugby who provided me an opportunity to join the BioImaging Unit. I have found John to be lively, enthusiastic and supportive. His immense knowledge and plentiful experience have encouraged me in all the time of my academic research and daily life. Sarah has been supportive and has given me the freedom to pursue various projects and provided me with many insightful discussions and suggestions. Her comprehensive view and strong scientific background helped me to broaden my horizon in various fields. I am enormously thankful to both John and Sarah for believing in my capabilities and for their continuous support throughout my journey.

Equally important, I would like to express my sincere gratitude to Prof Jon Lapington who has taken over supervision of my scholarship. I will forever be thankful to him for his immense enthusiasm and knowledge, for having taught me how good research is done and for his contagious passion for science. I also would like to thank Dr Steve Leach for his invariably generous help, deep insights, wise and experienced advice in all the scientific and technical aspects.

My gratitude extends to Prof Alan Perkins for his invaluable suggestions, continuous support and great guidance. His comprehensive knowledge and long experience in medical physics field helped me to expand my vision during this research opportunity.

I would like to acknowledge all my colleagues (present and former) who supported me throughout this journey. A special thank goes to Dr Mohammed Alqahtani for his terrific help and support before and during my study. Thank you for being such great colleague and, most importantly, devoted friend. Particular thanks are extended to my officemate, Kjell Koch-Mehrin who has been

supportive friend during our PhD studies. I also would like to thank Angaraj Duara, Connor Duffy, Duncan Ross, Dr Layal Jambi, Bill McKnight, Dr Simon Lindsay, Dr Numan Dawood, Dr Aik Ng, Dr Bahadar Bhatia, Dr John Pearl and John Holt.

I am forever indebted to my parents for giving me the opportunities and experiences that have made me who I am. They selflessly encouraged me to explore new directions in life and seek my own destiny. This journey would not have been possible if not for them, and I dedicate this milestone to them. Special thanks and sincere appreciation are reserved to my brothers, sisters and cousins for their endless encouragement and support during this long journey away from home. I am enormously grateful to my cousin Eng Ahmed Almarhaby, for his continuous and unparalleled help and support. I will forever be thankful to him for his immense and kind encouragement.

Last, but by no means least, I must express my very profound gratitude to my wife, Sarah, who experienced all of the ups and downs of my research. Thank you for your love, patience, care, affection and encouragement in all the time. Without you, I would not be where I am today. To my great girls, Rania and Fatimah you are my inspiration in this life to achieve greatness.

Contents

Publications

Algarni H, Alqahtani MS, **Almarhaby AM**, Hussein KI, Yasmeen KY, Almohiy H, Yaha IS and El Sayed Y. An estimation of the radiation protection properties of the fluoride-phosphate-tellurite glass with composition: $40P_2O_5$-30ZnO-$20BaF_2$-$3.8K_2TeO_3$-$1.2Al_2O_3$-$5Nb_2O_5$-3Er2O_3. *In press Journal of Nanoelectronics and Optoelectronics, 2020.*

Alqahtani MS, **Almarhaby AM**, Hussein KI, AbouDeif YM, Afifi H, Zahran H, et al. Radiation attenuation and photoluminescence properties of host tellurite glasses doped with Er3+ ions. Journal of Instrumentation. 2021;16(01):P01002-P.

Almarhaby AM, Lees JE, Bugby SL, Alqahtani MS, Jambi LK, McKnight WR and Perkins AC. Characterisation of a near-infrared (NIR) fluorescence imaging systems intended for hybrid gamma-NIR fluorescence image guided surgery. Journal of Instrumentation. 2019;14(07):P07007-P.

Conferences

Awad M. Almarhaby, John E. Lees, Sarah L. Bugby, Mohammed S. Alqahtani, Layal K. Jambi, William R. McKnight and Alan C. Perkins. Evaluation of Near Infrared Fluorescence System for Dual Gamma-NIR Intraoperative Imaging.IEEE NSS-MIC, Manchester, United Kingdom, 2019.

Awad M. Almarhaby, John E. Lees, Sarah L. Bugby, Mohammed S. Alqahtani, Layal K. Jambi, Numan S. Dawood, William R. McKnight, Bahadar S. Bhatia and Alan C. Perkins. Characterisation of a New Imaging System for Gamma-Near-Infrared Fluorescence-Guided Surgery. TOPIM TECH, Chania, Greece, 2019.

Awad M. Almarhaby, John E. Lees, Sarah L. Bugby, Mohammed S. Alqahtani, Layal K. Jambi, Numan S. Dawood, William R. McKnight, Bahadar S. Bhatia and Alan C. Perkins. A multimodality hybrid gamma-near infrared fluorescence (NIR) camera for intraoperative cancer surgery. Photon 2018, Birmingham, United Kingdom, 2018.

Mohammed S. Alqahtani, John E. Lees, Sarah L. Bugby, Layal K. Jambi, Aik H. Ng, Bahadar S. Bhatia, Numan S. Dawood, **Awad M. Almarhaby**, William R. McKnight and Alan C. Perkins. A novel small field of view hybrid gamma camera for scintigraphic imaging. SPIE Medical Imaging 2018: Image-Guided Procedures, Robotic Interventions, and Modeling. California, United States, 2018.

LK Jambi, JE Lees, SL Bugby, MS Alqahtani, BS Bhatia, NS Dawood, **AM Almarhaby**, WR McKnight, AH Ng and AC Perkins. Development of small field of view hybrid gamma camera for intra-operative imaging. The 5th International Conference on Radiation Medicine, Riyadh, Saudi Arabia, 2018.

List of acronyms

APD	Avalanche photodiodes
APSS	Albumin-enriched physiological salt solution
BLI	Bioluminescence imaging
CCD	Charge coupled device
CGC	Compact gamma camera
CLI	Cerenkove luminescence imaging
CMOS	Complementary metal oxide semiconductor
CNR	Contrast-to-noise ratio
CT	Computed tomography
DCR	Dark count rate
DOI	Depth of interaction
EMCCD	Electron multiplication charge coupled device
FDG	Fluorodeoxyglucose
FWHM	Full-width at half maximum
GAPD	Gieger avalanche photodiodes
GASMAS	Gas in scattering media absorption spectroscopy
HGC	Hybrid gamma camera
HGRI	High-resolution gamma imager
ICG	Indocyanine green
IDL	Interactive data language Imaging
LED	Light emission diode
LFOV	Large field of view
LL	Large lesion
MGRC	Mini gamma ray camera
ML	Metastatic lesions
MRI	Magnetic resonance imaging
ND	Natural density
NIRFI	Near infrared fluorescence imaging

OCT	Optical coherence tomography
PBS	Phosphate-buffered saline
PCB	Printed circuit board
PDE	Photon detection efficiency
PET	Positron emission tomography
PHD	Pulse height distribution
PIN	Positive intrinsic negative
PMMA	Polymethyl methacrylate
PMTs	Photomultiplier tubes
PN	Positive negative
QE	Quantum efficiency
RALP	Robot-assisted laparoscopic prostatectomy
RGB	Red, green, blue
ROI	Regions of interest
RTV	Room-temperature vulcanizing
sCMOS	Scientific complementary metal oxide semiconductor
SFOV	Small field of view
SiPM	Silicon photomultiplier
SLN	Sentinel lymph node
SNR	Signal-to-noise ratio
SPECT	Single-photon emission computed tomography
TEC	Thermo-electric cooler
TOF	Time of flight
US	Ultrasound

Chapter 1

Introduction

1.1 Background and motivation

Cancer, as an intricate genetic fatal disease and a leading cause of death, continues to thwart patients, physicians, and researchers despite the significant technological advancements and various scientific breakthroughs in understanding its biological underpinnings. Given this dilemma, the complexity of cancer treatment manifests at every different stage, including reliable early detection, precise distinction, accurate determination of tumour margins during intra-surgical procedures, tracking of tumour metastasis and prediction of recurrence [1, 2].

On average, there was more than 1000 new patients diagnosed with cancer every day between 2015 and 2017 in the United Kingdom [3]. The total number of new cases is predicted to increase by 55% in men and 35% in women by 2030. In breast cancer cases, incomplete tumour removal was reported at rates between 20 and 25% with an alarming recurrence rate of 27% [4]. However, the mortality rate has decreased in the last decade, despite the increased new cases, due to enormous developments in diagnostic and therapeutic procedures [1, 3].

Various clinical procedures have been used to combat cancer such as surgery, chemotherapy, radiotherapy and immunotherapy. Surgery is considered as the principal and most effective approach for a complete cancer removal [5]. This practice predominantly relies on surgeons' visual inspection and palpation to detect and resect tumour while keeping normal tissue untouched. However, this practice may lead to a possible failure in achieving negative margins and then necessitate a repeat surgery [6, 7, 8]. Incomplete resection is commonly associated

with significantly higher cancer recurrence rates and poorer survival. Precise tumour distinction from normal tissue is based on changes in the appearance (colour) and morphology (shape) of tissues. However, at very small tumour size in early stages, contrast could be lower to a cellular or sub-cellular level making tumour identification significantly challenging [9].

There are only six major imagining modalities that are commonly available for cancer identification, namely: X-rays (plain and computed tomography (CT)), ultrasound (US), magnetic resonance imaging (MRI), single-photon emission computed tomography (SPECT), positron emission tomography (PET), and optical imaging. These medical imaging technologies have played a key step towards addressing the challenges across the various types of cancer management [4]. However, it is still a challenging task to translate these modalities to the surgical phase due to, in general, changed body setup, internal organs manipulations, large device sizes, cost, increase operation time and interruption of surgical workflow [4, 10].

Non-imaging gamma probes technologies provided an integral solution to localise tumour site in surgical beds [11, 12]. This technique has a small size, is easy to operate, widely available and routinely used to detect radioactive accumulation. Gamma probes provide information as a sound output, thus, they are unable to determine radioactive distribution precisely [13, 14]. Alternatively, interaoperative SFOV gamma camera can enhance cancer treatment by providing higher degree of accuracy for tumour delineation in comparison to gamma probes [12, 15]. More details about these modalities are given in Chapter 3.

However, current intraoperative gamma imaging experiences inadequate spatial resolution; this prevents clinicians from accurately discriminating between malignancies and adjacent healthy tissues [16]. Another source that may affect the ability of detecting a target by a gamma device is the background radiation from surrounding tissues [16, 17]. Moreover, acquisition time requires several minutes to gain good statistics of photon counts in order to construct a proper image [17, 18, 19]. Radio-tracers are not always available to all hospitals and normally requires special preparation. It is also known that a human's cell normally has an average diameter of 10 μm and a tumour requires about 10^6 cells to proliferate uncontrollably by the so called angiogenic switch process [9]. Accordingly, imaging such a cohort of cells number could be challenging for conventional SFOV gamma camera [20]. This can be overcome utilising an imaging

tool that has better sensitivity and spatial resolution to detect such a tumour with a micro-scaled structure.

The application of optical imaging modalities in medicine have captivated the attention of many clinicians and researchers due to the feasibility of visualising anatomical and molecular structures intra-surgically, compactness and low cost [21, 22, 23]. These modalities include ultraviolet (UV), visible, NIRF and infrared (IR) light. Despite its limitations in terms of tissue penetration depth, optical imaging can offer significant advantages for early cancer detection because of the superior molecular sensitivity and spatial resolution [17, 18, 21]. Optical imaging (visible) has been used for a long time in combination with gamma probe and SFOV gamma camera for various types of cancer surgery [17, 24]. In such a multimodality system, the penetration ability of gamma allows better detection of lesion at high depth while the high spatial resolution of optical imaging facilitates a complete tumour resection.

In this regard, a novel multimodality handheld gamma camera called the HGC has been already designed to simultaneously visualise gamma and visible images for surgical procedures [25]. The HGC has been developed by the BioImaging Unit at the Space Research Centre (SRC) – University of Leicester in collaboration with the University of Nottingham. This camera consists of a columnar CsI:TI attached to an electron multiplication charge coupled device (EMCCD). A knife edge pinhole collimator is used while an optical camera is placed in front of the camera head. The HGC camera is capable of obtaining real-time fused images of gamma and optical (visible light) modalities with small, compact, good resolution and cost effectiveness.

In comparison to the visible-range light imaging techniques, NIRF imaging (wavelength range 700-1000 nm), an area that this thesis concern with, offers deeper tissue penetration capabilities (1-2 cm) and less autofluorescence from adjacent tissues, providing better signal-to-noise background ratio [17, 18, 22]. Different studies have shown that the concurrent use of NIRF-radioactive tracers enhances sentinel lymph node (SLN) detection rate in comparison to the standard techniques using gamma emitters with visible blue dye [16, 17, 18]. For this reason, there was an interest to improve the HGC efficiency of SLN detection by changing the optical imaging system from the visible to the NIRF range. Therefore, the high penetration ability of gamma can be combined with the high spatial resolution of NIRF technique for successful cancer eradication.

Recently, SiPM has emerged as a compelling technology in various devices such as gamma cameras, SPECT, PET, X-ray scanners, calorimetry and radiation monitoring [26, 27, 28]. This is due to the several advantages of SiPM that outweigh those of APD and PMTs such as high internal gain (at the level of 10^6), lower operating voltages, lower power consumption, insensitivity to magnetic fields, robust and small design.

Different studies have investigated SiPM-based scanners in medical use, showing their potential advantages. For example, a study was conducted by Queiroz et al. to optimise radiation dose of patients [29]. This was done by comparing PMTs-based fluorodeoxyglucose (FDG)-time of flight (TOF)-PET/CT to SiPM-based TOF-PET/MRI. Their findings assumed that SiPM-based PET provided images with good to excellent quality, even when reducing the dose of injected FDG by more than 50%. Another study by Zeimpekis et al. evaluated SiPM-based technology TOF-PET/MRI compared to conventional TOF-PET/CT as a function of acquisition time [30]. This clinical evaluation showed an improved image quality and sharpness with lower noise levels when using SiPM-based PET/MRI instead of PET/CT images. Several other studies have shown that the use of SiPM demonstrated decreased radiation dose, reduced acquisition time and good image quality for PET scanner [31, 32, 33].

For SPECT modality, Carminati et al. characterised a prototype SiPM-based MRI-compatible SPECT for human brain imaging using CsI:TI scintillator and arrays of SiPM [34]. Trigilio et al. experimentally evaluated a SiPM-based scintillation detector for MRI-SPECT systems for clinical imaging [35]. A study by Brown investigated several monolithic scintillator crystals coupled to SiPM for SPECT applications [36].

In the intraoperative imaging context, Popovic et al. developed a round hand-held gamma camera using cerium-doped lanthanum bromide ($LaBr_3$:Ce) plate coupled to SiPM array [37]. Goertzen et al. constructed a miniature gamma camera for SLN biopsy utilising CsI:TI crystal and SiPM [38]. Further study by Bizzozero et al. evaluated pixelated scintillation arrays of GAGG:Ce, LYSO and CsI:TI attached to SiPM [39]. Based on their findings, a compact gamma camera was designed combining GAGG:Ce to SiPM due to the better achieved energy resolution of GAGG compared to LYSO and CsI:TI crystals. These studies provided an insight into the useful advantages of new SiPM-based imaging systems, such as reduced scanning time, radiation dose reduction and enhanced

image quality. Thus, earlier tumour detection with more accurate surgical delineation could be achieved with such systems, leading ultimately to better cancer patient care and improved clinical management.

1.2 Aim of thesis

The primary aim of this thesis is to provide solutions to enhance surgical cancer detection through exploiting gamma and NIRFI techniques. This work evaluates different NIRFI cameras using various bespoke phantoms, fluorescent dyes and different experimental configurations. The eventual aim of this assessment is to combine the NIRFI technique with the HGC imaging system. In addition, this thesis seeks to demonstrate the usefulness of SiPM technology for nuclear medicine imaging, in particular for intraoperative imaging. To achieve this, SiPM performance was evaluated with temperature and overvoltage variations. Following this, SiPM technology was combined to scintillator layers, a columnar CsI:TI and a monolithic GAGG, to investigate its use for intraoperative gamma imaging. The ultimate aim is to design an intraoperative gamma-NIRF imaging system with high cancer detection capability.

1.3 Outline of thesis

The research work presented in this thesis is described over 7 Chapters. The first Chapter presents a general introduction to the main concepts that underpin intra-surgical imaging and describing the motivation of this thesis. The second Chapter explains briefly the principle of $\gamma-$rays measurement describing the physics of scintillators and photodetectors. In the third Chapter, the existing imaging modalities were summarised and compared with a particular focus on different gamma and optical imaging methods for intraoperative applications. Chapter 4 describes the method that was developed to evaluate NIRF imaging cameras to be combined with the HGC for dual gamma-NIRF imaging concept. Chapter 5 focuses on SiPM to study different parameters under different experimental conditions. In Chapter 6, scintillators SiPM-based detectors were tested including thin layers of CsI:TI and GAGG:Ce to investigate their feasibility for intraopertive imaging. Chapter 7 presents the overall conclusions, and draws a map of possible future work that can be conducted utilising this knowledge to guide the design of instrumentation.

1.4 Personal contribution to this research

The HGC imaging system was developed by the research group before commencing my PhD studies. The research group has evaluated the HGC capability for clinical application using various theoretical, experimental and clinical configurations with different designs. The initial notion of radio-NIRF combined system was suggested and tested before joining the BioImaging unit. I fully designed the characterisation experimental method, constructed the medical phantoms, collected data and analysed the results described in Chapter 4. The evaluation setup in Chapter 5 was designed by Mr Angaraj Duara in order to characterise the electrical properties of the SiPM. The python script for converting the trace file to text format was developed by Dr Steve Leach. I carried out data collection and analysis procedures. In Chapter 6, I fully planned and conducted the experiment, and analysed the produced data.

Chapter 2

Principles of radiation measurements

2.1 Introduction

Detection of ionising radiation plays a vital role in many branches of science and technology [40]. Detectors could be simply used to detect the presence of ionising radiation, but they often are designed to further give precise information about the type and energy of the detected radiation. The following sections will briefly describe various detectors based on scintillation principles in conjunction with the most common photosensor, the photomultiplier tubes (PMTs). Other devices that are made of silicon materials, including the charge coupled device (CCD), complementary metal oxide semiconductor (CMOS), PN, PIN, avalanche photodiodes (APD) and silicon photomultiplier (SiPM), will also be briefly discussed.

2.2 Scintillation detectors

The detection of ionising radiation by scintillators is based on the conversion of the kinetic energy of ionising radiation to visible light. Scintillating materials can be solids, liquids or gases. Therefore, when a γ-ray enters a scintillation detector, all or part of the photon energy will be transferred to an electron by an ionisation or excitation process [40, 41]. In the excitation process, electrons are raised to excited states which subsequently decay by emitting photons in the

visible light range. This prompt emission of visible light from a substance by means of excitation is called fluorescence. This visible light can be detected by sensitive photodetectors to convert it to a signal that will be suitable for data analysis. Scintillating materials can, in the main, be categorised in two ways: as either organic or inorganic materials.

2.2.1 Organic scintillators

Organic-based liquids and plastics scintillators are typically faster in their response times but have lower light yields compared to inorganics [42]. The fluorescence process in organic scintillators originates from raising electrons to higher electronic states and, in addition, exciting the vibrational states in the molecule of interest. The energy required to excite the molecular vibrational states is in the region of 0.1 eV, while it is greater than 1 eV to excite an electron [41]. Organic scintillators have different applications and are often used for detecting β, α and neutrons particles [42]. This type offers the most economical means when large area (> 1 m^2) is required in applications such as high energy radiation detection and cosmic ray physics. Examples of common organic scintillators are anthracene, stilbene and naphthalene [40].

Figure 2.1 illustrates the various energy levels resulting from the absorption of incoming photons and subsequent emission of light for organic scintillators [40]. It shows a number of singlet states (electronic spin 0) that are labelled S_0, S_1, S_2 and S_3 with increasing energy alongside triplet electronic levels (spin 1) that are, in the same manner, denoted by T_1, T_2 and T_3. Each electronic configuration is further subdivided into a number of vibrational energy levels with smaller spacings. Electrons excited by incoming photons undergo electronic transitions to different higher states. Prompt fluorescence results when an electron de-excites and is transferred from, for instance, the singlet state S_1 to the ground state, S_0. Another decay phenomenon which takes place with different transition process is that of intersystem crossing. In this case, excited singlet states may de-excite to a triplet states but with a longer lifetime. Whilst intersystem crossing itself is radiationless, the light subsequently emitted from the triplet state is known as phosphorescence.

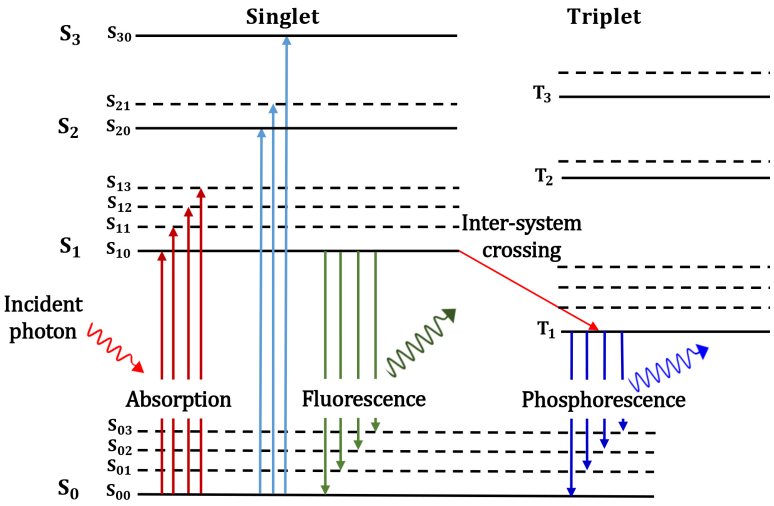

Figure 2.1: Excitation of an organic molecule by an incoming photon showing electronic excitation states. Absorption of photons excites electrons from S_0 to S_1 and higher singlets. Fluorescent light is emitted when electron transitions occur between S_1 and any vibrational level in the ground state. Phosphorescence may appear at longer time delays when conversion via intersystem crossing occurs between singlet and triplet states [40].

2.2.2 Inorganic scintillators

In comparison to organic materials, inorganic scintillators have a higher density that provides a higher stopping power for γ-rays, better energy resolution, higher light output, shorter decay times, and excellent linearity with incident photons [43, 44]. These characteristics have seen the introduction of inorganic scintillators as the most commonly used type in γ-ray detection and nuclear medicine applications. However, the main drawbacks of inorganic crystals are the difficulties in obtaining specific shapes and some types are hygroscopic [44].

Unlike organic scintillators, the scintillation mechanism in inorganic crystal occurs in the electronic band structure [41]. In pure inorganic scintillators (alkali halides), incident radiation elevates electrons from the valence band to the conduction band. Then, excited electrons returns instantly to the valance band, emitting fluorescence photons. However, photons emitted in pure crystals such as NaI are not in the visible light range, and may be absorbed by the crystal itself or by the glass window of the photodetector [40, 45]. For this reason, heavy metal activators are used to alter the wavelength of produced light. Therefore,

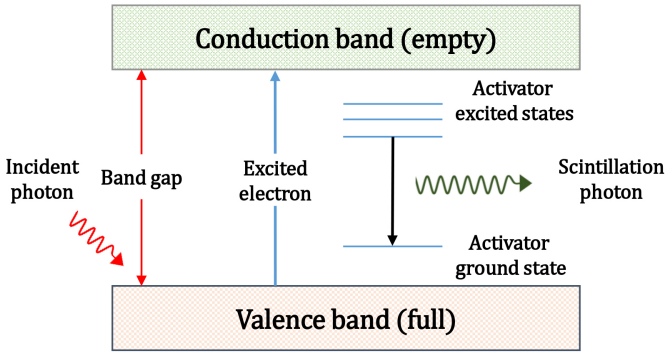

Figure 2.2: Scintillation process in inorganic crystal showing the electronic band structure with the presence of the activator. Incident radiation excites electrons, some of which migrate to the activator sites leaving behind vacancies in the valance band. De-excitation of electrons to the valance band causes fluorescence emission [41].

doping with thallium shifts the wavelength from 333 nm in pure NaI to 410 nm for NaI [TI], which improves the detection response for traditional photodetectors [41]. Figure 2.2 shows a schematic diagram of the fluorescence process in an inorganic scintillator.

There are different scintillators that were developed during 1950s which are well known today, such as NaI (Tl), CsI (TI) and Eu-doped Ca F_2 [44]. Currently, the majority of scintigraphy cameras in medical applications, such as SPECT scanners, use NaI [Tl] and CsI [Tl] crystals as their performance is perfectly adequate for the needs of SPECT imaging [45, 46]. After the 1980s, different man-made materials were developed such as $Bi_4Ge_3O_{12}$ (BGO). In comparison with NaI, CsI and CaF_2, BGO has very high effective atomic number, providing high photoelectric conversion efficiency. Therefore, BGO was the scintillator candidate in the early types of PET devices. Further development was achieved through the approach of Cerium-doping in insulating host materials, such as Ce-doped Lu_2SiO (LSO) and its Y admixture (LYSO) [44]. These new scintillators have shown better sensitivity and spatial resolution with faster decay times than BGO. For this reason, the newest generation of PET scanners are equipped with Ce-doped LYSO instead of BGO [46].

During the last two decades, an enormous amount of research has been conducted to develop scintillators with even greater efficiencies and faster detection capabilities. Ce-doped Gd_2O_2S exhibits very high scintillation intensity and has been utilised in CT scanners with a decay time of only several microseconds

[47, 48]. Moreover, GOS has a scintillation emission that is well-matched with the spectral sensitivity of Si-based photodetectors. Another example is Ce-doped $Gd_3(Al,Ga)O_{12}$ (GAGG), which is a newly developed crystal that has good stopping power and ruggedness [49]. It has an emission peak at 520 nm which is suited to silicon photomultiplier (SiPM) readout. More details of SiPM will be given in section 2.3.6. GAGG crystal is useful in various applications in medical imaging, such as CT, PET, and SPECT scanners [46]. Considerable attention has recently also been given to Eu_3-doped $(Lu,Gd)_2O_3$ for medical applications [47]. This new crystal has a higher emission intensity in the red wavelengths which also makes it suitable for coupling with silicon-based photodetector.

Table 2.1 reports examples of various inorganic scintillators used in medical imaging. One of the main important characteristics of a scintillator material is the stopping power at a given energy range; therefore, material with high density is favoured. Another important requirement is the high output which is usually needed to be > 20,000 photons/MeV in order to reduce the noise in the image at low signal levels and improve the energy resolution. CsI [Tl], GAGG and $LaBr_3$ have the highest light yield compared to other scintillators in the table. Another important property is the scintillation emission that is required to match the spectral sensitivity of silicon photodetectors. Decay time has also to be short to reduce the dead time and hence increasing the counting rate capability [40].

Scintillator & reference	**Density**	**Bandgap**	**Light yield**	**Emission light**	**Decay time**
	(g/cm^3)	(eV)	(ph/MeV)	(nm)	(μs)
NaI [TI][46]	3.67	5.9	38,000	415	0.23
CsI [Tl][46]	4.51	6.4	54,000	550	1
BGO[46]	7.13	5	9000	480	0.3
LuAP [Ce][46]	8.34	NA	10,000	365	0.017
LSO [Ce][46]	7.4	6	27,000	420	0.04
$LaBr_3$[Ce][46]	5.29	5.6	61,000	358	0.035
GOS [Ce][48]	7.34	4.3	35000	512	600
GAGG [Ce][49]	6.63	6	60,000	520	0.09-0.17

Table 2.1: The main characteristics of most common scintillators developed for medical applications.

2.3 Photodetectors

2.3.1 Photomultiplier tubes

The photomultiplier tubes (PMTs) are considered as the oldest photosensor still in use for converting emitted visible light (scintillation photons) into an electrical signal that is proportional to the incident radiation energy [40, 41]. A standard PMTs consists of a photocathode, a dynode chain and an anode, as shown in Figure 2.3. The photocathode is made of a metallic material that has a low work function (such as potassium) to enhance electrons release by incident photons via the photoelectric effect. Released electrons normally have low kinetic energies in the range of about 1 eV [41]. These electrons are then guided under high electric fields to be accelerated towards the dynode chain where impact ionisation occurs to produce higher gain through electron multiplication. An electron gain of up to 10^6 can be achieved using the PMTs operating principle.

The high gain associated with low noise remains the principal advantage to PMTs, making them appropriate for reading out large areas of scintillators [40, 41]. However, PMTs have some practical limitations such as heavy weight, large size, high operating voltage (normally from 0.5 to 3 keV), fragility and sensitivity to magnetic fields. These problems can complicate the use of PMTs in portable devices or in small instruments where space is more important [40, 50].

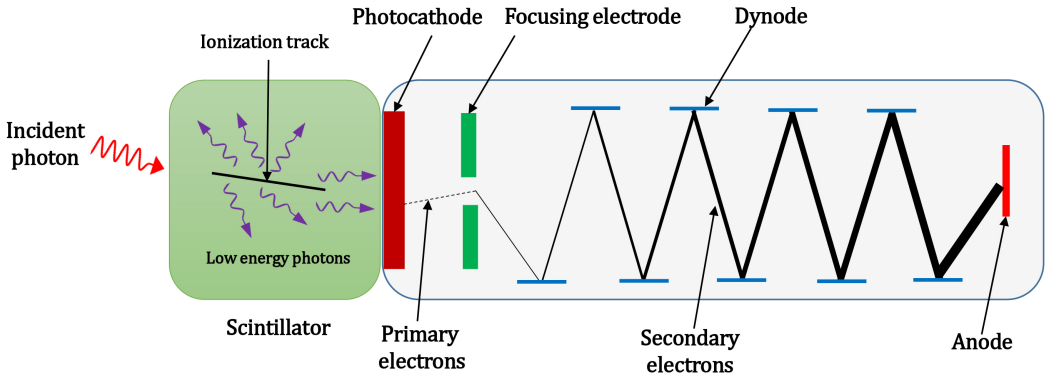

Figure 2.3: Schematic diagram representing PMT components that are normally placed within a glass enclosure [41]. Primary electrons are accelerated in vacuum to produced secondary electrons with a gain of up to 10^6.

2.3.2 Charge-coupled devices

Silicon-based charge coupled devices (CCDs) were first introduced in 1970 as a microcircuit device for visible light imaging. Since then, CCDs have become widely used sensor for ionising radiation detection. Figure 2.4 shows a schematic diagram of a simple CCDs architecture that typically has a square shape with an area of 1-2 cm^2 [40, 51, 52]. When a voltage is applied to the control electrodes, each pixel will produce an individual potential well. Therefore, any electron generated by the incident ionising radiation will be stored at each corresponding pixel. Following the exposure period, a time variable voltage sequence is applied using a pulse drive in a specific pattern to shift the charge packets to the required direction. Subsequently, accumulated charges will be sequentially transferred to the adjacent column or row to reach the readout part.

However, thermally generated electrons within the silicon, corresponding to leakage current electrons, will also accumulate in all pixels, representing a source of noise [40, 52]. In this case, it is necessary to cool the CCDs system in order to reduce the leakage current. Another limitation of CCDs is that it cannot register the specific arrival time of the signal as each follows a sequential transfer of signals of rows of pixels towards the readout section.

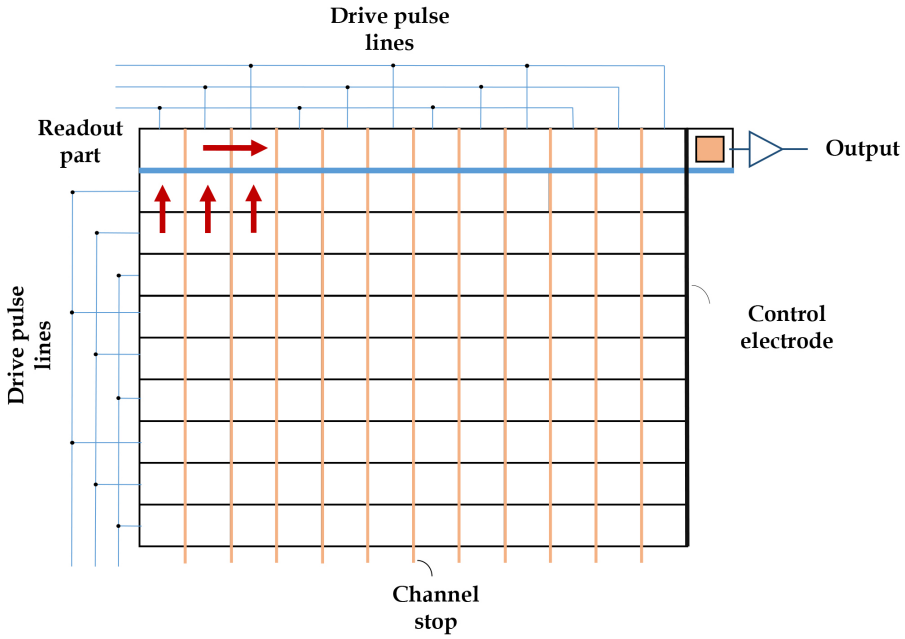

Figure 2.4: Layout of the CCDs surface showing a number of pixels fabricated on a control electrode and divided by channel stops. Arrows represent the direction of charge collection towards the readout section [40].

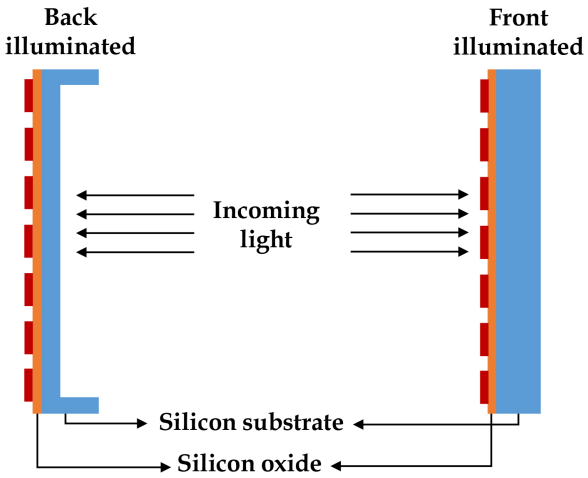

Figure 2.5: A simplified structure for back- and front-illuminated CCDs types. In the front-illuminated design, light passes through the frontside gate structure to reach the sensitive area. The back-illuminated structure allows light to reach the sensitive area directly [52].

Thus, the CCDs exhibit a relatively slow readout process compared to detectors that drive charges continuously to their respective readout sections. Smearing effects from any additional hits during charge movement may also result in an incorrect positional registration, which could represent a potential problem [53].

The CCDs are usually classified as either front- or back-illuminated designs. These two terms indicate whether light is incident on the frontside or the backside of the detector, as shown in Figure 2.5. The CCDs that employ frontside illumination are sensitive to light with wavelengths in the 400-1100 nm range with quantum efficiencies (QE) of up to 80% in the 450-800 nm range [54]. However, they are not suitable for wavelengths under 350 nm as the QE values measured below 400 nm are typically less than 5%. This is attributed to the atomic structure of silicon and to the light absorption by the frontside gate structure [54]. Therefore, the back-illuminated design has been developed where light can pass directly through a thinned substrate (thickness less than 20 μm) onto the sensitive area. As a consequence lower absorption is achieved, leading to better sensitivity for shorter wavelengths.

Another approach in manufacturing has allowed CCDs to be utilised for low-light imaging applications. This approach is based on increasing the charge level collected above the readout noise using electron multiplying (EMCCDs) technology [55]. Electron multiplication takes place before the charge reaches the

readout amplifier in the multiplication register, where electrons are accelerated from pixel to pixel by applying a high voltage (up to 50 V) [55]. Accelerated electrons generate secondary electrons by an impact ionisation process. This enables EMCCDs to increase the gain by a factor of 10^3 compared to normal CCDs, resulting in better signal-to-noise ratio (SNR) for low-level signal applications [52, 55].

2.3.3 Complementary metal oxide semiconductor

Complementary metal oxide semiconductor (CMOS) detectors have received considerable attention over the last few decades. This technology has shown a promising performance compared to CCDs technologies. Figure 2.6 demonstrates the overall architecture of a CMOS imager which contains, in general, a pixel array, analogue signal processor, raw and column selector, and timing and control units [40, 56]. The dominant type of pixel circuit is the active pixel sensor (APS) where an amplifier is incorporated into each pixel, improving its performance.

Each pixel has its own charge to voltage converter and voltage amplifier circuits, providing a higher-speed imaging process [56, 57]. Moreover, power consumption is generally lower than that of CCDs as each amplifier is only activated during the readout process. The synchronous shutter design in CMOS enables sharper image and reduces the typically observed smearing effect in the CCDs array [40].

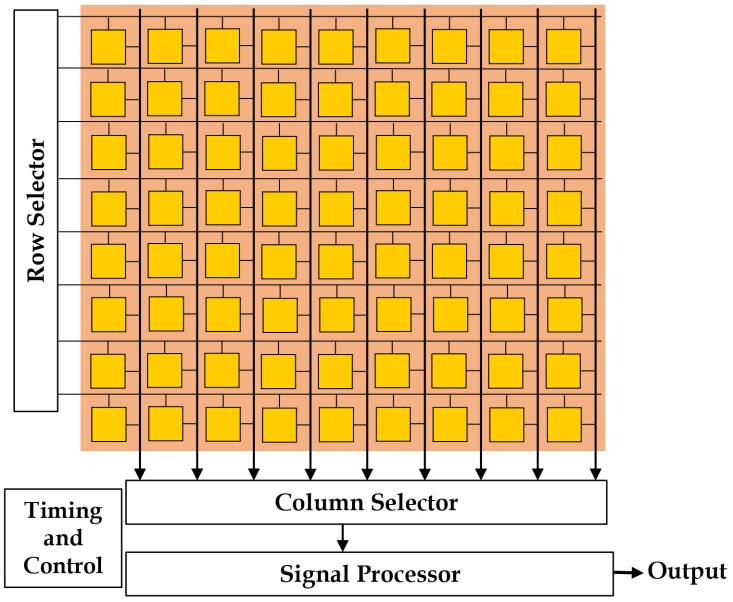

Figure 2.6: CMOS sensor architecture, illustrating its main components [40].

CMOS	CCD
Lower power consumption	Lower noise
Lower cost	Lower dark current
Single power supply	Higher sensitivity
High integration capability	Smaller pixel sizes
Single master clock	100% Fill factor
Random access	Electronic shutter without artefacts

Table 2.2: The main advantages of CMOS and CCDs sensors [56].

Table 2.2 provides some of the main advantages of both CCDs and CMOS light detectors. However, CMOS detectors APS-based technique, has a lower sensitivity due to the limited fill factor, resulting in lower quantum efficiency (QE) compared to CCDs [58, 59]. Another fundamental drawback of CMOS is the high noise levels that affect the signal, in particular for detecting low-levels of photons [40]. This stems from different sources such as shot noise, thermal noise after each pixel readout, amplifier and other electronic noise.

Recently, more advanced fabrications with highly integrated processing circuits have been used to enhance both CMOS and CCDs performance [57, 58, 59]. The main focus has been on the desired features of the overall imaging system including low noise, low power dissipation, high dynamic range, high-speed imaging, high sensitivity and low voltage operation. Nevertheless, it is a difficult task to achieve all of these properties in one system; rather, one feature will have a greater priority than another as dictated by the specific application.

2.3.4 PN and PIN photodiodes

Although photomultiplier tubes (PMTs) are the most commonly used type of photodetector in medical gamma detection, advances in the development of silicon-based semiconductor photodiodes have started to allow for the replacement of PMTs [60]. This is due to the various advantages of photodiodes compared to PMTs including, in general, better energy resolution, reduction in power consumption, smaller size, lower price, lower noise, longer lifetimes, improved ruggedness and insensitivity to magnetic fields [40, 60].

Silicon positive-negative (PN) photodiodes are formed by attaching a p-type semiconductor (the majority of charge carriers are holes) to n-type semiconductor (the majority of charge carriers are electrons) [61]. Once p-type (anode)

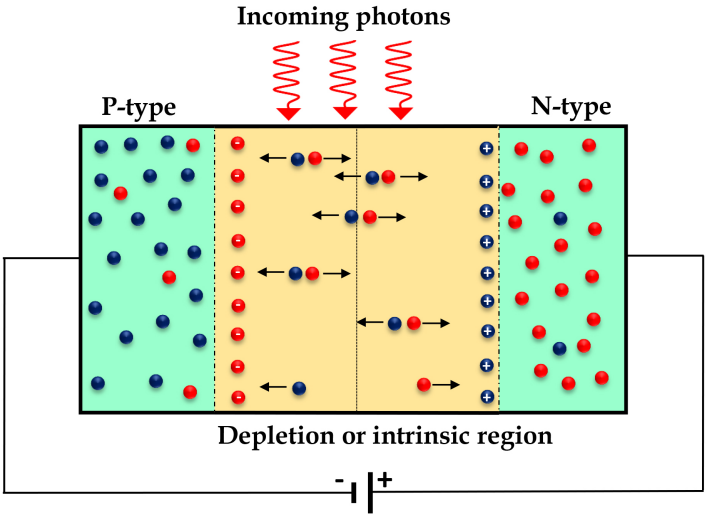

Figure 2.7: A PIN photodiode with an intrinsic region in the middle. When gamma photons passes through the depletion regions electron-hole pairs are created. Electrons (red) diffuse to n-type region and holes (blue) diffuse to the p-type region creating a signal [61].

and n-type (cathode) regions are connected, a depletion region is created at the junction that is sensitive to radiation. When radiation passes through the depletion layer, electron-hole pairs are created under the influence of the electric field and forms a current pulse represents incident radiation.

Jun-ichi Nishizawa invented the PIN diode in 1950 [62]. This device improves the frequency response and bandwidth of PN photodiodes. This can be achieved by inserting a region of intrinsic silicon in between the p- and n-regions, as can be seen in Figure 2.7 [61]. The main role of the intrinsic region is to decrease the capacitance of the photodiode per unit of area to speed up the movement of charge carriers between the two regions. Therefore, PIN can be used for applications where faster operation is desirable making it suitable for high-frequency pulsed applications. These photodiodes operate at a gain of 1, i.e., no signal amplification is used, and are thus not used for detecting lower light signal levels [60, 61].

2.3.5 Avalanche photodiodes

In PIN photodiodes, the amount of signal produced is relatively small. This signal can be increased above the level of the electronic noise by applying higher bias voltage [60, 63]. Photodiodes operating using this technique are called avalanche photodiodes (APDs). Similar to the PIN junction, the incident photon

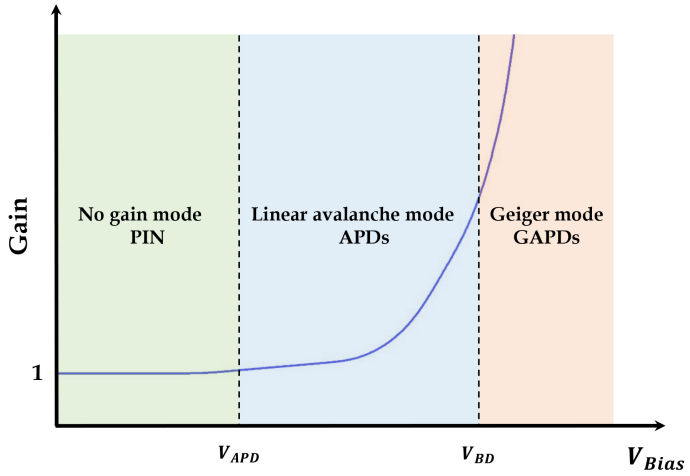

Figure 2.8: Gain-voltage characteristics of silicon photodiode. Ordinary photodiode operate at gain equals 1. By increasing the bias voltage, the gain can reach a magnitude of a few hundreds in the linear avalanche region. With further increase in the bias voltage, photodiode enters the Geiger region [64].

generates an electron-hole pair which is then separated by the electric field. In APDs, the higher applied voltages cause the charge carriers to accelerate and thus gain sufficient kinetic energy to create further electron-hole pairs through impact ionisation. This internal signal amplification property of APDs allows higher signal-to-noise-ratio (SNR) and improved sensitivity compared to PIN type [63, 64]. APDs are normally operated at a reverse bias voltage close to, but below, the breakdown voltage (V_{BD}). V_{BD} is the point where Geiger discharge starts; more details about V_{BD} will be given in section 2.3.6.1. Figure 2.8 illustrates the three distinct regions based on gain-voltage curves showing modes of operation for photodiodes.

Despite the overall performance improvement introduced by the APDs technique, high performance is limited to detectors with sensitive areas of about 1 cm^2 [65, 66]. The avalanche process also has an effect on thermally excited electrons in that it increases dark current signal. Its gain is still limited to a factor of 10^2-10^3, compared to 10^5-10^7 for PMTs with a poorer timing resolution [66]. Moreover, APDs need to be connected to a well-regulated high voltage supply (up to 350 V) as the gain factor is quite sensitive to the applied voltage and thermal variations. These challenges have limited the overall performance characteristics of APDs to replacing PMTs-based design systems in medical applications such as in PET scanners [66].

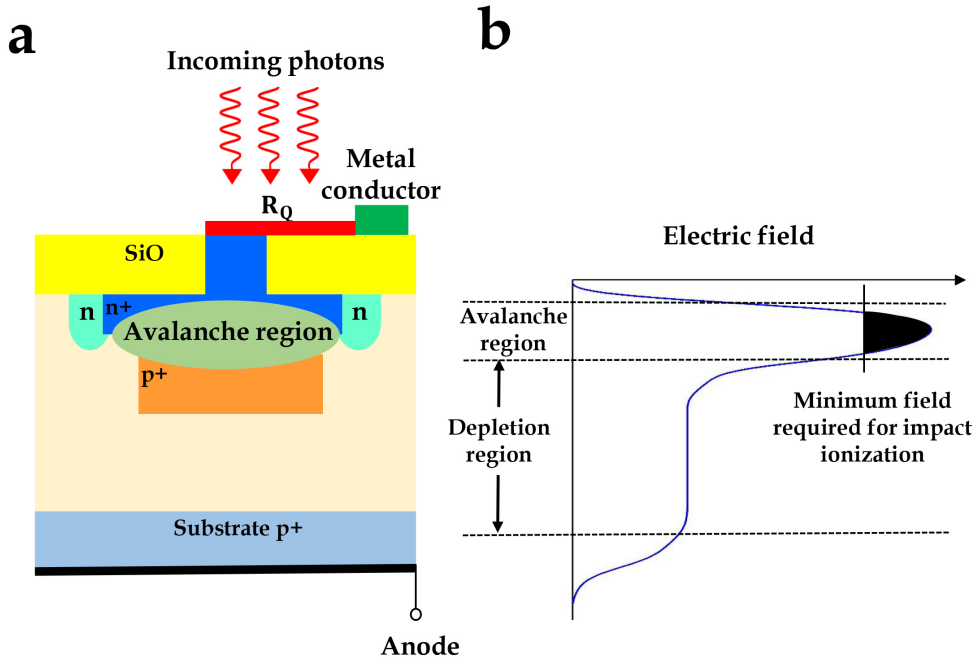

Figure 2.9: A cross-section of GAPDs design in (a). The avalanche region is shown in light green. The electric field distribution is depicted in (b), reaching the maximum value at the n+ and p+ junction [67].

With further increase of the bias voltage above the breakdown voltage, as denoted previously in Figure 2.8, the photodiode enters Geiger mode (GAPDs), where a substantial higher electric field (5×10^5 V/cm) is generated that enhances intensity of each avalanche [67]. At large values of the electric field, an exponentially growing number of avalanches can be created, hence the gain does not follow a linear relationship with changes in reverse voltage. Therefore, all pulses generated from GAPDs are of the same amplitude, regardless of the number of photon-induced events. This large output pulse allows GAPDs to be used for detecting even single optical photons, and is also called the single photon avalanche diode (SPADs) [66, 67]. Figure 2.9 illustrates the typical structure of GAPDs and the accompanying electrical field as a function of depth.

In GAPDs mode, the impact ionisation is faster than the signal extraction causing avalanche to be a self-sustaining process. Thus, a current will continually flow through the GAPDs unless quenched [63, 67]. This freely flowing current prevents the production of discrete output pulses of the new photons arriving at the detector. This problem can be solved by connecting a metal quenching resistor (R_q) to allow further signal output from incident photons. As the

avalanche is triggered there will be an increase in the current that results in a voltage drop across the resistor, where the resistance is typically in the range of 1 MΩ [67]. Impact ionisation decreases when the reverse bias falls below the breakdown voltage, resulting in an avalanche drop and consequently a current drop. This returns GAPDs to the initial state in a cyclic process with typical rise and recovery times of 1 ns and 100 ns, respectively [63, 67]. The entire cycle will then be repeated, producing a continuous output of multiple pulses as illustrated in Figure 2.10.

However, the main disadvantage of a single GAPDs is the independence of the output pulse amplitudes on the number of photons that are interacting within the detector [65, 66]. This has limited the utilisation of GAPDs to applications where there is a need to discriminate between incident photon energies. To overcome the lack of proportionality, a two dimensional (2D) array consists of a large number of GAPDs components can be used to image very low light levels. This new form of photodetector is referred to as the silicon photomultiplier (SiPM).

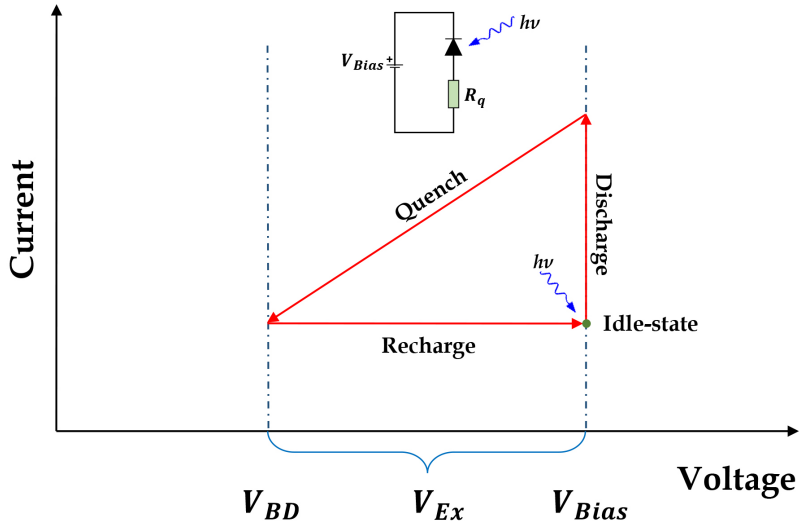

Figure 2.10: Illustration of the steps in the passive quenching process and their dependence on the applied voltage. Once the photon has been absorbed, the GAPDs discharges, resulting in a high current followed by the quenching that causes a drop in voltage and current. After the quenching process, the cell recharges and returns to its idle-state. The equivalent circuit diagram for a reverse biased GAPDs is depicted in the upper insert [67].

2.3.6 Silicon photomultiplier

SiPM is a novel photon counting semiconductor detector that consists of an array of microscopic APDs operating in Geiger mode to provide a higher gain, usually referred to as microcells [68, 69]. A typical individual microcell is made of a p-n junction that has dimensions in the range of 10 to 100 μm. A depletion layer with a thickness of about 0.8 μm is created between the p+ and n+ layers. Due to the micro-thickness of the depletion layer, only tens of volts are required to achieve a high electric field [67]. Then, cells are combined on a silicon substrate while the output signal is collected through the metal conductor. As a result, the advantages of SiPM and GAPDs can thus be combined in a single system, namely those of signal proportionality to number of incident light quanta and the ability to detect single photons. Figure 2.11 shows the equivalent circuit for the SiPM detector and the typical SiPM design.

It is necessary to understand the typical characteristics and behaviour of SiPM and how these relate to the operating principles. These parameters include the breakdown voltage, overvoltage, gain, photon detection efficiency, dynamic range, linearity, optical crosstalk, afterpulses and dark current rate. All of these terms will be explained briefly in the following sections.

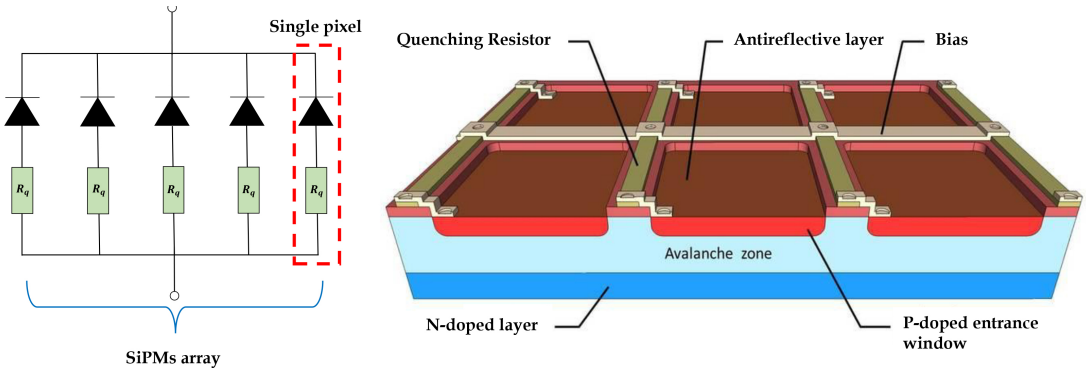

Figure 2.11: The equivalent circuit for SiPM shows that a single pixel consists of an APDs operating in Geiger mode and is connected to a quenching resistor. A diagram of an array of typical SiPM design is shown with the main components [67, 70].

2.3.6.1 Breakdown voltage and overvoltage

The breakdown voltage (V_{BR}) is defined as the point at which SiPM creates a Geiger discharge. It is important to determine SiPM operating point using

the gain-bias voltage plot to derive V_{BR} [67]. Mathematically, the breakdown condition within the depletion region can be derived from the basic integral of the ionisation rate. When the avalanche process is triggered by holes, the breakdown condition is given by the ionisation integral [60]:

$$\int_0^{W_D} \alpha_p exp\left[-\int_0^x (\alpha_p - \alpha_n)\, dx^{'}\right] dx = 1 \tag{2.1}$$

where W_D is the depth of the depletion region in which electron-hole pairs are created by the impact ionisation process, α_n and α_p are the electron and hole ionisation rates, respectively. In the case of initiating the avalanche process via electrons rather than holes, the ionisation integral is expressed by [60]:

$$\int_0^{W_D} \alpha_n exp\left[-\int_x^{W_{Dm}} (\alpha_n - \alpha_p)\, dx^{'}\right] dx = 1 \tag{2.2}$$

The breakdown conditions enable ionisation rates to be determined with electric field dependence, the breakdown voltage, the width of the depletion region and the maximum applied electric field. In the depletion region, the electric field and the potential can be calculated from the Poisson equation. The boundaries of the depletion region in equations 2.1 or 2.2 can be determined numerically via iterative methods and therefore the breakdown voltage can be obtained using [60]:

$$V_{BD} = \frac{\varepsilon_s \xi_m^2}{2qN} \tag{2.3}$$

where ε_s is the dielectric constant of the semiconductor, ξ_m is the maximum electric field across the junction, q is the charge and N is the impurity concentration of the lightly doped side.

Typically, a SiPM is required to operate at few volts above the breakdown voltage, referred to as the overvoltage (ΔV). The overvoltage is defined as the difference between the applied reverse bias voltage and the breakdown voltage, as in the following equation [60]:

$$\Delta V = V_{bias} - V_{BD} \tag{2.4}$$

Overvoltage is associated with current growth when an electron-hole pair initiates an avalanche. The electron-hole population, with the accompanying photocurrent, increases exponentially with time and, hence, the greater the overvoltage, the faster the growth [69, 71]. However, current only increases to a value that is limited by the circuit's resistance. Overvoltages are usually between 1 and 5 V and are commonly recommended by the manufacturer.

2.3.6.2 Gain

The gain of SiPM detector can be described as the amount of charge created by each photon detected. Gain is dependent on overvoltage and can consequently be changed by varying the bias voltage which relates to the breakdown voltage. The breakdown voltage also changes according to temperature, which can result in a gain variation of 0.5% per 1 K for a given bias voltage [69]. Microcell size also has an effect on the gain as each microcell produces a highly uniform amount of charge each time an avalanche is created [69, 71]. Therefore, the gain of a microcell is described by the ratio of the charges generated from each activated microcell to the charge of an electron. The gain can be calculated using equation 2.5 [69]:

$$G = \frac{C.\Delta V}{q} \tag{2.5}$$

where C is the microcell capacitance, ΔV is the overvoltage and q represents the electron charge. Typically, the gain of SiPM is in the order of 10^6.

2.3.6.3 Photon detection efficiency

Photon detection efficiency (PDE) is a measure of the probability of an incident photon to trigger an avalanche on SiPM. There are different factors that are taken into account to calculate PDE such as avalanche initiation probability (P_{av}), fill factor (FF), the applied overvoltage and the incident photon wavelength [60, 71].

The probability that charge carriers will trigger avalanche depends on the applied bias voltage; the higher the bias voltage the higher the average energy of

the charge carriers and consequently the higher the chance to cause impact ionisation. The fill factor has a significant role in PDE measurements as the active sensitive area occupies only a fraction of the surface of the SiPM and photoelectrons will be lost in the dead areas between cells [68]. Improvement of the fill factor can be attained by tightly packing microcells using shorter resistors, or by producing microcells with larger sizes. Nonetheless, a trade-off exists as increasing the microcell size leads to a lower microcell number, and hence lower dynamic range, and increases non-linearity with the number of detected photons [68].

Another factor influencing PDE is the incident photon wavelength as photons with short wavelengths do not penetrate deeply into SiPM and consequently there is a lower chance to create an electron-hole pair within the depletion region [71, 72, 73]. When wavelength increases in the range between 400 to 600 nm, photons penetrate more deeply creating a greater fraction of electron-hole pairs in the depletion region. Therefore, generated electrons need to pass through the high electric field region which increases the impact ionisation probability leading to a higher PDE [72].

By combining the terms mentioned above, given the avalanche probability P_{av}, the quantum efficiency QE and the fill factor FF, the PDE can be expressed as [61]:

$$PDE = P_{Av} \times QE \times FF \tag{2.6}$$

2.3.6.4 Dynamic range and linearity

For a given SiPM, their associated dynamic range can be described as the ratio between the highest and the lowest input signals [66, 67]. The dynamic range depends on the total number of microcells, the pixel recovery time, the applied overvoltage and the incident photon wavelength [67, 68]. Therefore, a larger number of microcells with a small pixel size result in a larger dynamic range and shorter recovery time than sensors with larger pixel sizes.

The linearity of SiPM is represented by the proportionality between the sensor response and the number of incident photons. Theoretically, the ideal pho-

todetector has a linear response within the constraints of SNR >1 and up to saturation [69].

2.3.6.5 Dark count rate

One of the main sources of noise in SiPM is the dark count rate (DCR) that results from thermal electrons within the active volume [69]. DCR depends primarily on the active area, overvoltage and temperature.

Charge carriers generated by thermal agitation are the major contributors to the DCR [68, 71, 72]. But at lower temperatures, tunnelling effects become the main source of DCR noise. This stems from the fact that electrons may tunnel through the band gap and move from the valence to the conduction band [73]. This effect increases as the applied electric field increases. Therefore, the DCR in both cases represents an unwanted source of noise that is essentially indistinguishable from any impinging photons. This noise source is a limiting factor for detecting low-intensity photons and the timing properties of the detector.

2.3.6.6 Optical crosstalk probability

During the avalanche process, it is possible for a secondary photon to emit and travel to a neighbouring SiPM pixel and trigger an undesirable new avalanche in a process which is referred to as optical crosstalk [74, 75]. Penetration into

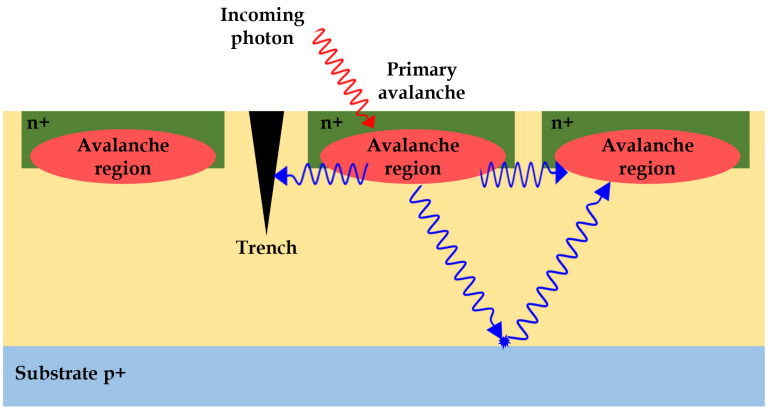

Figure 2.12: Following the primary avalanche caused by the incoming photon, the two possible ways in which a secondary photon can trigger further avalanches are shown [75]. The photon can propagate directly to the neighbouring pixel or be reflected from the substrate and enter an adjacent pixel. An opaque trench is used to minimise the effects direct propagation.

a neighbouring pixel can occur either directly or by reflection from the cell border, as depicted in Figure 2.12. To prevent the effect of this phenomenon, trenches can be created between pixels and filled with light-absorbing material to stop direct photon propagation into adjacent pixels.

In general, there are two types of crosstalk: prompt and delayed [68, 74, 75]. In prompt crosstalk, the photon produced creates an electron-hole pair in the depletion region of a neighbouring pixel, leading to a new avalanche and a simultaneous crosstalk output pulse appearing with the original pulse. By contrast, delayed crosstalk occurs when the photon produces an electron-hole pair outside the depletion region. It is probable for this electron-hole pair to reach the depletion region by diffusion, resulting in further avalanche processes. Therefore, a delay exists between the original pulse and the noise from the crosstalk. Crosstalk is considered as a source of noise, in particular the prompt type which has a significant impact on low-level light detection [75].

2.3.6.7 Afterpulses

During the avalanche process, some charge carriers may be trapped in the microcell and released at a later time because of impurities in the silicon [74]. The carriers so released can potentially initiate avalanches and create afterpulses

with a short delay, occurring during the recovery time in the same microcell. Afterpulses are considered another source of noise in SiPM, and the probability of an afterpulse occurring as a function of time can be calculated according to equation 2.7 [67]:

$$P_{ap}(t) = P_t.\frac{exp(-t/\tau_t)}{\tau_t}.P_{tr} \tag{2.7}$$

where P_{ap} is the afterpulse probability, P_t is the trapping probability, which depends on the density of the impurities and the carriers flux during the avalanche process, τ_t is the trapping lifetime, which depends on the band gap energy level and temperature and P_{tr} is the probability of triggering an avalanche, which depends on the applied electric field strength.

2.4 Conclusion

This chapter briefly touched upon the basics of gamma radiation measurements. Scintillators play a considerable role in gamma-ray detection. Modern development in scintillators materials along with the current advancement in photodetector technologies can provide high performance medical imaging modalities with enhanced sensitivity and spatial resolution.

Chapter 3

Overview of medical imaging modalities

3.1 Introduction

Medical imaging plays a critically important role in treatment of numerous diseases. Different imaging techniques are used to differentiate healthy and cancerous tissues in order to perform the best cancer management. This chapter will present the most common imaging modalities in daily routines where examples of anatomical and functional imaging will be discussed providing their strengths and limitations. In addition to that, intraoperative imaging technologies will be addressed followed by the important role of multimodality imaging principles in both pre- and intraoperative procedures. The hybrid gamma camera, which is the main focus of this thesis, will also be described showing the latest research development. Lastly, medical phantoms that have been developed for optical imaging studies will be discussed.

3.2 Conventional imaging techniques

Medical imaging modalities can be mainly divided into two categories; anatomical and functional imaging [76, 77]. Anatomical imaging has been the primary tools for cancer diagnosis, response assessment, and follow-up. Despite the fact

that anatomical imaging provides important information regarding to tumour location, morphology, size and discrimination from adjacent tissues, these technologies do not represent details related to metabolic activity of tissues. On the other hand, functional imaging has the power to provide insight into the lesion biological functions and the surrounding micro-environment, but without anatomical references [76, 77, 78].

The former group typically involves computed tomography (CT), magnetic resonance imaging (MRI) and ultrasound (US). Ionising radiation is employed in CT imaging where X-ray propagates through the patient to reconstruct an image of a chosen two dimensional (2D) slice of tissue. This technique uses differences in X-ray attenuation coefficient, which in turn provides the physical properties of the biological region being imaged [76, 78, 79]. Figure 3.1 illustrates the typical design of a CT device, consisting of an X-ray source emitting a narrow fan of beams typically with energy levels between 20 to 150 keV. Radiation passing through the patient from different angles is recorded by several hundred detectors that are placed in an outer ring.

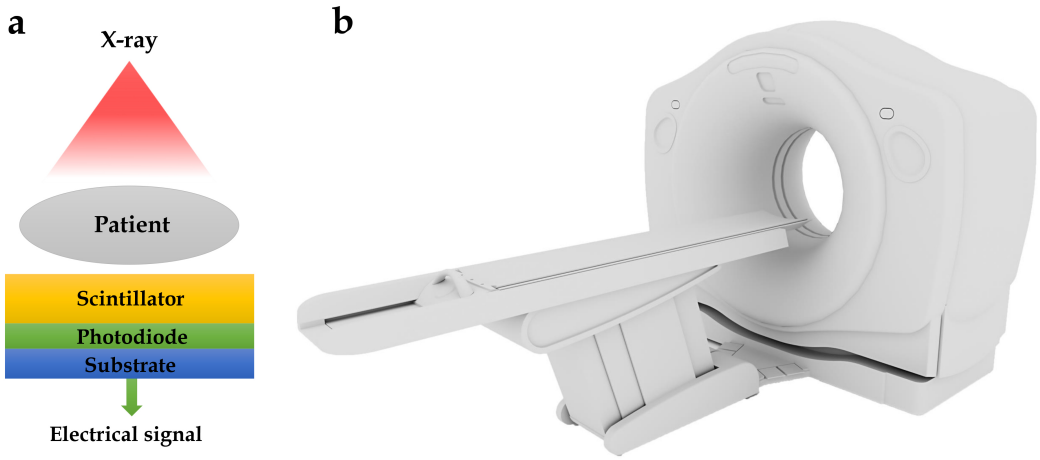

Figure 3.1: Schematic diagram of the CT imaging system. (a) X-ray passes through the patient and then to a scintillator where it is converted into optical light. Optical light is recorded by a photodiode layer and converted to an electrical signal. The substrate layer preserves a flat structure and transfer the signal to electronics to obtain images. (b) shows a clinical CT scanner [76].
.

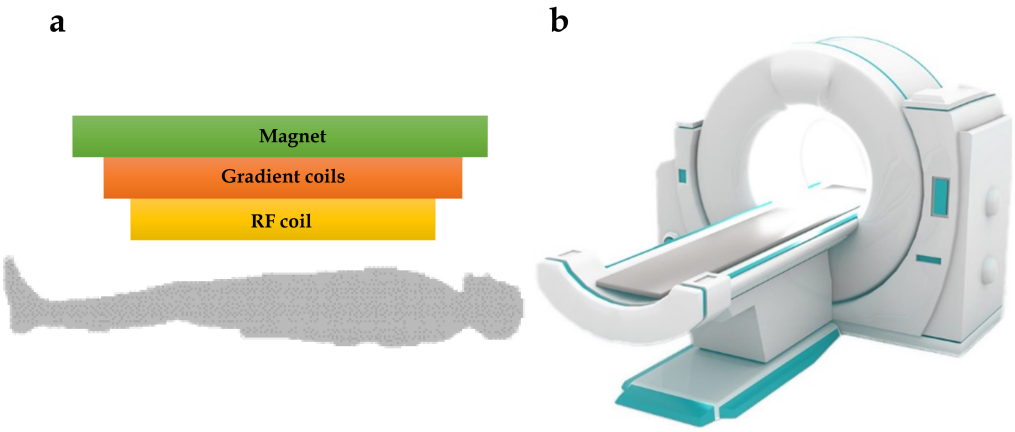

Figure 3.2: (a) Illustration of the basic components of an MRI device. RF coil transmits and receives electromagnetic signal from the patient. The gradient coil alters the magnetic field produced from the magnet source. (b) a clinical MRI device [76].

In contrast, MRI does not expose patients to ionising radiation but mainly exploits electromagnetic field to image proton concentrations (i.e. water). Electromagnetic field is used for protons alignment and relaxation which is associated with electromagnetic emission that can be measured [76, 78]. Compared to CT images, MRI provides better contrast of soft tissues even in absence of a contrast medium. The basic components of a typical MRI machine can be divided into three main components as depicted in Figure 3.2 (a). The first element is the magnet which generates very intense and stable magnetic field commonly between 0.5 and 7T [80]. The main magnetic field is then altered using the second component; the gradient coils. The third part is the radio frequency (RF) coil which is placed close to the body of the patient for transmitting and receiving signals for producing an image.

Another non-ionising technique is ultrasound that uses high frequency sound waves to propagate in the body. US method relies on recording reflected acoustic waves. The main component responsible for generating and recording sound wave is the transducer [81]. In clinical imaging, a transducer usually produces mechanical vibrations between 2 MHz and 20 MHz via materials that have a piezoelectric properties [82].

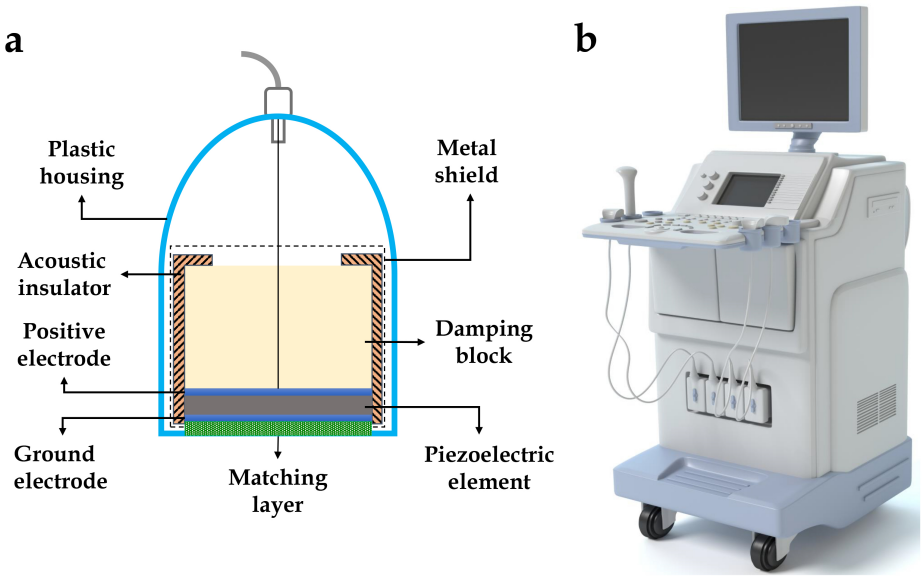

Figure 3.3: (a) illustration of a clinical ultrasonic transducer. Once the ultrasound wave is generated, the reflected echoes vibrates the piezoelectric elements and electrical potential is created across the two electrodes. The vibrating material is fixed to a damping material from one side while flexible layer is used to scan the body surface. (b) an image of US system in clinical use [76].

This effect is described as the ability of some materials, such as quartz, Rochelle salt, topaz, barium titanate and lead zirconate titanate, to generate an electric charge in response to applied mechanical stress. Figure 3.3 (a) demonstrates the basic components of a clinical transducer consisting of a 1D array of hundreds of small packed elements of the piezoelectric material. When a sound wave is sent to the body, the returning echo will set into vibration the piezoelectric elements generating an electrical potential which can be amplified and recorded to produce an image.

The above mentioned anatomical imaging techniques play an indispensable role in medicine for diagnosis, surgical guidance and ultimate treatment outcomes. However, functional imaging methods have been increasingly used in early diagnosis of disease due to the significantly higher detection sensitivity. Molecular imaging offers improvements in the specificity and quantitation of personalised treatment planning [76, 77]. This can be attained by imaging key molecular factors in carcinogenesis in order to treat cancer. There are different functional imaging methods that are commonly performed in nuclear medicine for cancer investigations including gamma camera, SPECT and PET scanners.

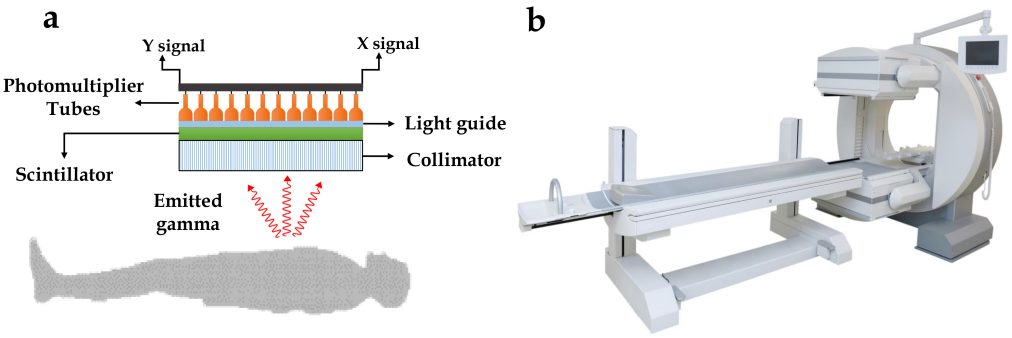

Figure 3.4: (a) basic gamma camera design. The first processing layer, the collimator, restricts the direction of emitted gamma to small angular range to project the spatial distribution of the radiotracer on the scintillator. The emitted light from the scintillator will be directed via a light guide to an array of PMTs. Produced signals that then can be analysed in xy positions producing a 2D image. (b) an image illustrating a clinical gamma camera with two heads [76].

The common device that has been used in nuclear medicine is the gamma camera, also called Anger camera. Figure 3.4 (a) shows a simplified sketch illustrating the main elements of a planar gamma camera consisting of a multi-hole collimator, a scintillator, a light guide, an arrays of photomultiplier tubes and positional and summing circuit. Prior to a scan, the patient is injected with a radioactive isotope (such as ^{99m}Tc) which is subsequently distributed throughout the body based on the tracer's chemical characteristics and the organ physiology. As the radioactive nuclei decays, it emits gamma radiation which consequently is detected by the gamma camera indicating the radio-tracer distribution in two-dimensional image [76, 78].

Since the plain gamma camera generates data in 2D form images, SPECT technique uses a planar gamma camera to reconstruct three dimensional (3D) images by rotating detection systems around the patient either a complete 360° or partial 180° rotation [76, 77]. Therefore, more heads can be used (2 or 3) which improves the sensitivity and image quality by taking a series images from different projections.

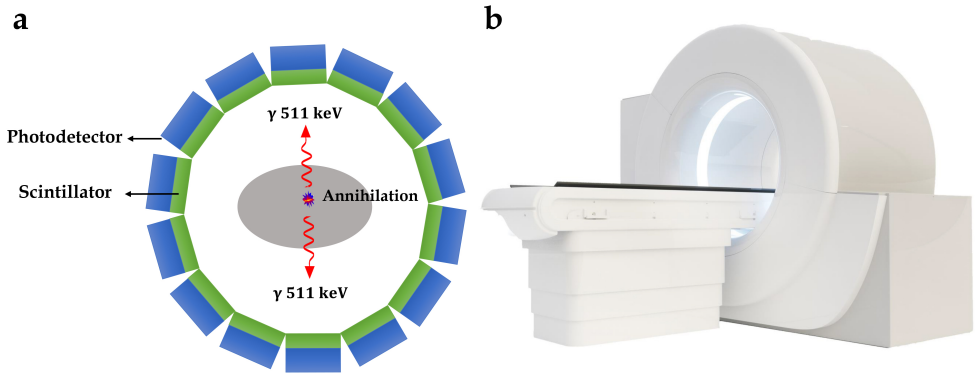

Figure 3.5: (a) schematic diagram represents imaging components of PET scanner to detect two gamma photons with energy of 511 keV. (b) shows an image of a clinical PET device [76].

Another imaging option in nuclear medicine is PET which consists of a scintillator crystals coupled to photodetectors. This device detects gamma photons produced from annihilation process (energy of 511 keV) with the unique coincidence in 180° opposed as shown in Figure 3.5 (a). Due to the nature of the annihilation process, physical collimators can be entirely removed providing much higher sensitivity of PET compared to SPECT system [83, 84].

There are different advantages and disadvantages features of SPECT and PET based on differences in physical, biological and molecular considerations [83, 84]. Without delving into the details of these differences, Table 3.1 summarises some of the main properties of SPECT and PET in the clinical use.

Modality	**Advantages**	**Disadvantages**
SPECT	Resolution limited by technology	Long scan time
	Low dose	Semiquantitave information
	Longer observational time window	Lower sensitivity
	Detecting different gamma energies	
	3D imaging	
	Widespread used	
	Different clinical applications	
	Cheaper	
PET	Physically limited resolution	Short life-time radiotracer
	Higher sensitivity	Expansive device
	3D acquisition	Higher doses
	Quantitative information	Not widely used
		Expensive isotopes production

Table 3.1: Advantages and disadvantages of SPECT in comparison to PET scanners [83, 84].

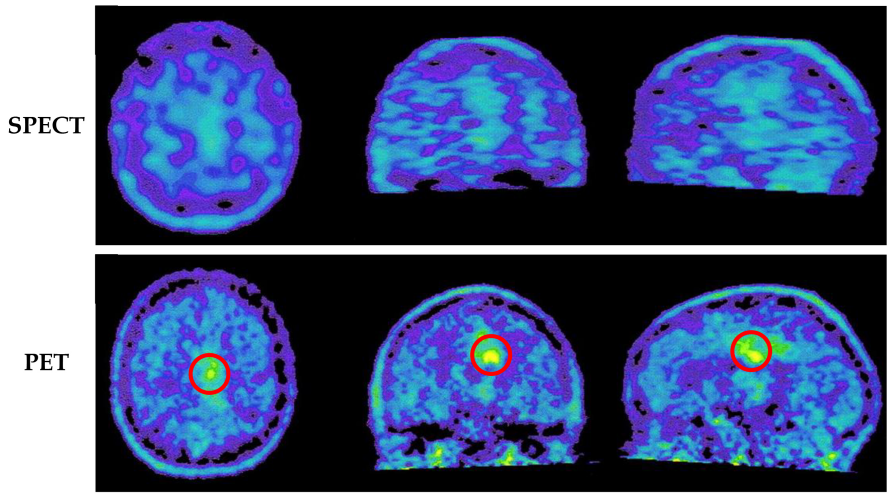

Figure 3.6: SPECT and PET brain scans of 57-year-old woman. Tumour-to-brain contrast was identified by ^{18}F-FET PET showing a low grade glioma (within the red circle) but not on ^{123}I-IMT SPECT images [85].

Figure 3.6 shows also a comparison of clinical case images by ^{18}F-FET PET and ^{123}I-IMT SPECT. This example illustrates that PET scan enables better tumour-to-brain contrast of a low grade tumour (glioma) compared to SPECT images [85].

All aforementioned medical devices are indispensable tools in preoperative cancer identification. Nuclear medicine techniques have long been a useful adjunct in oncology. Preoperative images are normally registered to the patient's anatomy and shown in the context of diagnostics and surgical plans [86]. Further registration between the patient and preoperative images is required to improve cancer tissues positioning during surgery.

In intraoperative imaging guidance US, CT and MRI have been used to accurately discern tumour margins [87, 88, 89]. Nevertheless, US is not always a viable option and has some limitations regarding to, for example, the need of direct contact to the surgical field that may lead to induced ultrasound artifacts [87]. Other devices including CT, MRI, SPECT and PET have several limitations to be used intraoperatively such as cost, complex, requirement of large space, interrupts surgical workflow and lengthens operative time [15, 88]. Therefore, there is a need for simple, small and appropriate imaging modality that provides real-time positioning and does not hamper surgical procedures.

3.3 Intraoperative imaging modalities

There are different intraoperative imaging tools that provide useful cancer surgical-guidance such as non-imaging gamma probes, SFOV gamma cameras and optical imaging. In this section, small scaled imaging tools will be highlighted in the context of tumour resection and SLN mapping.

3.3.1 Intraoperative gamma probes

The first use of radiation detection in surgical theatre dates back to 1949 where a hand-held Geiger-Müller tube was used to detect beta particles in brain tumour patients [90, 91]. Since that time, a tremendous development has been devoted to establish the discipline of radio-guided practice within surgical procedures. This has provided an important real-time information to surgeons resulting in better assessment for cancer resection. In this review, the focus will be only on the use of gamma detection technique in intraoperative procedures.

The basic principle of intraoperative gamma probes is based on the detection of gamma rays emitted from the patient during surgery after the injection of a specific radiopharmaceutical solution. This enables more precise detection of hot spots and better information regarding to the location and the extent of cancer non-invasively [12, 15, 92]. Based on the probe system, gamma photons can be either detected directly using semiconductor materials (cadmium telluride (CdTe), cadmium zinc telluride (CdZnTe), and mercuric iodide (HgI_2)), or indirectly via scintillation crystals (thallium-activated sodium iodide (NaI[Tl]), thallium-activated cesium iodide (CsI[Tl]), samarium-activated lutetium orthooxysilicate (LSO), and bismuth germanate (BGO) [15, 91, 93, 94]. Figure 3.7 (a) shows a simplified illustration of a gamma probe components utilized in surgical procedures.

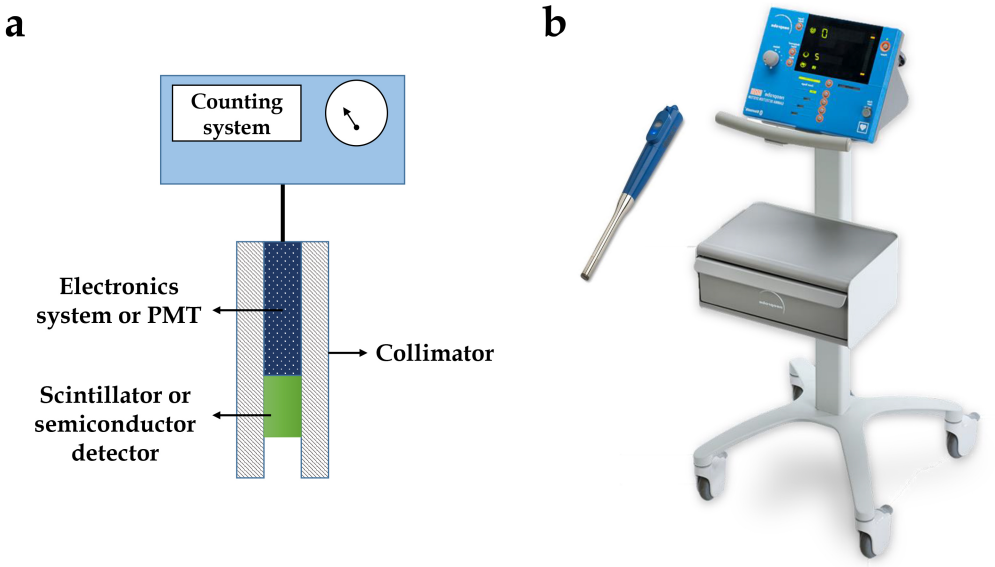

Figure 3.7: (a) a simplified diagram showing the detecting system of an intra-operative gamma probe. Gamma detection system is enclosed in a collimator (typically lead) to reduce scattered background. (b) picture of the Neoprobe gamma detection system [95].

There are advantageous features of using semiconductor detectors in gamma probes compared to scintillation crystal. This includes higher energy resolution due to the direct collection of charges produced by radiation interaction within the semiconductor [91, 93]. Furthermore, semiconductor-based probes have better scatter rejection, more compact design and can be designed with smaller size. However, semiconductors exhibit lower sensitivity, in particular, at medium and high energy gamma photons. On the other hand, a scintillation-type probe has higher sensitivity because of its higher atomic number and density. Nevertheless, due to indirect gamma detection, scintillators show poorer energy resolution and scatter rejection. Table 3.2 shows some of the currently available gamma probe devices in the clinical use.

Probe name & reference	**Detector**	**Diameter (mm)**	**Sensitivity (cps/MBq)**	**Spatial reso. FWHM (mm)**	**Weight (g)**
Crystal Probe[93]	CsI	15	NA	16	400
Gamma finder®[93]	CsI [TI]+PMTs	14	1577	14	210
C-Trak[96]	CsI [TI]+PMTs	11	1500	28	191
Europrobe3[96]	CsI [TI]+SiPMs	15	1900	43	150
Node Seeker^{TM}[96]	LYSO	14	2300	21.2	133
Neoprobe[96]	CdZnTe	14	2200	53	142
Navigator[96]	CdTe	14	510	35	182
Surgeoguide [97]	CsI [TI]+SiPMs	16	1700	75	185
TruNode®[98]	NA	10	3400	14	70
GammaProbe II[99]	CdZnTe	10	1063	20.5	NA

Table 3.2: A summery of the physical properties for some of the commercially available gamma probes.

Intraoperative gamma probes have been frequently used for different clinical applications, such as breast cancer surgery [100], SLN mapping [101], radioguided interaoperative margin evaluation (RIME), melanoma [102], sarcoma [103, 105], lymphoma [104], brain tumour [105], bone lesions [106], gastrointestinal malignancies [107], head and neck tumours [108], thoracic cancer [109], gynecologic malignancies and urological cancer [110, 111]. These tremendous studies have evolved and established what is now considered as an important discipline in surgery due to the high reported detection rates.

However, some considerations should be made related to the limitation of this method. In some cases, it is difficult to identify a small structure lesion when it is located near to a high-activity site, close to the injection site or has an activity below than 1% [112]. Moreover, high detection rates in reported cases not always possible by all surgeons in all cases even with proper exposure and training. Therefore, SVOF gamma camera has been introduced in the surgical use to enhance cancer detection rates.

3.3.2 Small field of view gamma imaging (SFOV)

With the advent of solid state photodetectors and their widely-used applications in nuclear medicine, smaller and more compact designs of gamma camera have allowed SVOF devices. SFOV term means a significantly smaller device than that of conventional large field of view (LFOV) devices in nuclear medicine.

A LFOV camera is usually used to image a relatively large area of the body with limited distance to the organ of interest. In some cases, a LFOV device receives a significant background activity from other organs such as the background resulting from the myocardial intake in breast imaging [113]. This may lead to under- or overestimation of the actual activity leading to limited spatial resolution and sensitivity of the imaged organ.

An intraoperative SFOV gamma camera provides a useful tool to perform radioguided surgery procedures. SFOV gamma cameras can be used with the focus only on a specific region or organ of the body with reduced undesired activity from surrounding tissues [15, 114, 115]. Furthermore, SFOV gamma camera can provide comparable to better intrinsic spatial resolution than LFOV at a reasonable cost-effective. These small devices are portable and have compact design offering simple use in surgical theatre, clinics, cardiology or any other department where the bulkiness of conventional nuclear medicine cameras limits their use [116]. Furthermore, a SFOV can be a useful tool to provide a real-time quantification, spatial orientation on a screen [116, 117]. Figure 3.8 compares LFOV images to SFOV showing two SLNs in a neck region of a rabbit at 4 hr after injection. It can be seen that the SFOV was able to build images of the radioactive uptake in 15 s compared to 600 s by LFOV technology.

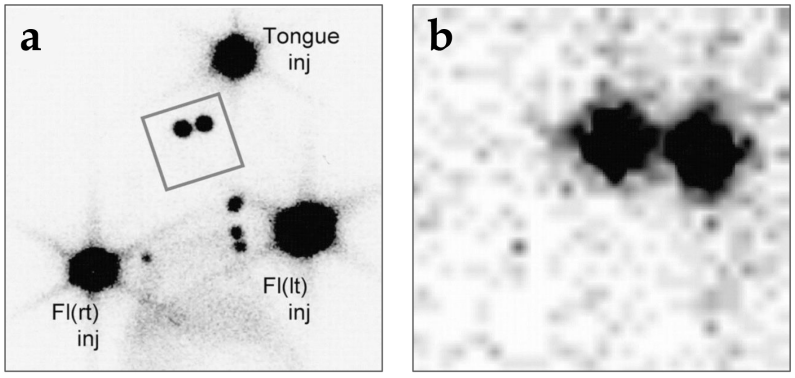

Figure 3.8: Two images compares LVOF to SVOF. (a) shows two SLNs (in the rectangular frame) detected by LFOV technique with acquisition time of 600 s. The same SLNs imaged by SFOV system with acquisition time of 15 s in (b) [118].

In comparison to gamma probes, an additional practical advantage can be achieved by SFOV imaging systems. For instance, several centimetres FOV can

be produced by SFOV gamma cameras compared to less than 1 cm provided by gamma probes [91, 114]. Larger FOV expedites tissue interrogation for large areas with lower statistical noise. Recorded signal then can be displayed as a scintigraphic image rather than a numerical display or a variable-frequency audio output as in gamma probe technique.

To date, several portable and handheld gamma cameras have been designed for intraoperative applications or under development. For example, Sentinella 102 imaging system is manufactured by Oncovision/GEM Imaging Valencia, Spain, shown in Figure 3.9. It utilises CsI [Na] crystal coupled to position sensitive PMTs and exchangeable pinhole collimator with apertures range of 1-4 mm [119]. This camera has been used clinically in different investigations such as SLN detection in breast, penile, prostate cancer and intraoperative imaging for primary hyperparathyroidism.

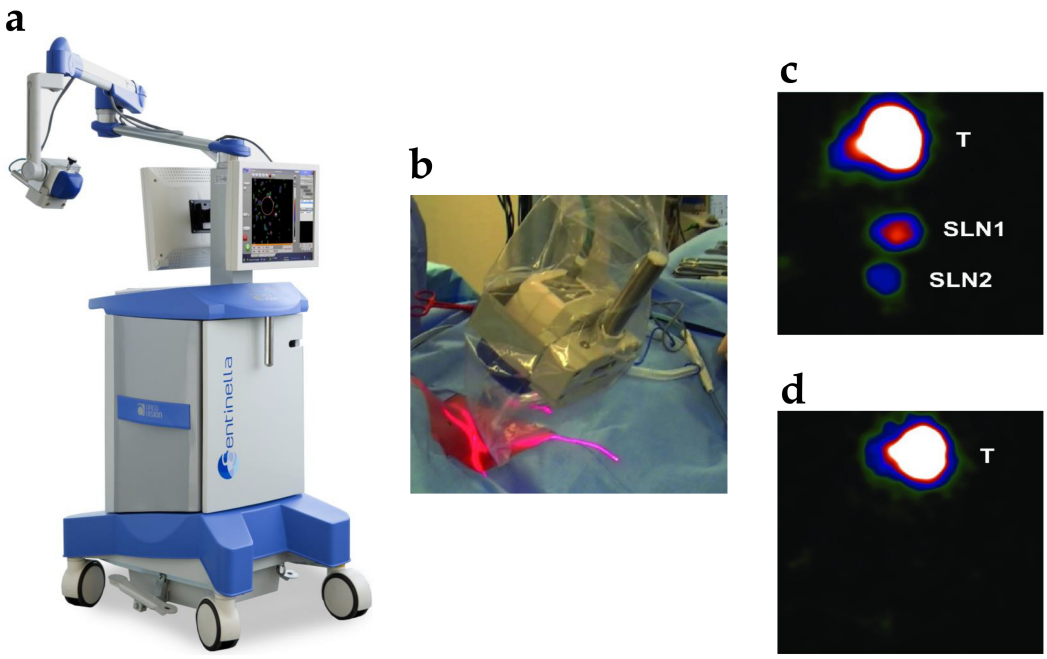

Figure 3.9: (a) the mobile gamma camera Sentinella 102 [119]. (b) Sentinella in the operation room detected the radioactive hotspots in head and neck region. (c) shows (SLN1 and SLN2) pre-excision overview with regards to the injection site (T) and in (d) to confirm removal of SLNs [120].

Another example of a handheld gamma camera based on solid-state detector is CrystalCam, which is manufactured by Crystal Photonics, Berlin, Germany. It is equipped with CdZnTe semiconductor detector (5 mm thickness) and provides FOV of 40×40 mm^2 [121, 122]. The CrystalCam and an example of clinical images are demonstrated in Figure 3.10, where CrystalCam was compared to SPECT/CT modality. This camera has been used to visualize the location of SLN in breast cancer and melanoma [123, 124]. Table 3.3 summarises different SFOV gamma cameras that have been intended for intraoperative cancer treatment. Note that this table is not for comparison purposes as resulted sensitivity and energy resolution were obtained using different imaging systems with different procedures at different energy ranges.

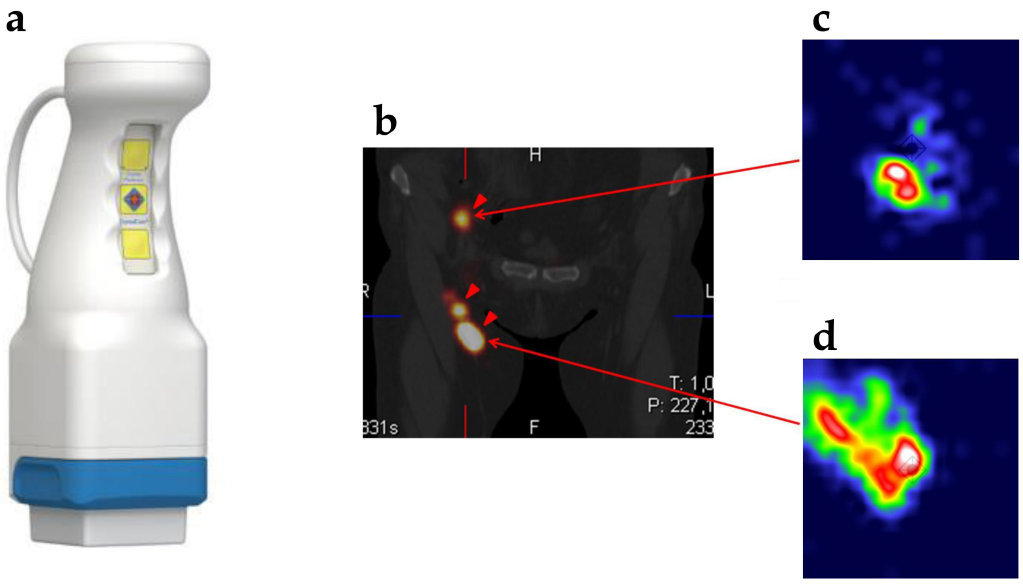

Figure 3.10: (a) picture of handheld gamma camera CrystalCam [121]. (b) acquired image of melanoma cancer using SPECT/CT with acquisition time (20s/angular increment). Images obtained pre-operatively using CrystalCam showing (c) the upper and (d) the lower lymph nodes at 20 s acquisition time [125].

Name & reference	**Detector system**	**FOV (cm)**	**Weight (kg)**	**Energy range (keV)**	**Collimator type**	**Sensitivity (cps/MBq)**	**Energy res. (%), ^{99m}Tc**
SURGEOSIGHT-I[97]	CsI [Na]+PSPMTs	4.9×4.9	NA	140	Parallel hole	142	21
POCI[116]	YAP [Ce]+IPSDs	4×4	1.2	35-247	Parallel hole	200	38-^{57}Co
POCII[116]	CsI [Na]+IPSDs	4×4	1.2	105-175	Parallel hole	290	32
Minicam®[116]	CdTe	4.9×4.9	0.7	20-200	Parallel hole	NA	7
MinicamII®[116]	CdTe	4×4	0.7	30-200	Parallel hole	200	7
Sentinella 102®[119]	CsI [Na]+IPSDs	4×4	1	50-200	Pinhole	90-900	15.9
eZ-SCOPE®[126]	CdZnTe	3.2×3.2	0.8	71-364	Parallel hole, pinhole	184	8.6
CrystalCam [121]	CdZnTe	4×4	0.8	50-250	Parallel hole	237	7
GE camera[127]	CdZnTe	4×4	1.2	40-200	Parallel hole	100	8
MediPROBE[128]	CdTe	14.1×14.1	1.5	60-140	Pinhole	6.5-33	NA
SSGC clinical-type[129]	CdTe	4.4×4.4	1.4	550	Parallel hole	150-1600	6.9
MRG15[130]	CsI [TI]+SiPMs	1.3×1.3	0.32	140	Parallel hole	149	38.9
MGC500[131]	CdTe	4.5×4.5	NA	60-300	Parallel hole	436	5.5
CarolIRes[132]	GSO [Ce]+PSPMTs	4×4	2.5	140	Parallel hole	130	45-^{57}Co
GammaCAM/OR[133]	NaI[TI]+PSPMTs	12.7×12.7	10	NA	Parallel hole	83.3	NA
DEPICT[134]	CZT	4.4×4.4	NA	30-3000	Parallel hole	NA	2.9-^{131}I
IP Guardian II[135]	CsI [TI]+PSPMTs	4.4×4.4	1.2	50-250	Parallel hole	211	19.3
IHGC[136]	NaI[TI]+PSPMTs	5×5	1.1	30-300	Parallel hole	270	12
Round GC[37]	$LaBr_3$+SiPMs	6 diameter	1.4	140	Parallel hole	73-481	21.1
TReCam[137]	$LaBr_3$[Ce]+MAPMTs	4.9×4.9	2.2	140	Parallel hole	300	11

PSPMTs: Position Sensitive Photomultiplier Tubes, IPSDs: Intensified Position-Sensitive Diodes, SiPMs: Silicon Photomultipliers, MAPMTs: Multi-Anode photomultiplier Tubes, NA: Not Available.

Table 3.3: Physical and performance characteristics of different SFOV gamma cameras.

However, the main inadequacy of current intraoperative nuclear medicine imaging is the lack of good spatial resolution that allows clinicians to achieve a higher contrast among malignancies and adjacent normal tissues [16, 18]. The background radiation emitting from surrounding tissues and organs can affect detection ability of tumours. Moreover, radioisotopes are not always available to all treatment centres and their preparation requires experienced staff working in licensed nuclear medicine departments [17, 138]. Beside the relatively high cost of this technique, it also exposes patients and workers to ionizing radiation that may increase the probability of initiating a new cancer in the future [17]. Furthermore, several minutes acquisition times are usually required to build up an image of the target without anatomical information. Finally, and since the patient needs to be anesthetised, the time window between the radiotracer injection and operation is limited.

3.3.3 Optical imaging

Optical imaging techniques have received a great deal of attention for image-guided surgery due to ease of use, availability with various contrast agents, high resolution, high detection rates, low cost and provide direct feedback of the natural surgical view [17, 138, 139]. In comparison to preoperative imaging modalities such as CT, MRI and PET, optical imaging can detect a small lesion in the range of 10 μm making it particularly appealing for early cancer detection [138]. This feature could have a significant impact on cancer surgical outcome. There are currently various optical technologies that have been developed at different stages or still in clinical translation. Table 3.4 compares optical imaging to the aforementioned conventional modalities for cancer detection.

Technique	Information	Resolution	Molar sensitivity (M)	Depth	Ionising radiation	Cost
CT	Anatomical	100 μm- 1 mm	NA	Whole body	Yes	$$
MRI	Anatomical, functional	100 μm- 1 mm	10^{-3}–10^{-5}	Whole body	No	$$$
US	Anatomical, functional	100 μm- 1 mm	$\sim 10^{-12}$	$<$ 10 cm	No	$$
SPECT	functional	5-10 mm	10^{-10}–10^{-11}	Whole body	Yes	$$
PET	functional	$\sim$ 5 mm	10^{-11}–10^{-12}	Whole body	Yes	$$$
Optical	Anatomical, functional	10 μm- 10 mm	10^{-9}–10^{-17}	$<$ 5 cm	No	$

Table 3.4: Comparison of different imaging technologies used for cancer detection. Adapted from [138].

In medical investigations, optical tomography can be mainly classified based on electromagnetic wave used visible (400–750 nm) or near infrared (NIR) light (750–1000 nm) [140, 141]. Figure 3.11 demonstrates the optical imaging range based on the electromagnetic spectrum.

Since the early days of medicine, physicians have used their own vision and tactile feedback to diagnose and treat diseases [141]. In 1950, surgeons started using magnifying lenses and microscopes in surgical rooms for cancer resection [142]. Endoscopy is considered as the simplest example of optical imaging where a flexible tube consists of light and camera is used to illuminate internal organs or tissues to investigate causes of symptoms. Optical coherence tomography (OCT) is another technology using backscattered light measurements to

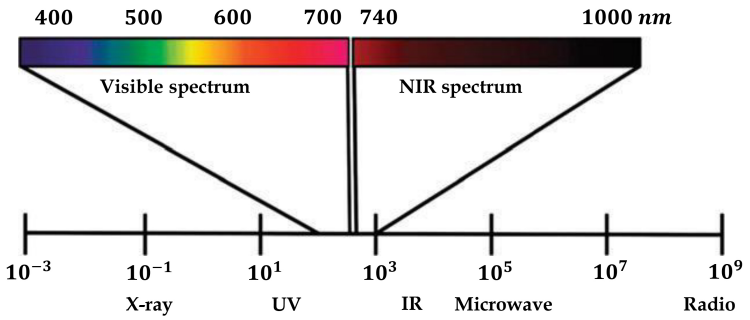

Figure 3.11: Optical imaging related to the electromagnetic spectrum. The visible spectrum (400–750 nm) and the near-infrared (NIR) spectrum (750–1000 nm) are highlighted. NIR is not visible to the human eye and can be detected only by an IR camera [141].

obtain tomographic internal microstructure of the biologic tissues [143]. The OCT provides image resolution of 1-15 μm up to 2-3 mm deep in most tissues. This technology has a variety of applications in ophthalmology, coronary artery disease, neoplasia and guiding surgical intervention [144].

However, surgeon's visual inspection is still restricted inherently to superficial contrast. Moreover, unaided eye can only identify anatomical structures, but it is not able to distinguish diffuse cancer from normal tissue merely on molecular-based features [141]. Therefore, precise tumour detection can be subjective and depends significantly on surgeon's experience. This may lead to several undesired consequences such as incomplete tumour resection, removal of healthy tissue and iatrogenic side effects [17, 138].

Various approaches have been developed to enhance surgeons' vision via the use of targeted and non targeted agents, which can reveal otherwise invisible disease bio-markers [138]. Visible dyes have an obvious role in oncology which are widely used for cancer demarcating in all stages starting from initial identification, histopathological confirmation, biopsy and intraoperative guiding. There are various visible dyes types that have been used for SLN mapping, melanoma and surgical guidance. For example, methylene blue is considered as the visual tracer of choice for different surgical procedures due to its reported efficiency, wide availability and low cost [17]. Regardless of the advantageous features of the visible blue dye, it has some drawbacks that make it an undesirable option in many cases. The main limitation of this method is the difficulty to locate deep-seated targets due to its limited penetration ability, a few micrometers, in tissues and dense fat [17, 145].

Other technologies dedicated to tissue interrogation intraoperatively are combining both; contrast agents and imaging systems. These technologies include, for example, bioluminescence imaging (BLI), Cerenkov luminescence imaging (CLI) and NIRFI. The BLI and CLI imaging system will be described succinctly, where more details will be given for florescence imaging as it is a part of this thesis.

In BLI imaging system, a CCDs camera is used to identify light signals (560 nm) produced from enzymes such as luciferase. This imaging modality remains clinically unavailable and currently studies are focusing on different diseases amongst cancer in animal models [146, 147].

The CLI is also a multi-modality emerging imaging technique that utilises emitted visible light from radioactive materials used in nuclear medicine applications

particularly PET scanners [19, 148, 149]. When a charged particle (electron and positron) travels with a velocity higher than that of light in a dielectric medium, prompt bluish-white light emitted due to relaxation in the medium. This prompt light can be detected using an ultra sensitive CCDs camera in dark conditions as used in BLI. Different preclinical and clinical trials have proposed this novel technology for image-guided cancer surgery and radiotherapy driving a widespread clinical adoption.

The NIRFI is based on detection of light emission after the absorption of electromagnetic energy. When a fluorescent molecule, called a fluorophore, is exposed to light at a particular wavelength, absorption of the photon creates an excited electronic state. In the order of a few nanoseconds, the electron relaxes toward the lowest vibrational energy level and emits a photon [17]. Emitted light then can be detected using a suitable imaging system. Figure 3.12 illustrates the three different optical modalities using different molecular agents but almost have similar imaging systems. Some of the other optical imaging technologies are summarised in Table 3.5.

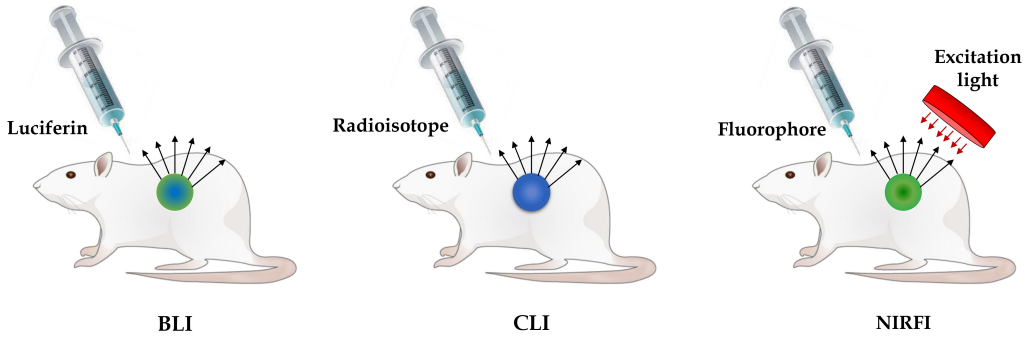

Figure 3.12: A representation of optical modalities that use different molecular dyes and have been used in preclinical and clinical trials for molecular-based cancer detection.

Technology & reference	**Working principle**	**Resolution**	**Depth**	**Advantages**	**Limitation**
OCT [143]	Described in the text	1 μm	2-3 mm	High spatial resolution, 3D imaging possible	Expensive, lack of specificity, limited depth
BLI [146, 147]	Described in the text	1-4 mm	~ 10 mm	Cheap, short scanning time, high sensitivity, easy to use, 3D imaging possible	Low resolution, lack of clinical translation, complex contrast agent
CLI[148]	Described in the text	0.3 -2 mm	10-20 mm	Cheap, real-time imaging, tested clinically,	Low sensitivity, relies on radioactive distribution, limited depth, 2D only
NIRFI[17]	Described in the text	50 μm- 5 mm	10-30 mm	Real-time imaging, cheap, easy to use, applied clinically	2D imaging, resolution decreases with depth
TPM [150]	Tow photons with identical or different wavelengths excite a molecule to construct an image	1 μm	1-2 mm	High spatial resolution	Expensive, limited FOV
Raman[151, 152]	After incident photons, different frequencies of scattered light are used to determine molecular compositions	NA†	<1 μm- 1mm	High specificity, no contrast media needed	Limited depth, slow, difficult to analyse
DOT[153]	Intensities measurements of light when propagating in tissues	> 1 mm	100 mm	3D imaging possible	Slow, limited FOV
OPAI[154]	Detection of acoustic signals produced after light absorption in tissues	50 μm- 1 mm	50 mm	High resolution, high penetration ability, 3D imaging possible	Expensive, difficult to analyse

OCT: Optical Coherence Tomography, BLI: Bioluminescence Imaging, CLI: Cerenkove Luminescence Imaging, NIRFI: Near Infrared Fluorescence Imaging, TPM: Two-Photons Microscopy. DOT: Diffuse Optical Tomography, OPAI: Optoacoustic Imaging. † NA: not available as Raman technique here provides spectroscopic output from sub-millimetre region of tissue. However, Raman imaging is used in microscopy.

Table 3.5: Summary of operating principles and performance for some of optical imaging techniques in cancer detection.

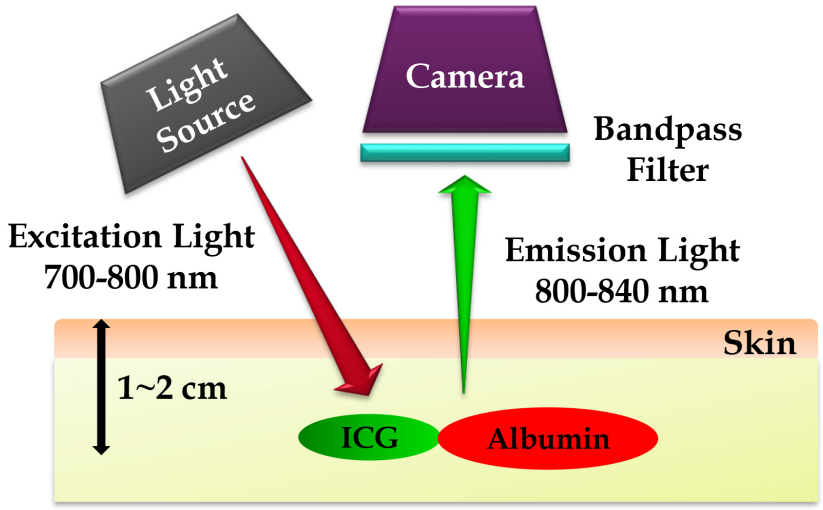

Figure 3.13: The basic components of a NIRF imaging system. A fluorophore (ICG) is injected into the body and attached to albumin in the blood. Photons in the range of 800 nm are emitted using excitation light and can be detected using filters and an imaging system [17].

NIRFI is a novel technology that has the potential to assist surgeons in real-time imaging. More details about this approach in clinical applications are given in Chapter 4. The basic elements of a NIRFI detection system are a light source for excitation, NIR fluorescent agents, filters, collection optics and a NIR camera as shown in Figure 3.13.

Indocyanine green (ICG) is considered the most common NIRFI contrast agent used for cancer identification [156, 157, 158]. This dye has been approved by the Food and Drug Administration (FDA) and the European Medicines Agency (EMA) for differnt clinical applications [17, 157, 158]. Another emerging NIRF dye is the IRDye® 800CW that has been introduced for molecular imaging. It is still in the evaluation stages and has been tested with animal models and clinical trials in Europe and the U.S. In comparison to ICG, IRDye® 800CW showed lower toxicity and faster attachment to the biomolecules [159, 160, 161]. Table 3.6 summarises the most common fluorophores that have been used clinically or being under evaluation.

Fluorophore	**Absorption peak (nm)**	**Emission peak (nm)**	**Quantum yield**	**Extinction coefficient** $(M^{-1}cm^{-1}L^{-1})$	**FDA/EMA approved**
Fluorescein [162]	490	520	0.93	77000	Yes
ICG[163]	780	810	0.03	150000	Yes
MB[164]	665	685	0.05	80000	Yes
IRDye®[165]	785	830	0.034	180000	No
Cy5.5 [166]	675	694	0.28	250000	No
Cy7[166]	743	767	0.28	200000	No

Table 3.6: Summary of the common intraoperative NIRFI dyes for cancer treatment. Extinction coefficient refers to how strongly the fluorophore absorbs light at a given wavelength per molar concentration.

In most imaging systems, the excitation source, in the NIR wavelength range of 700-1000 nm, is directly positioned either above, below, or to the side of the imaging field [167]. There are three common types of light sources that can be used to illuminate fluorophore molecules: arc lamps, light emitting diodes (LEDs) and laser diodes. Arc lamps are widely used because of their high optical power output and broad emission spectrum [156, 167]. Recently, LEDs have gained increasing interest even though with their lower-power output is a drawback [156]. This is owing to their lower cost, narrower wavelength range, longer lifespan, lower energy consumption and lower heat generation. The laser-based imaging system produces highly monochromatic and coherent light with very narrow spectral bandwidth. Nevertheless, the higher price of laser sources and safety issues associated with laser bio-effects have limited the uptake of these systems [156, 168].

CCDs imaging technology is the most common sensor that has been used in interaoperative imaging systems [156, 167]. CMOS sensors are considered as an alternative option to CCDs because of reduction in size, power consumption and increased frame rate, but their QE also remains low with high readout noise [167]. The new generation of scientific CMOS (sCMOS) image sensor has been introduced achieving the desired properties, such as the extremely low noise, rapid frame rate, high resolution and better QE at 800 nm. Table 3.7 concludes some of the common intraoperative optical imaging device that are commercially available or under development.

Name & reference	**Detector**	**Sensor resolution**	**Excitation source**	**Maximum FPS**	**Detection limits**	**Room light**	**Colour and fluorescence overlay**	**FDA approved**
SPY Elite®[168]	CCD	1024×768	laser (805 nm)	20	5 nM	Dim	No	2007
PDE^{TM} [168]	CCD	640×480	LEDs (760 nm)	20	15 nM	Dim	No	2014
Quest Spectrum®[168]†	CCD	640×494	LEDs	20	10 nM	On	Yes	2015
EleVision^{TM} [168]	CCD	960×720	laser (805 nm)	NA	50 pM	Dim	Yes	2015
Fluobeam 800^{TM}[168]	CCD	720×576	laser (750 nm)	25	5 nM	Dim	No	2017
Solaris [168]	sCMOS	1024×1024	LEDs	100	1 nM	On	Yes	No
LAB-Flare [168]	CCD	1024×1024	LEDs (760 nm)	30	NA	Dim	Yes	No
Bio-inspired [169]	CMOS	1280×720	laser (780 nm)	40	100 pM	On	Yes	No

†It was called Artemis previously.

Table 3.7: Summary of the optical performance of various NIRFI systems.

3.4 Towards multimodality imaging techniques

Multimodality imaging is defined as the combination of two or more imaging technologies into a synchronous acquisition procedure. This new form is synergistic in a way that provides functional information within the anatomical context in a single imaging session. The first device that combines a simultaneous imaging of CT and SPECT was pioneered by Hasegawa in 1990, while the first commercial introduction of SPECT/CT and PET/CT was in 1998 [171]. There are different approach of hybrid imaging modalities currently in existence including US/MRI, SPECT/CT, PET/CT, SPECT/MRI and PET/MRI. These advanced technologies have the potential to aid the development of personalized, molecular medicine primarily in oncology. Figure 3.14 shows an example of transversal simultaneous datasets of a brain tumour using hybrid PET/MRI modality.

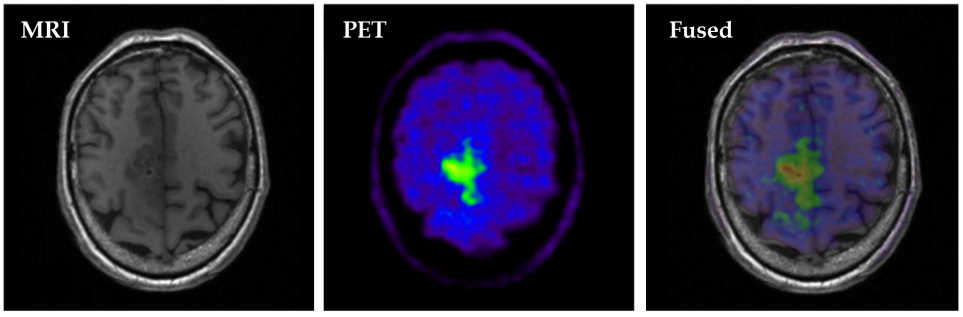

Figure 3.14: PET/MRI image acquired simultaneously for a 60-y-old patient with anaplastic astrocytoma [172].

In intraoperative cancer navigation, different multimodal gamma-optical techniques have been employed for tumour margins delineation and SLN mapping. This includes the use of gamma probes with visible dyes, SFOV gamma camera with optical imaging and gamma-NIRF techniques. The most common procedure is the injection of a gamma emitter alongside the injection of a visible blue dye [17, 173]. This method has been evaluated widely in many clinical cases. For example, in a group of breast cancer patients, when ^{99m}Tc was injected alone, SLN identification rate was 88.6% compared to 80.3% when the blue dye was injected only. The concurrent use of both techniques increased the identification rate to reach about 95.7% [24]. Such a significant improvement in SLN localization rate yields to a better surgical outcome and more reduction of morbidity.

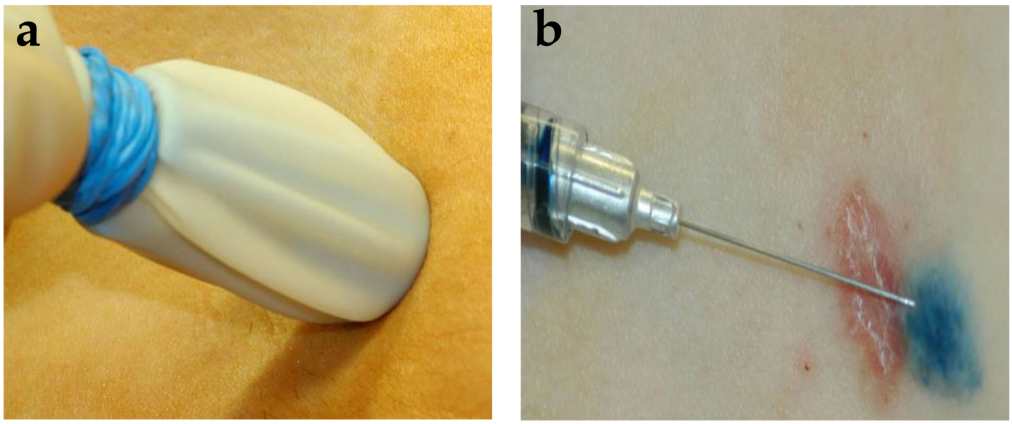

Figure 3.15: (a) after the injection of the radioactive fluid, gamma probe aids surgeons to locate the target. (b) blue dye is then injected during the surgical procedure to visually allows complete resection of the cancer target [174].

Figure 3.15 shows a melanoma case that injected with a blue dye and gamma source to locate SLN. The gamma probe is used to locate the target while the blue dye visually labels cancer tissue in order to eradicate it completely.

Hybrid gamma-optical imaging can also enhance surgical accuracy in SLN detection and tumour delineation. The Sentinella, a SFOV gamma camera has been mentioned previously, was adapted for hybrid gamma using two optical cameras [19, 120]. This system has been evaluated intraoperatively showing useful method to determine the position and orientation of the gamma imaging FOV. Another example of gamma-optical multi-modality is HGC, which this thesis is focusing on, will be mentioned in details in the following section.

The hybrid gamma-NIRFI has also emerged as a new hybrid intraoperative imaging tool. This is due to the higher penetration ability of NIRFI compared to optical imaging. Therefore, NIRFI provides a high resolution real-time imaging combined with the high penetration depth of gamma system to localise sources at depth within the body [17, 19, 156]. Figure 3.16 illustrates the current image-guided surgery where surgical plan can be decided based on a suitable imaging system in the clinic while intraoperative hybrid imaging tool aids surgeons in the operation room.

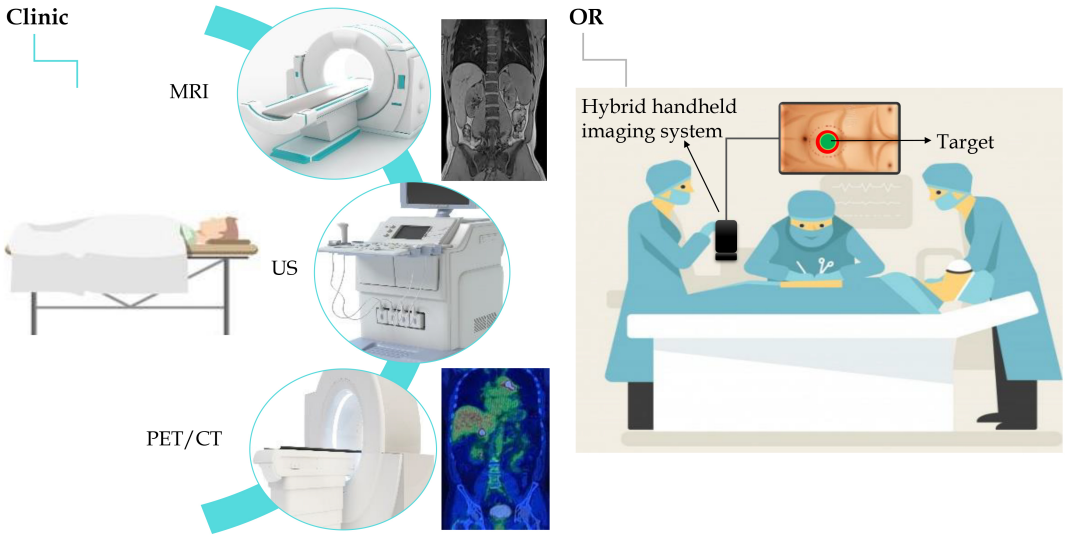

Figure 3.16: Conventional or hybrid preoperative imaging modalities assist in diagnosis and surgical plans in the clinic. Portable hybrid gamma-optical imaging technique can further help surgeons to accurately detect and remove diseased tissues in the operation room.

3.4.1 The hybrid gamma camera (HGC)

The hybrid gamma camera was developed by the BioImaging Unit at the Space Research Centre (SRC), University of Leicester. The first SFOV gamma camera was designed in 2003 and called the high-resolution gamma imager (HRGI) [25]. It was based on 500-µm-thick gadolinium oxysulphide Gd_2O_2S scintillation layer attached to a CCDs device with a sensitive area of 20 mm × 30 mm. The HRGI provided a spatial resolution of 0.6 mm.

In 2006, Lees et al. explained the development of a scintillator-CCDs based camera to investigate detection of radioactive uptakes [175, 176, 177]. The camera was upgraded with a 500-µm-thick terbium-doped gadolinium oxysulphide Gd_2O_2S [TB] scintillation layer. A Peltier cooling system was used to reduce temperature to around -5 °C to suppress the dark current to 10 e^-/pixel/second. A parallel hole lead collimator was used while the detection head was enclosed in a plastic container for protection purposes. This camera design was small enough to be a handheld.

Further development was continued on the camera and a novel prototype named the mini gamma ray camera (MGRC) was built. This camera offered an improved spatial resolution images to be used in nuclear medicine imaging. The

scintillation crystal was changed from Gd_2O_2S [TB] to a thallium-doped caesium iodide Csl[TI] [176, 175]. The scintillator then was attached optically to back-illuminated EMCCD using optical grease. The detector system then was encased in a 4 mm thick lead shield in order to reduce the background and scattered radiation level [178]. The MGRC design allowed different interchangeable collimators systems such as parallel hole collimator or pinhole collimator. Different diameter pinhole collimators (0.5 and 1.0 mm) with angular apertures of 60°, were made from tungsten discs (6 mm thick). The MGRC was used for photon energy in the range between 20 to 140 keV. Therefore, images of radioactive sources were obtained using interactive data language (IDL) software [176, 177]. This imaging design offered a spatial resolution of ~1 mm.

Lately, the camera was further improved with better outer and more compact design and called the compact gamma camera (CGC) [176]. The current design includes a cooling system consists of a praffin-based phase-change material (PCM) that enables CCD temperature reduction to about -13 °C.

Taking into account the importance of multimodality imaging techniques in enhancing theranostic procedures of cancer, the CGC was combined with an optical imaging camera and called the HGC [179]. The current design of the HGC consists of 600 µm thick columnar CsI [Tl] scintillator coupled to back-thinned EMCCD [175, 180]. The back end of the EMCCD is thermally coupled to a thermoelectric cooler (TEC) and to a phase-change material. The detector system is encased in an Al chamber maintaining a pressure level of 1 Pa to protect the hygroscopic scintillator CsI [Tl] and to improve cooling performance. The chamber is shielded by 3 mm thick tungsten material. A knife edge pinhole collimator is used with (0.5 or 1 mm) diameter and 60° acceptance angle to increase imaging FOV. An optical system combined of a miniature optical camera and a mirror is fitted to the collimator ensuring that both systems FOV are independent on the distance between both imaging systems and the radioactive source. The mirror is tilted with 45° and reflects optical photons towards the optical camera while gamma ray passes through it with minimal absorption (<1%) to reach gamma detection system [175, 176, 177]. Therefore, gamma-optical images can be obtained simultaneously offering a hybrid imaging tool. Figure 3.17 displays the development stages of the HGC showing images of previous and current camera designs. It also shows hybrid optical-radioactive uptakes of preclinical and clinical images of thyroid and lacrimal glands.

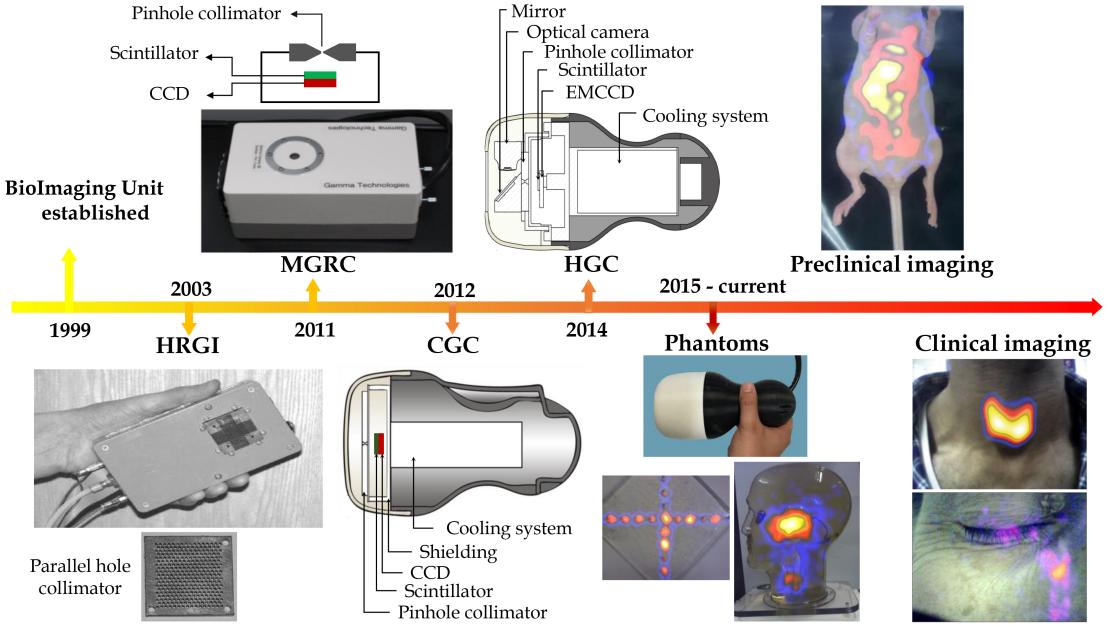

Figure 3.17: Development stages of the HGC starting from the first prototype (HGRI) to hybrid clinical images of the thyroid and lacrimal glands.

The HGC has been evaluated in various configurations including *in vitro* imaging using different phantoms, clinical investigations for SLN mapping, thyroid and lacrimal drainage imaging [181, 182, 183, 184]. It has been also used to estimate the depth of a radioactive source below the surface. Furthermore, hybrid NIRF-gamma imaging was tested showing the feasibility of a new modality to be added to the HGC [184]. Figure 3.18 illustrates the initial hybrid NIRF-gamma images of Eppendrof tube contained ^{111}In radionuclide tracer and ICG fluorescence dye.

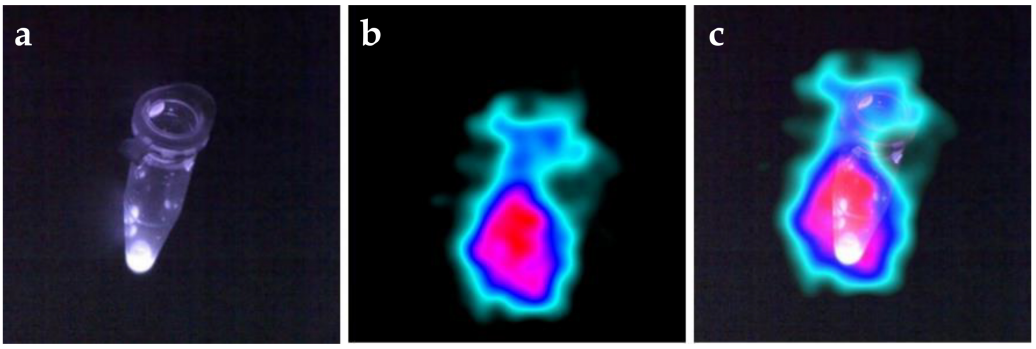

Figure 3.18: Images obtained using the HGC for ICG fluoresence dye (a), gamma image of ^{111}In source (b) and fused image of both modalities in (c) [184].

3.5 Phantoms in optical imaging

Similar to any new diagnostic or therapeutic modality, the development of optical imaging technology requires appropriate phantoms that have the same physical and biological properties of human tissues. Measurements on tissue equivalent phantoms have a crucial role in evaluating the performance of the optical system, validating imaging algorithms, characterisation and optimisation before translating into clinical practice and routine calibration [185]. For these reasons, many materials have been proposed to simulate the characteristics of biological tissues in optical imaging studies during the past two decades.

Phantoms can be fabricated either in solid or liquid forms. In general, a typical optical phantom is made of three main components: a bulk material (water, silicone, agar gel, epoxy resin), an absorbing material (India ink, printer toner, black silicone, food colouring) and a scattering material (milk, non-dairy creamer, intralipid, titanium oxide, aluminum oxide, silica microspheres) [185].

Liquid-based phantoms (mainly water-based) are considered as the most appropriate type for evaluating optical imaging systems. Liquids allow a homogeneous medium in which small solid targets can be inserted with different sizes at different depths [185]. However, there are some drawbacks of liquid-based phantoms including the need of a solid barrier to contain the liquid, difficult to handle in daily routines, short shelf-life and difficulties in moulding a realistic organ shapes. These disadvantages can be avoided using solid phantoms that have been introduced with various recipes mimicking different tissues and human organs [185].

Silicone rubber, in particular, has allowed simulating not only the optical properties of tissues but also constructing a more realistic human organ. For example, a highly scattering material called Delrin was investigated for mimicking human tissues by Berg et al. [186]. Jiang et al. used room-temperature vulcanizing (RTV) silicone to simulate tissues for NIR tomography application [187]. Different other mixtures were investigated including for example; paraffin wax with colouring pigment [188], agar with ink and intralipid [189], haemoglobin and intralipid in gelatine [190], polyester resin with dye and titanium dioxide particles [191], dye and quartz glass spheres in polyester resin [192], polyvinyl alcohol (PVA) slime with titanium dioxide [193] and cosmetic powder with aluminium oxide particles in silicone rubber [194].

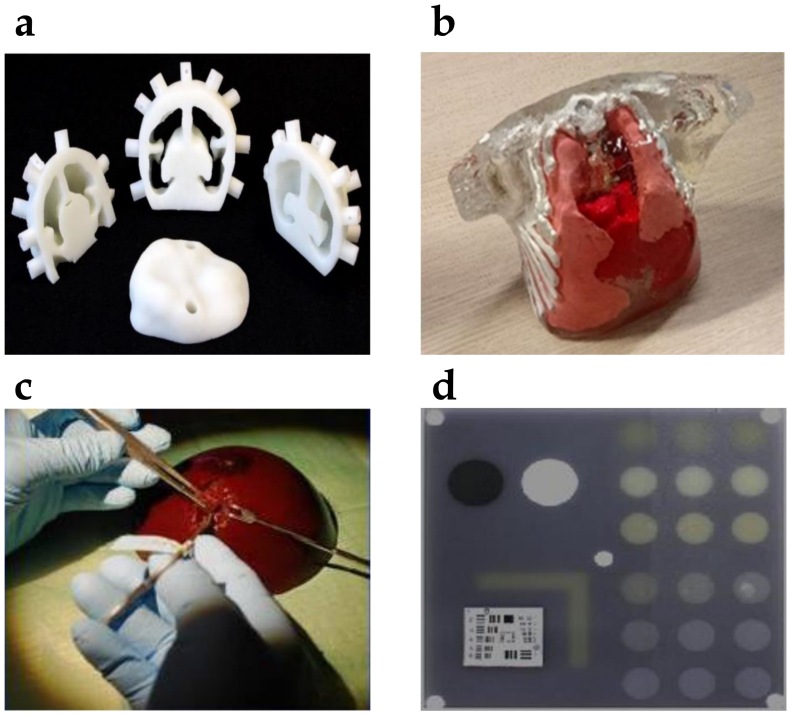

Figure 3.19: Examples of phantoms designed for optical imaging system evaluation. Recipes and 3D printing technology simulating an infant brain (a) and the upper part of an infant in (b) [195, 196]. (c) shows a moulded breast shaped phantom made of silicone to simulate breast surgery using ICG and an imaging system [200]. (d) a comprehensive solid phantom to evaluate NIRFI system using a single snapshot [201].

More benefits of silicone rubber could be achieved in simulating soft tissues and moulding the desired shape and thicknesses such as skin layers, breast and head and neck geometries. The advent of 3D printing technology has also enabled more realistic phantoms for optical imaging. A recipe and method of 3D printing brain phantom was presented by Dempsey et al. [195]. They created a tissue-equivalent premature infant brain based on MRI atlas data. Larsson et al. simulated the upper part of an infant representing; lung, heart, bones and muscles based on segmented CT images [196]. The 3D model is designed to study an optical technique called gas in scattering media absorption spectroscopy (GASMAS). Other examples of phantoms that have been also used for NIRFI system evaluation include; chicken breast tissues [197], bovine muscle [198] and gelatine dough-flour based compositions [199]. Figure 3.19 demonstrates different examples of phantoms that have been designed to evaluate optical imaging systems.

3.6 Conclusion

Conventional medical imaging techniques play an indispensable role for a large number of diagnostic and therapeutic procedures. This chapter demonstrated the fundamental aspects and basic components of routinely used medical imaging devices. It also reviewed the currently available intraoperative gamma probes, SFOV gamma imaging systems and optical imaging techniques for cancer detection. The characteristics and operating principles of the various medical imaging tools were compared and discussed. The HGC properties and its development stages have been also highlighted.

Chapter 4

Characterisation of NIRF imaging systems intended for hybrid gamma-NIRF image-guided surgery

4.1 Introduction

Cancer remains one of the leading causes of morbidity and mortality worldwide [202]. Surgery is the oldest form of treatment and is still currently considered the most effective method for solid tumour resection. Although modern preoperative imaging technologies have significantly improved the success of cancer surgery, there is still an unfulfilled demand for additional guidance during the surgical procedure [5, 17]. This stems from the fact that surgeons cannot precisely detect or 'see' the target tissue margins that need to be resected, whilst preserving non-diseased tissues.

Recently, a growing body of research has shown that fluorescent light within the NIR window has the potential to provide the basis for a new intraoperative imaging technology for SLN localisation and the assessment of tumour margin delineation [18]. NIRFI approach has a higher spatial resolution than conventional radiological and nuclear medicine technologies, providing better discrimination between diseased and healthy tissues [203]. It has been reported clinically that NIRFI has a better detection ability compared to the current

gold standard ^{99m}Tc probe guided techniques for SLN detection. For instance, a prospective study comparing both methods was conducted on a group of 134 patients to resect axillary SLN in early breast cancer. This cohort presented a total of 246 SLN, detected by one or both techniques. The ^{99m}Tc method detected 231 SLN (93.9%), while the NIRFI detected 245 of 246 (99.6%) of the total SLN found during surgical procedures [157]. Several other studies have indicated that NIRFI for detecting SLN shows a sensitivity of 97-100% and was associated with low toxicity and few side effects, such as allergic reactions [204, 205, 206].

During the last decade, there have been an increasing number of NIRFI systems approved by the FDA for use in the operating theatre [17, 156]. These are not only for open surgery procedures, but also for laparoscopic, thoracoscopic, and robotic surgery. Examples of the currently available intraoperative systems are PDE® manufactured by Hamamatsu [207], the SPY fluorescence imaging system by Novadaq [208], the FLARE^{TM} system from the Frangioni Laboratory [209], and Fluobeam developed by Fluoptics [210]. The Artemis, a recent imaging system developed for real-time guidance during surgery, has been developed by Quest Medical Imaging (Essex UK) and the Leiden University Medical Centre in Holland [170]. This imaging system has been evaluated in vivo for tumours, SLN and vital structure visualisation, demonstrating the possibility of its use in the operating room, albeit with further improvements.

Other systems for in vivo molecular imaging are also commercially available, providing NIRFI and optical imaging for small animal studies. For example, the Pearl Impulse Small Animal Imager (LI-COR) combines two laser excitation systems in a closed box in which the sample is isolated from external sources of light [211]. This system is light-tight, offering high-quality NIRFI with very low background signal, and therefore has an exceptional imaging sensitivity imaging, even for deep targets.

Despite the fact that the NIRFI approach has emerged as a new intraoperative imaging technique, it has certain limitations with regards to the limited depth penetration of which it is capable, which is about 1-2 cm under the skin [17, 18, 156]. To overcome this impediment, gamma emitting and NIRFI agents have been combined for SLN navigation. This complementary combination allows the use of the penetrative nature of radioactivity to perform gross navigation of the lesion, while the superior spatial resolution of NIRFI assists surgeons in detailed target identification and resection [18]. This concurrent use of radio-

fluorescence imaging has the potential to reduce surgical time, anaesthesia, costs and improve cancer treatment outcomes.

In 2011, van der Poel et al. used the ICG-^{99m}Tc-nanocolloid to detect the location of SLN in 11 patients who underwent robot-assisted laparoscopic prostatectomy (RALP) [212]. SLNs were localised preoperatively using SPECT/CT imaging. Then, fluorescence imaging enabled intraoperative identification with improved surgical guidance, particularly for SLNs at sites with high radioactive background signals. Brouwer et al. also evaluated ICG-^{99m}Tc tracers to detect SLN in 11 patients with head and neck melanoma in 2012 [213]. This allowed preoperative visualisation and intraoperative guidance for SLN resection in head and neck cancer patients. Another study performed by van den Berg et al. in 2012 studied the concomitant application of ICG-^{99m}Tc for SLN mapping in oral cavity malignancies [214]. The combined use of radio-fluorescence imaging demonstrated the feasibility of SLN detection, in particular when found in close proximity to the primary site. Jeschke et al. (2012) investigated the use of a ^{99m}Tc-nanocolloid which was injected preoperatively with immediate injection of ICG before surgery for lymph node mapping in prostate patients [215]. Two separate systems were used in this study with a laparoscopic fluorescence imaging system designed to visualise lymphatic vessels and nodes. The second system was a laparoscopic gamma probe that could detect the radio localisation in SLN. This study showed that fluorescence navigation has the potential to be an effective tool not only for lymph nodes but also for lymphatic vessel visualisation. However, these findings were based on the sequential application of pre- and intraoperative gamma imaging/probing and real-time NIRFI due to the lack of any single system that combines gamma and NIRFI during surgery.

A recent study by Kang et al. in 2018 presented a proof-of-concept for a prototype multimodal laparoscope that enables NIR/gamma/visible imaging using a wavelength division multiplexing method [216]. They evaluated each imaging method and obtained simultaneous NIR/gamma/visible fused images of Eppendorf tubes containing a mixture of ICG and ^{99m}Tc that were placed within a dark box. A novel SFOV hand-held HGC has already been developed for scintigraphic procedures and intraoperative SLN mapping [176, 181]. This camera combines gamma and optical images to provide high spatial resolution and demonstrates a new possibility for SLN identification during surgery [218]. This chapter describes research undertaken to develop and integrate a new NIRFI system for combination with the HGC gamma imaging system. The eventual aim of this is

that the penetrative nature of gamma emission, together with the high spatial resolution of fluorescence imaging, can be combined simultaneously in a single device. This work has evaluated two NIRFI cameras using two different NIR florescent contrast agents at various concentrations and with different formats and phantoms, with the ultimate focus on detection ability in order to identify areas for future development.

4.2 Materials and methods

Different experimental configurations were used to study system performance under a range of simulated situations with variables including dye concentration, depth of target and target diameter. All images were acquired with the room lights turned off to reduce possible interference from visible light. A primary aim was to measure the signal-to-noise ratio (SNR), which indicates a system's ability to detect a particular feature in an image. The other quantity investigated was the contrast-to-noise ratio (CNR), which is a measure of how easily different regions can be distinguished from each other. Each of these quantities can be calculated using equations 4.1 and 4.2.

$$SNR = \frac{Mean}{\sigma_{Background}} \tag{4.1}$$

$$CNR = \frac{Mean - Mean_{Background}}{\sigma_{Background}} \tag{4.2}$$

4.2.1 NIRFI cameras

Two cameras were used in this experiment to detect the fluorescence agents: the USB2 uEye XS industrial camera, and the USB3 uEye UI-3240CP Rev.2 camera [219, 220]; these are described in more details in the following sections.

4.2.1.1 The XS camera

The USB 2 uEye XS optical camera consisted of a lens, autofocus system and a 5 megapixel CMOS sensor with a pixel size of 1.4 µm [219]. The sensor provided a resolution of 2592 × 1944 pixels with a frame rate of 15 fps. This lightweight camera, with a mass of 20 g, has dimensions of 26.5 mm × 23.0 mm × 21.5 mm. Camera readout was via a USB 2.0 interface and operation is controlled using Imaging Development Systems' (IDS) software suite to enable image acquisition. This optical camera has already been incorporated with the HGC system to obtain images in the visible wavelengths; it was not designed for NIRF imaging and therefore its infrared-blocking filter was removed for modification to act as a NIRF camera. Figure 4.1 shows the internal components of the XS camera.

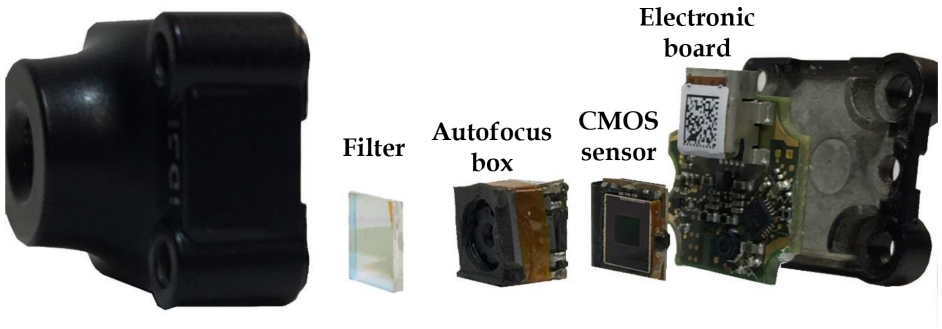

Figure 4.1: Components of the modified optical XS camera.

4.2.1.2 The CP camera

The UI-3240 CP, as shown in Figure 4.2, camera contained one of the most light-sensitive sensors in the IDS product portfolio, a 1.3 megapixel CMOS sensor with a 5.3 µm pixel size [220]. It had a resolution of 1280 × 1024 pixels at a frame rate of 60 fps. The dimensions of this camera were 29.0 mm × 29.0 mm × 29.0 mm with a weight of 52 g. This NIR camera was connected to a manual focussing lens that had a focal length of 6 mm. It was directly connected to a computer via USB 3.0 interface that ran using its own software program.

Figure 4.2: The CP NIR camera parts with the circular optical filter.

4.2.2 NIRFI probes

The most commonly used NIRF contrast agent in the 800-900 nm range is indocyanine green (ICG) [18, 158, 160]. It has been approved for several medical applications by the Food and Drug Administration (FDA) and the European Medicines Agency (EMA) [158]. When ICG is injected into the patient, it binds with serum albumin, the most abundant protein in blood, and emits light between 800 to 840 nm after excitation. ICG has been used for lymph node mapping in various types of tumour including breast cancer, melanoma, anal cancer, colorectal neoplasia, gynaecological cancers and head and neck lesions [18, 160]. More recently, an emerging NIRF dye with the product name IRDye® 800CW has been introduced for molecular imaging. It has an excitation peak at 770 nm and a light emission peak at 805 nm [18]. This new agent has been evaluated in animal models and is currently being used in phase II clinical trials, both in Europe and in the U.S. It has been reported that, in vivo, the IRDye® 800CW has lower toxicity than ICG and conjugates with biomolecules in a straightforward manner [159, 161]. Figure 4.3 shows the excitation and emission spectrum properties of ICG and IRDye® 800CW contrast agents.

Both cameras were evaluated using various concentrations of both ICG and IRDye® 800CW. ICG was dissolved in deionised water while IRDye® 800CW was dissolved in phosphate-buffered saline (PBS). Then, different concentrations were prepared in the range from 1 μM to 100 fM.

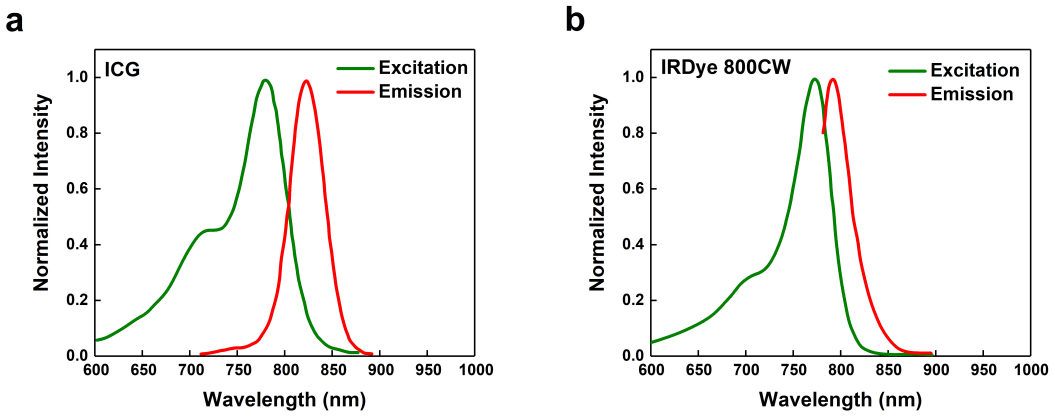

Figure 4.3: The excitation and emission spectra of (a) ICG and (b) IRDye® 800CW [17, 157].

For each concentration, a volume of 100 µL was added to a 96-well plate, and individual wells were imaged with each camera in different experimental setups. ImageJ software was used to measure the mean signal of the regions of interest (ROIs), whilst background signals were measured outside the ROIs [221]. The camera noise was considered to be the standard deviation within the background area ($\sigma_{Background}$). SNRs were calculated using equation 4.1, and the resultant curves were compared to the data published for the Pearl and Artemis devices [170].

4.2.3 Excitation light

A NIR LED ring with a peak intensity at 740 nm was used as the illumination source [222]. The full-width at half maximum (FWHM) of the spectral intensity is 30 nm, which makes this product suitably matched to the excitation wavelength of both fluorescence dyes. It has a ring geometry with a diameter of 70.8 mm. This provides a radiant flux of 80 W/m^2 with a spot size of 100 mm diameter when placed at a distance of 40 mm from the target surface.

4.2.4 Filters

NIR optical bandpass filters were used to select narrowband emission wavelength from the target with the aim of rejecting the excitation light and enhancing the detectability of the emitted light. Multi-layer hard-coating bandpass filters centred at 850 nm were fitted in each camera during the study [223]. For the XS

camera, a square filter with dimensions of 8 mm^2 and a thickness of 1.1 mm was fixed in front of the lens; a circular bandpass filter, with an 18 mm diameter and a 1.1 mm thickness and the same transmission properties, was placed between the manual lens and the sensor of the CP camera.

4.2.5 Phantoms

To evaluate the SLN mapping and target navigation capabilities of the imaging system, three phantoms were constructed in-house; two were made of polymethyl methacrylate (PMMA), also known as acrylic glass, to simulate lymph nodes. For the tissue-like phantom, a mixture of different components was used to build a phantom with optical properties similar to that of human tissues. These phantoms are described in more detail in the following sections.

4.2.5.1 Lymph node phantoms

The first phantom was a plastic slab with dimensions of 80 × 80 × 8 mm^3. It was designed with a 10 mm diameter well, 6 mm deep, positioned centrally. This phantom was used to simulate a large lesion (LL) in the body. The second phantom had a rectangular shape with dimensions of 26 mm × 14.5 mm and a thickness of 7 mm. It consisted of four columns, each having five different-sized holes with a fixed depth of 5 mm and diameters of 4, 3, 2, 1 and 0.5 mm. These different diameter sizes were used to simulate metastatic lesions (ML). Figure 4.4 is a schematic diagram illustrating each of these designs.

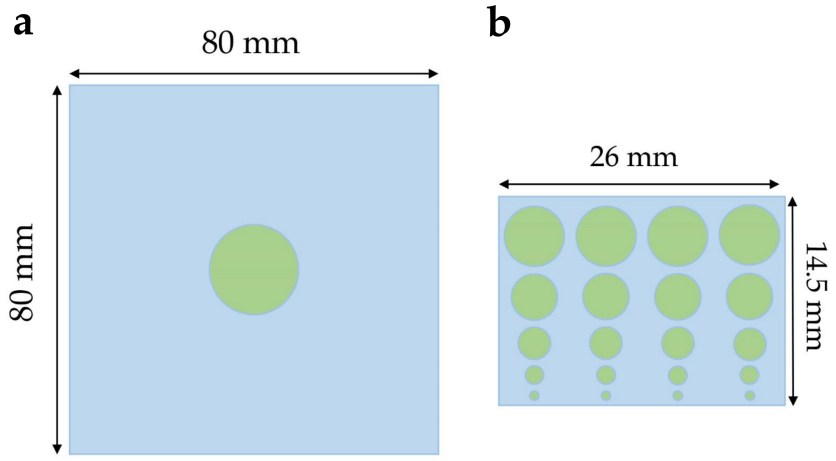

Figure 4.4: Illustration of the lymph node phantoms representing a large lesion (LL) in (a) and metastatic lesions (ML) in (b).

4.2.5.2 The optical tissue-like phantom

In order to characterise a target at depth within the body, a phantom with tissue-like optical properties was created based on a previously published study [194]. The phantom was made of a transparent silicone rubber in which scattering materials were mixed [224]. The scattering materials were Al_2O_3 and a cosmetic powder, which were used to imitate scattering substances under the human skin such as water, lipids, oxyhemoglobin, deoxyhemoglobin, melanin and fat [225, 226]. The phantom components were well-mixed in a glass beaker using a mixture of 97.52% silicone rubber, 2.22% Al_2O_3 and 0.26% cosmetic powder [227]. Then, the mixture was moulded in a standard Petri dish using different volumes to build phantoms with different centroid thicknesses of between 1 to 4 mm. The mixture was then kept for more than 48 hrs. at room temperature to ensure it was completely cured. After that, it was extracted from the Petri dishes with the final shapes shown in Figure 4.5.

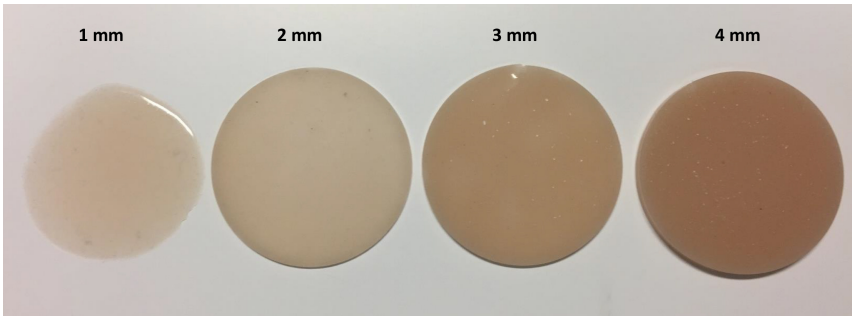

Figure 4.5: An image of the final constructed tissue phantoms with different thicknesses ranging from 1 to 4 mm.

4.2.6 NIRFI procedures

In this experiment, two identical setups were used for both the XS and CP cameras, where the excitation light was placed in two positions, namely above and to the side of the phantoms, as depicted in Figure 4.6. In the parallel position, each of the cameras was fixed in the middle of the excitation ring.

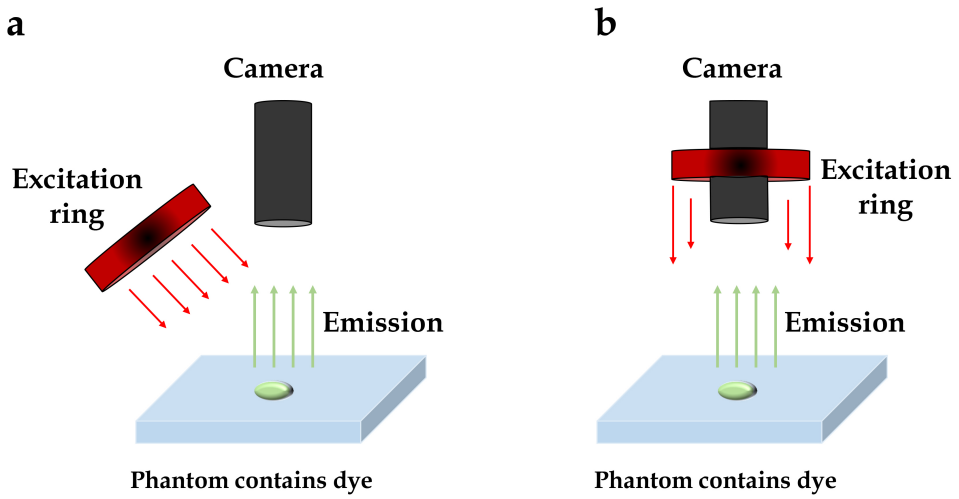

Figure 4.6: The experimental setup using the excitation ring to the side (a) and parallel to the imaging field (b).

4.3 Results and discussion

The performances of two NIRF cameras were assessed in the detection of ICG and 800CW dyes. These performances were put into perspective by comparison with the Pearl and Artemis NIRFI systems. Moreover, the detection capabilities of both imaging systems were determined for imaging metastatic targets with various concentrations at various distances and depths.

4.3.1 Concentration-based sensitivity analysis

Images of the 96-well plates were acquired for concentration series of both NIR fluorophores described above to estimate the concentration-dependent sensitivity of each camera. The resultant SNR curves were plotted as a function of concentration and compared to the Pearl and Artemis imaging systems from a study conducted by van Driel et al. in 2015 [170]. Similar to this study, the excitation light was placed parallel to the 96-well plate. For the ICG dye, Figure 4.7 (a) shows that the SNR of the Pearl increased with increasing concentration and peaked at a concentration of approximately 10 μM. After this peak, the SNR started to decrease due to peak quenching. The Artemis registered its lowest reliable concentration of 10^{-2} μM, and its SNR peaked earlier than the Pearl due to sensor saturation [170]. The CP and XS cameras were unable to

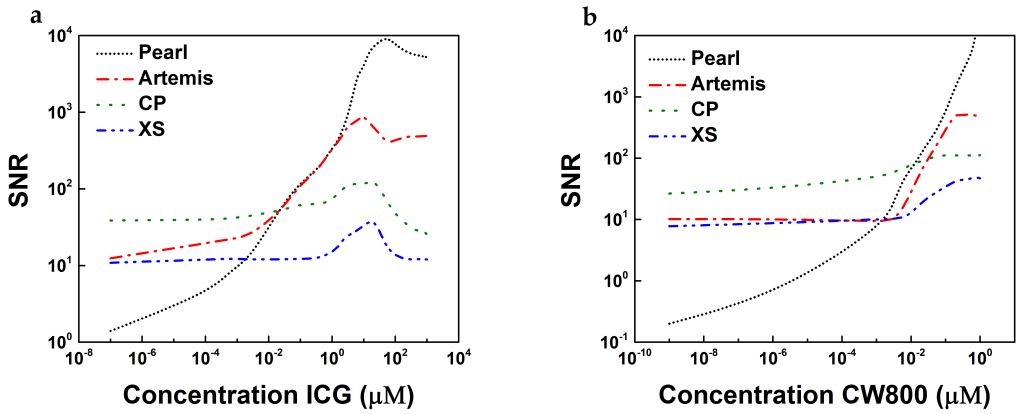

Figure 4.7: Signal-to-noise ratio (SNR) for series dilutions of ICG (a) and 800CW (b) imaged in 96-well plate for CP and XS cameras, as compared to the Pearl and Artemis.

distinguish lower concentrations due to high background noise from the bright reflection of the LED ring which was visible as a circular spot on the plastic well-plate. Also, it can be seen that the CP camera registered higher SNR at lower concentration compared to the other systems. Both the XS and CP were found to have a threshold for reliable ICG detection of 1 μM and reached maximum SNRs at concentrations of about 10 μM using the ICG.

Similarly, the 96-well plate was imaged for a serial dilution of 800CW dye and compared to the Pearl and Artemis, as illustrated in Figure 4.7 (b). The SNR curve for the Pearl began from almost zero followed by a considerable increase at a concentration of 10^{-3} μM, which then increased as the concentrations of 800CW increased, demonstrating its higher sensitivity for detecting very low concentrations [170]. The SNR started to increase for the CP, indicating its minimum detectable concentration at 10^{-3} μM, and then reached its peak earlier than all the cameras at about 10^{-3} μM. The lowest reliably detectable concentration for the XS was 10^{-2} μM, which recorded a maximum SNR at approximately 1 μM but at lower values compared to the other three cameras.

It is worth mentioning that the XS camera is designed to provide optical and coloured images, while the other three systems are specifically manufactured for NIRF applications. The minimum and maximum detectable concentrations were extrapolated for both dyes from SNR curves of the serial dilutions. Both cameras were able to detect ICG concentrations between about 0.8 to 80 μM, while the concentration ranges for 800CW began to be observed at 10^{-2} μM and plateaued at high concentrations up to 10 μM. The optimal concentration

of ICG (80 μM) was still comparable to the *in vivo* injected dose (100 μM) that has previously been used in Artemis-based studies. At low concentrations, the reflection of the excitation light had a negative influence on the sensitivity of both cameras. A diffuser plate was tested to eliminate the reflection of the LED ring on the sample, however this strongly decreased the intensity of the illumination and for this reason was not used further. The effect of the reflected excitation light on detection ability has been reported as a major challenge that limits the reduction of the noise floor when attempting to collect weaker fluorescence signals [170, 228, 229, 230].

4.3.2 CNR as a function of camera distance

Both cameras were used to image the ML phantom which contains different concentrations of ICG. Images were taken at distances of 5, 10, 15, 20, 25 cm between the camera and the phantom. Then, CNR was measured for one row with fixed diameter of 4 mm and different dye concentrations at both LED positions. Figure 4.8 depicts an example of images obtained by the CP camera for the ICG dye at different distances and both LED ring positions. The same procedure was followed for both cameras and both fluorescence dyes as well.

Figure 4.9 demonstrates CNRs of the XS and CP cameras at the angled and parallel positions. At each distance, the focusing lens of the CP camera needed to be adjusted manually for each acquisition. The XS camera did not require adjustment as it has an internal autofocus system. The highest intensity of ICG was measured at concentrations of 10 μM at all distances for both cameras positions.

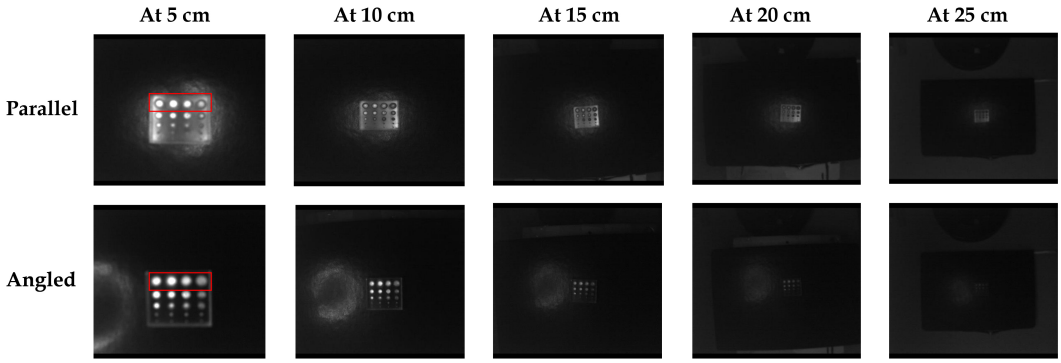

Figure 4.8: Example images of ML phantom filled with ICG using CP camera at different distances. The red rectangular indicates the row of 4 mm diameter wells that were used for CNR calculations.

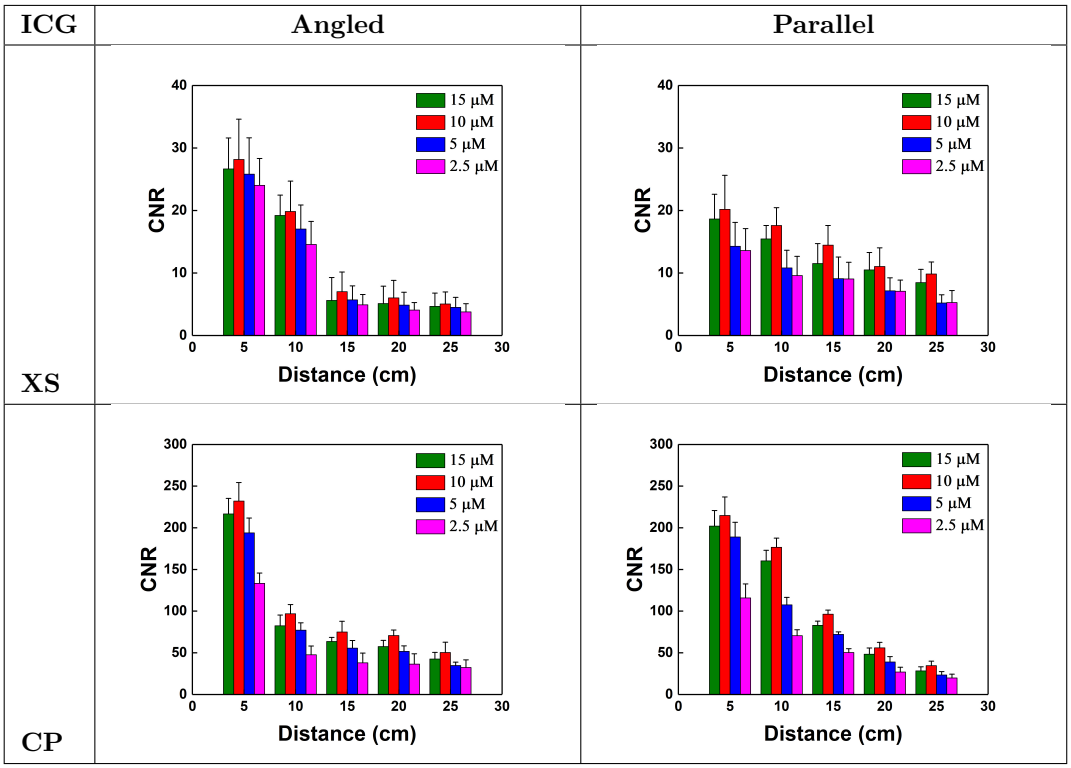

Figure 4.9: CNRs as a function of camera distance for the XS and CP with the ICG and 800CW. The angled position of the LED ring showed a better CNR in all setups.

Distances of 5 and 10 cm offered the best position for detecting different concentrations at both cameras and LED setups. The angled position slightly enhanced the ICG intensities for both cameras compared to the parallel position at same distances.

Using the 800CW dye, images also acquired for the ML phantom by both cameras and both LED ring positions. Figure 4.10 shows the CNR for both cameras at the angled and the parallel positions. It can be seen that the CNRs of 800CW at both LED positions for the XS camera are doubled their values using the ICG dye. This difference between the two dyes is also observed in the concentration-dependent sensitivity analysis for this camera. The CP camera, likewise the XS, is also measured higher CNRs using 800CW compared to the ICG probe. It reached the maximum intensity at 5 cm distance for concentration of 0.2 µM. However, this concentration (0.2 µM) has the highest 800CW intensity for both cameras at all distances. Again, a small improvement in CNRs was achieved when the LED ring was placed in the angled position for both cameras due to the absence of the frontal LED reflection on the ML phantom.

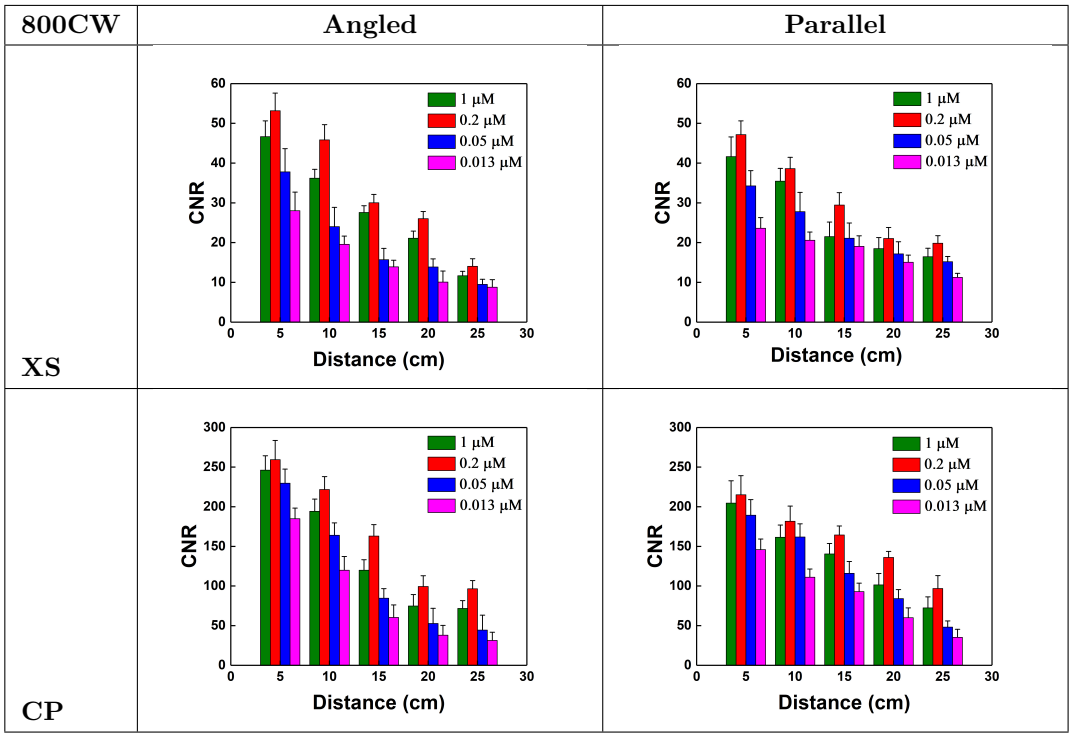

Figure 4.10: CNRs as a function of camera distance for the XS and CP with the ICG and 800CW. The angled position of the LED ring showed a better CNR in all setups.

4.3.3 CNR as a function of target diameter

The ML phantom was used to investigate the detection ability of each camera for imaging simulated small-sized metastatic lesions with focal spots between 4 and 0.5 mm in diameter. At 10 cm distance, one column containing optimal concentrations resulting from a dilution series in concentration-based sensitivity analysis was chosen for each dye. Chosen concentrations were 10 and 1 µM for ICG and 800CW, respectively. Figure 4.11 shows images that were obtained for the ML phantom using the CP and XS with both dyes.

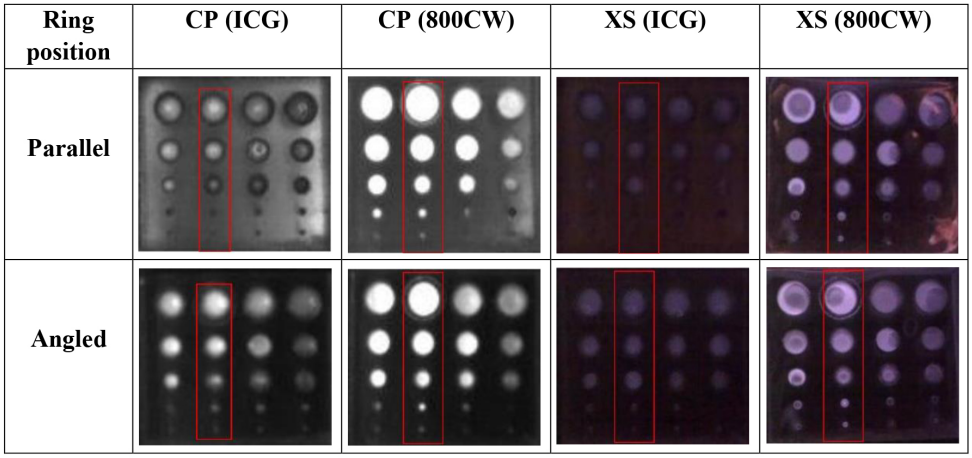

Figure 4.11: Example images of the ML phantom filled with different concentrations of ICG and 800CW using CP and XS cameras at 5 cm distance using different light source positions. The red rectangle indicates the column of different diameter wells filled with concentrations of 10 and 0.2 μM of ICG and 800CW dyes, respectively. The effect of the reflection on the imaged field can be seen in both LED positions. Air bubbles are shown within the well for 800CW using the XS camera.

As can be seen in Figure 4.12, the CNR of the XS, using ICG and 800CW probes with angled and parallel positions of the LED ring, are plotted for all holes for one column. When the excitation ring was in the angled position, higher CNR values were observed, such that smaller wells (0.5, 1 mm) could be identified with a lower surrounding background signal. However, when the parallel position was used, the smaller wells could not be distinguished from the background. This was due to the fact that the photons exciting the fluorescence dyes followed a similar and contorted path as the light emitted towards the detector [18, 232]. Thus, the high amount of scattering from the excitation light at the surface of the ML phantom produced stronger light signals than the small-sized targets. This accumulation of consecutive scattering events led to random changes in the emitted photon paths and consequently prevented the accurate localisation of small-sized sources.

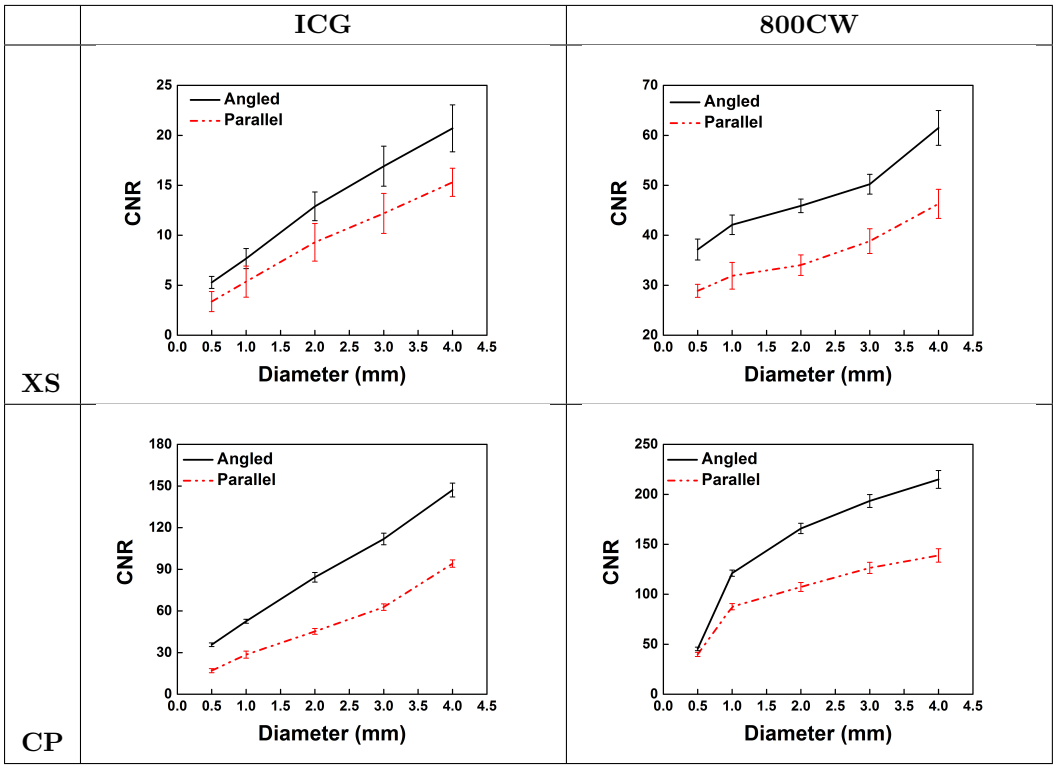

Figure 4.12: CNRs as a function of well diameter for the XS and CP with the ICG and 800CW. The angled position of the LED ring showed a better CNR in all setups.

4.3.4 CNR as a function of target depth

One of the main limitations of the NIRFI technique is the limited penetrative ability due to absorption and scattering within tissues. Scattering events (i.e., changes in photon direction) occur much more frequently than absorption events [232]. Thus, to evaluate the performance of each camera, measurements using the optical tissue-like phantom were conducted. Figure 4.13 shows example images of the ML phantom filled with 800CW and imaged under different layers of the tissue-like phantom at a fixed distance (5 cm).

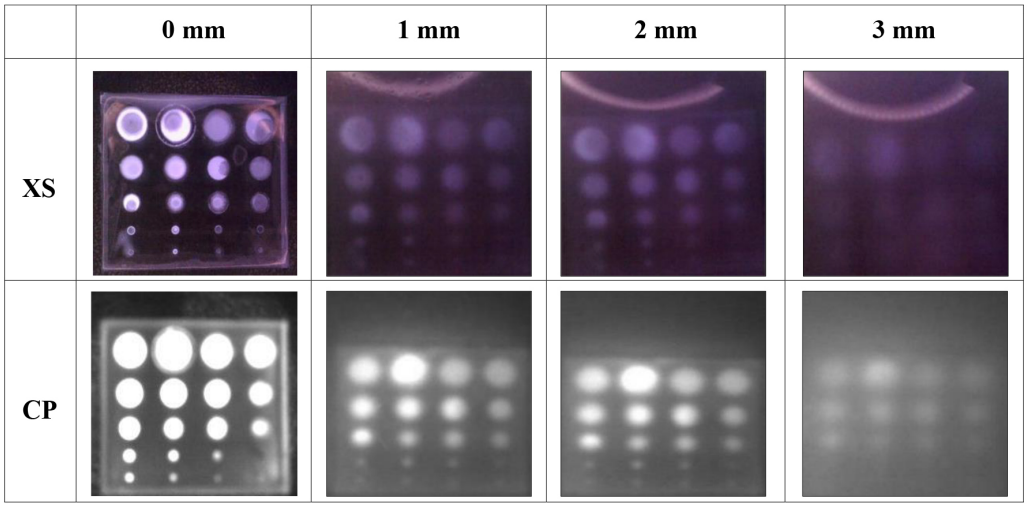

Figure 4.13: Example of the ML phantom filled with different concentrations of 800CW and covered with the optical tissue-like phantom with thicknesses between 0 and 3 mm. Images were obtained using the XS and CP cameras at 5 cm distance. The LED was in the angled position.

Images were also taken with the LL phantom using optimal intensity concentrations of 10 µM and 1 µM for ICG and 800CW, respectively. An example of the images acquired is shown in Figures 4.14 and 4.15 for the LL phantom filled with 800CW and placed at 5 cm distance. It was imaged with the CP camera under thicknesses between 1 to 8 mm of scattering equivalent medium and the LED ring was placed in the parallel and angled positions. It was observed that the spatial resolution degraded at 5 mm and the fluorescence target disappeared completely at an 8 mm depth due to the increased scattering and absorption effects of the optical tissue-like phantom.

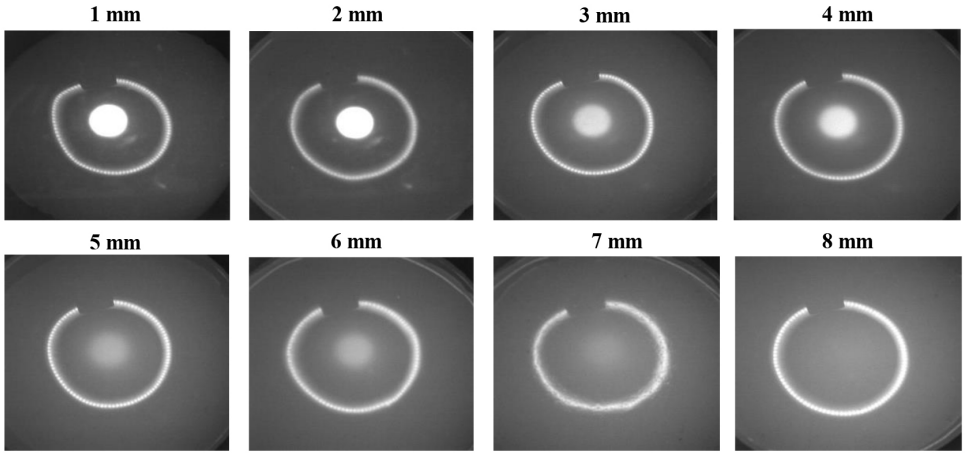

Figure 4.14: Images of the LL phantom containing a concentration of 0.2 μM 800CW and imaged by the CP camera. The tissue-like phantom was used with a 1 mm thickness increment. The circular ring around the fluorescence target is the reflection of the LED ring placed in the parallel positions.

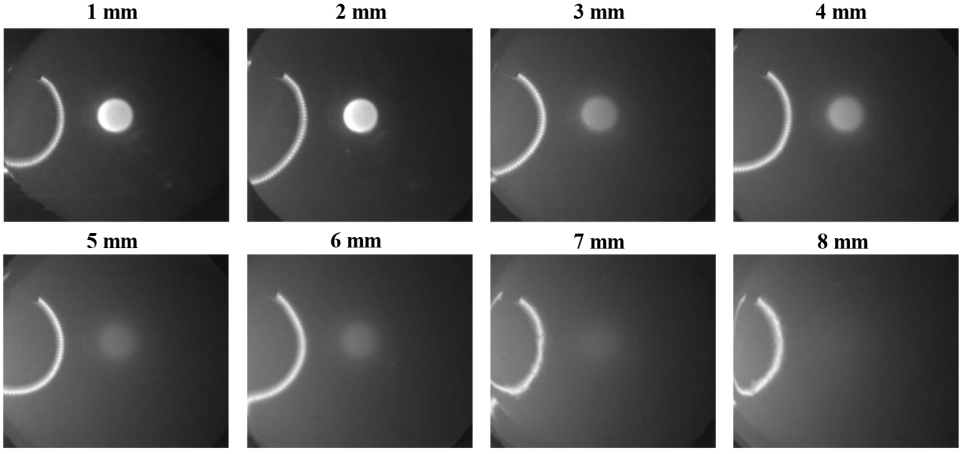

Figure 4.15: CP camera images of the LL phantom containing a concentration of 0.2 μM 800CW. The reflection of the circular LED ring is shown in the angular position aside from the fluorescence target.

Figure 4.16 illustrates CNRs for the XS and CP cameras as a function of depth using both fluorescence dyes. CNRs decreased as depth increased, until the point where the circular shape of the fluorescence target disappeared completely at 6 and 7 mm for the XS and CP, respectively.

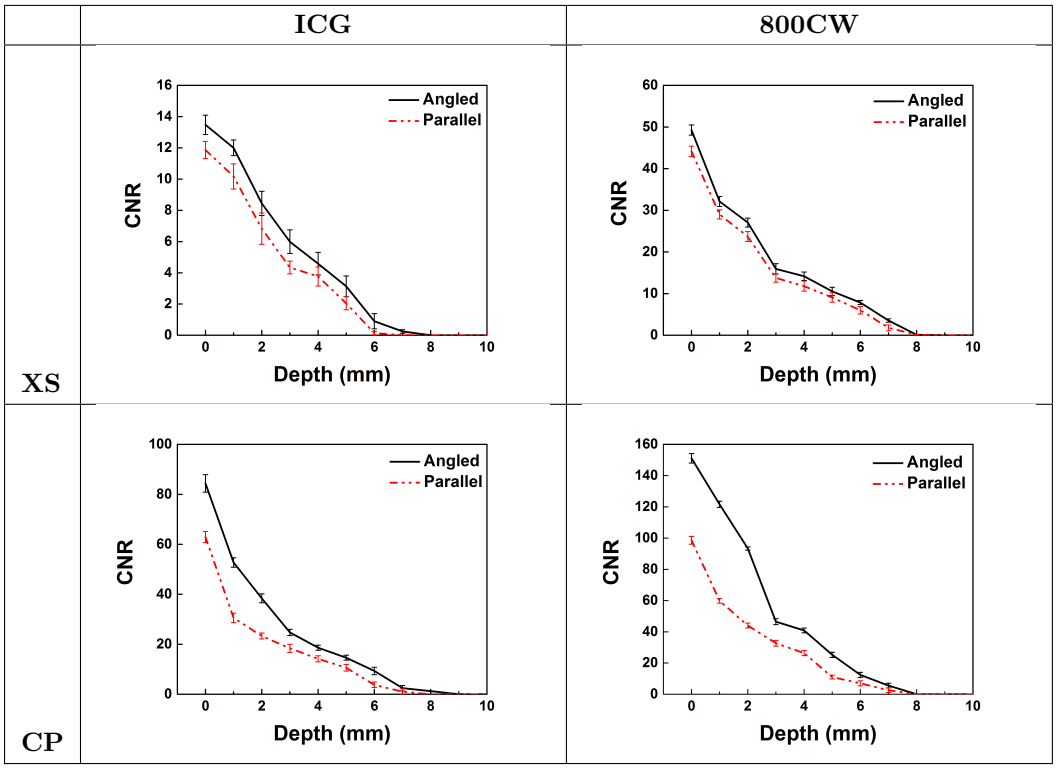

Figure 4.16: CNRs as a function of thickness for the XS and CP with ICG and 800CW using the LL phantom. The angled position shows better CNRs for all cameras when using either dye. For all setups, the maximum depth that either camera could image was 7 mm.

Both tested cameras were capable of detecting both dyes, ICG and 800CW, as deep as 7 mm. The angled position of the excitation light also enhanced the intensity for both cameras and for both dyes. A depth of 7 mm was found to be the maximum detection depth, after which it became difficult to identify NIRF targets even with diameters as large as 10 mm using either camera or either dye in either LED ring position. For targets with smaller diameters (between 0.5-4 mm) the maximum depth for fluorescence imaging was about 3 mm due to the weak signal emitted from the micro-volumes used. In general, the CP camera showed better detection abilities than the XS camera in all tests when using different dyes and LED positions. Unlike the CP, the XS camera is mainly designed for optical applications, but with appropriate modification it was able to detect NIRF targets without the need for manual adjustment of the focussing lens at each acquisition. Clearly, detection ability depends on different factors including illumination position, filtration of the excitation and emission lights, fluorophore concentration, target size and position, phantom properties and the camera system.

One possible enhancement could be focussing the excitation light to produce homogenous illumination of the target. This may allow for a reduction in the reflected light from the area of non-interest around the target by adjusting the illumination to only cover to the area being imaged. Another important improvement could be to filter the excitation light using an interference filter to block unwanted spectral ranges. Thus, further improvements are required for the NIRFI system, taking into account cost-effectiveness, camera size, simplicity, LED intensity and position. Further development will allow the NIRFI system to be combined with the HGC camera to enable dual radio-NIRFI. This would offer the possibility of simultaneously using the higher penetrative ability of gamma-ray sources with the higher spatial resolution of NIRF in a single imaging system for intraoperative procedures.

4.4 Conclusion

Fluorescence-guided surgery has the potential to assist surgeons with anatomical and functional feedback about tumour margins and vital structures. However, the main inadequacy of the NIRFI technique is its limited penetrative ability for targets located deeper than 1 cm. To tackle this limitation, a combination of radioactivity and NIRFI techniques have been used for SLN identification. These techniques were conducted using separate systems due to the current lack of a single real-time imaging system that combines gamma radiation with NIRF.

A hybrid gamma camera that combines gamma and optical imaging has been developed for clinical and surgical use. Further development of this system will merge the NIRF modality to provide simultaneous fluorescence-gamma imaging. In this study, NIRFI systems were assessed by testing two cameras (XS and CP), two fluorescence dyes (ICG and 800CW) and different phantoms with different LED excitation positions. The minimum and maximum detectable concentrations of ICG and 800CW were determined. Moreover, the detection capabilities of both imaging systems were determined for the purpose of imaging metastatic targets. A tissue-like phantom was also used in this evaluation to determine the maximum depth at which NIRF targets could be distinguished. Further development will combine the NIRFI system with the HGC camera to enable dual radio-NIRFI.

Chapter 5

Characterisation of SiPM for an intraoperative gamma camera

5.1 Introduction

Intraoperative gamma imaging techniques play an integral role in identifying affected tissues, SLN mapping and radical cancer resection. This modality provides comparable intrinsic spatial resolution to conventional nuclear medicine devices, small size, compact design, simple use and real-time quantification with displayed images [116, 117]. There are different gamma detection systems that have been used for cancer surgery as described previously in section 3.2.2 Chapter 3. Among these systems are scintillators EMCCD-based technologies that have been used for cancer treatment and preclinical studies. EMCCDs feature low readout noise, high quantum efficiency (93% at 550 nm for back-illuminated), detection of low light level, high spatial resolution and wide dynamic range [233]. However, there are some limitations of EMCCD technology such as noise which could sometimes complicate event detection in low energy gamma imaging [233, 234]. A cooling system (typically between -10 and -50 $^{\circ}C$) is also required to suppress thermal dark counts that could be a more challenging task when designing an array of detectors. Furthermore, the mechanism in which EMCCD collects charges, more details were given in section 2.3.2 Chapter 2, leads to slow readout that could limit its use for high count rate applications [40, 234, 235, 236, 237].

SiPM technology has become increasingly popular compared to PMTs and other types of photodetectors in medical gamma imaging. SiPM has a good time resolution, high gain, low power consumption, insensitivity to magnetic fields, robustness, easy installation, good energy resolution and small design [238, 239]. SiPM can produce charge pulses of 10^5-10^7 in several tens nanosecond compared to a gain of 10^3 generated by EMCCD. The EMCCD has slow readout property where capture of photon arrival time is not possible, hence, it can not be used for time coincidence measurement as required in PET imaging [240, 241]. Despite the SiPM's high dark count rate and variation of gain with temperature, different studies have reported that SiPM can operate at room temperature when a gain stabilisation system is used [242, 243, 244, 245].

Various novel approaches have been carried out to use SiPM in medical X-ray scanners, SPECT and PET systems [240, 246, 247, 248, 249, 250, 251]. For intraoperative imaging and preclinical studies, different prototypes have been developed exploiting the advantageous features of SiPM-based detectors [252, 253]. For example, the first generation of Albira, a small animal PET/SPECT/CT imaging device uses monolithic crystal coupled to PMTs, showed high image quality and good performance [254]. The next generation of Albira device was designed based on arrays of SiPM in replacement of the PMTs. They demonstrated that the SiPM-based device significantly outperforms the previous PMTs based system in all measured performance parameters [255].

Another study by Castro et al. characterised SiPM-based SFOV gamma camera for scintimammography, SLN detection, small animal imaging and research applications [256]. In their prototype, they investigated the use of SiPM for detecting light from a CsI[Na] crystal. Their study suggested that SiPM has a good performance with obtained energy resolution of 23% at 122 keV. However, they proposed that further optimisations are needed in terms of improving readout electronics, temperature stabilisation and bias voltage monitoring of the SiPM. Another study by David et al. investigated SiPM array coupled to LGSO[Ce] scintillator crystal for SFOV PET imaging [257]. Their findings showed a clear visualisation of discrete events on the scintillator with an energy resolution of 18% at ^{137}Cs energy (662 keV).

The SFOV HGC, that has been already described in Chapter 3, was designed for scintigraphy imaging and intraoperative SLN mapping. The HGC uses EMCCD technology showing good performance characteristics for clinical gamma

imaging in the energy range between 30-140 keV [184]. A SiPM-based imaging system could have the potential to enhance the HGC performance at higher energy ranges which could then extend its application in other fields that include high energy gamma imaging. In order to design a detector system based on SiPM principle, it is essential to investigate SiPM physical properties. The purpose of this Chapter is to study the main SiPM properties such as breakdown voltage, gain, diode capacitance, quenching resistor, time response, crosstalk probability and count rate levels in relation to temperature. Measurements of these quantitative data is of paramount importance to properly identify and define the essential signal characteristics of SiPM which allow us to gain further insight into the device physics.

5.2 Materials and methods

The SiPM is a semiconductor photodetector which uses a matrix of elementary cells operating in Geiger mode. Each cell is connected to a series resistor which limits the current flowing during the breakdown and consequently ensures that the avalanche current is quenched. The basic functionality of SiPM was reviewed in section 2.3.6 Chapter 2. The presented study was conducted using SiPM manufactured by Hamamatsu with the physical properties that are shown in Table 5.1. Tested SiPM has 3×3 mm^2 effective photosensitive area with a microcell size of 50 μm. This SiPM series has a spectral response ranging between 270 to 900 nm with a peak sensitivity at a wavelength of 450 nm.

Serial No.	Effective area	Pixel pitch	No. of pixels	Spectral response
3050CS	3×3 mm^2	50 μm	3600	270-900 nm

Table 5.1: Physical properties of the SiPM [258].

Figure 5.1 shows the SiPM S13360 series which was connected to a printed circuit board (PCB) with 1 kΩ bias resistor and a coupling capacitor to act as a low pass filter for the input signal. A microscopic image was obtained showing the photosensitive area and the quenching resistor for each pixel.

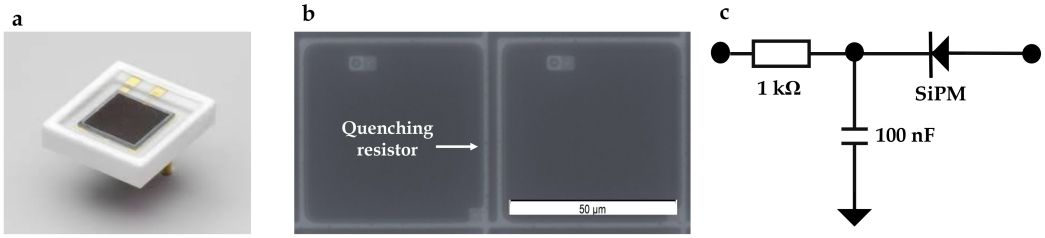

Figure 5.1: Illustration photo of the SiPM (a), (b) microscopic image of the SiPM shows pixels and quenching resistors and (c) a diagram of the PCB attached to the SiPM to filter the input signal [258].

Figure 5.2 demonstrates the characterisation setup which was mainly designed to test and enhance electrical characterisation methods of SiPM [259]. The SiPM system was connected to a thermo-electric cooler (TEC) board, provided by Meerstetter Engineering Gmbh, to maintain the SiPM at a stable set temperature [260]. Then, it was placed in an inner chamber in order to avoid condensation using dry nitrogen to reduce the humidity in the range between 3-5%. In a light-tight box the SiPM was illuminated by a pulsed laser (LPG-450), from Photek, that provides photon pulses with wavelength of 405 nm [261]. The pulse duration of the light source was 100 ns with a frequency of 1 kHz driven by a pulse generator. The light beam was directed to pass through a natural density (ND) filter, provided by Thorlabs, to reduce the number of photons hitting the SiPM to a low level [262]. Prior to each test the inner chamber was evacuated and the SiPM's output signal was integrated using 12-bit high resolution oscilloscope from Lecroy [263].

It is important to mention that for performing this measurement, it is necessary to obtain statistically significant set of data for the output pulse in order to describe meaningful histograms. For this reason, the sequence acquisition mode in the HD oscilloscope was used to maintain high sample rate. Therefore, a trace of 10 ms contains 2.5×10^7 samples at 400 picosecond/sample. This TRaCe (TRC) file was then converted into a text file using a python code for data analysis and parameter calculations.

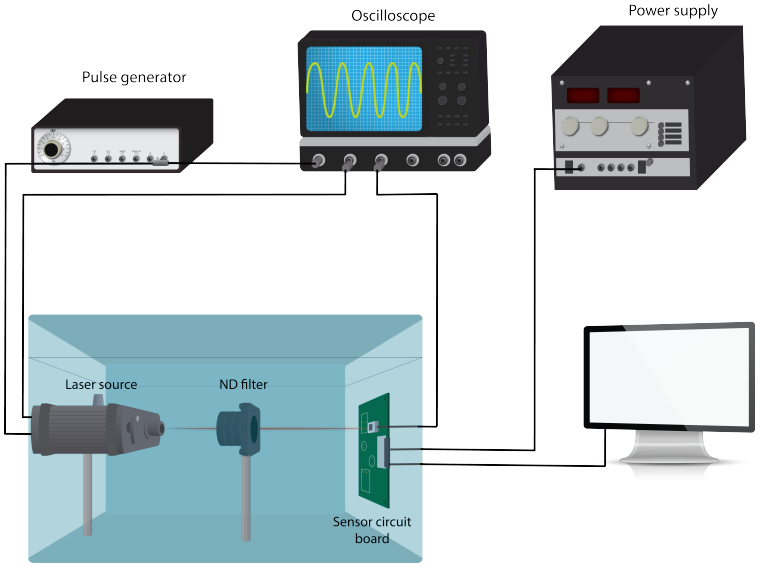

Figure 5.2: Illustration of the characterisation setup of the SiPM. The laser pulses are driven by a pulse generator where the pulse signal is fed into the oscilloscope. Laser beam passes through the ND filter hitting the SiPM that is mounted on the circuit board. The SiPM was operated by a power supply. The resulted signal was recorded by the oscilloscope.

5.3 Results and discussion

In this experimental test, the main properties of SiPM (type S13360-3050CS by Hamamatsu) were addressed including measurements of the breakdown voltage, gain, junction capacitance, time response, quenching resistance, dark count rate and crosstalk probability at different temperatures.

5.3.1 Determination of the breakdown voltage

Measurement of the breakdown voltage (V_{BR}) is important before determining other characteristics of the SiPM. Scattering of charge carriers in the silicon leads to net loss of carriers' energy prevents the impact ionisation rate [265]. Therefore, it is required to increase the impact ionisation rate by increasing the electric field strength (i.e the reverse bias) which in turn increases V_{BR}. The proportional relation between the signal amplitude and the applied voltage at different temperatures was plotted and V_{BR} was then derived from the y-intercept of a linear curve fitted through the points as shown in Figure 5.3. The linear dependence of V_{BR} on temperature was measured.

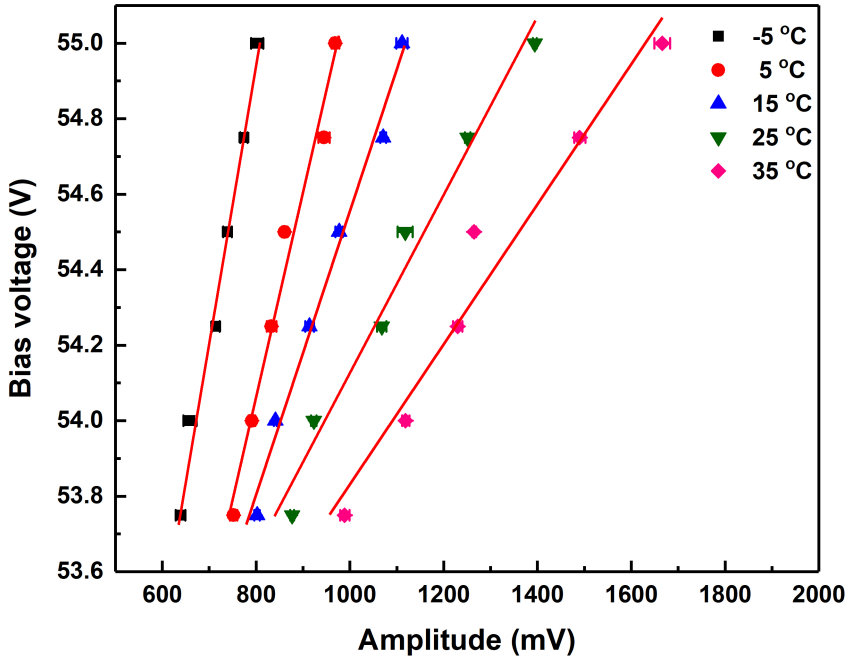

Figure 5.3: The relation between the amplitude and the bias voltage was used to calculate the breakdown voltage at different temperatures. Some error bars are smaller than the data point symbols.

The breakdown voltage was then determined for this SiPM sample at five temperature values. Figure 5.4 shows a linear dependence with nearly identical slope between the V_{BR} and temperature. The influence of temperature on V_{BR} is due to the increased probability of scattering for the charge carriers (electrons and holes) as temperature increases. Measured V_{BR} was in the range between 49 to 52.8 V with a temperature coefficient of 0.10±0.04 $mV/^{\circ}C$. The standard error was calculated from the intercepts of the linear regression fitting for each point at each temperature. These values were used as the basis for all applied voltages at each tested temperature in the following parameters measurements.

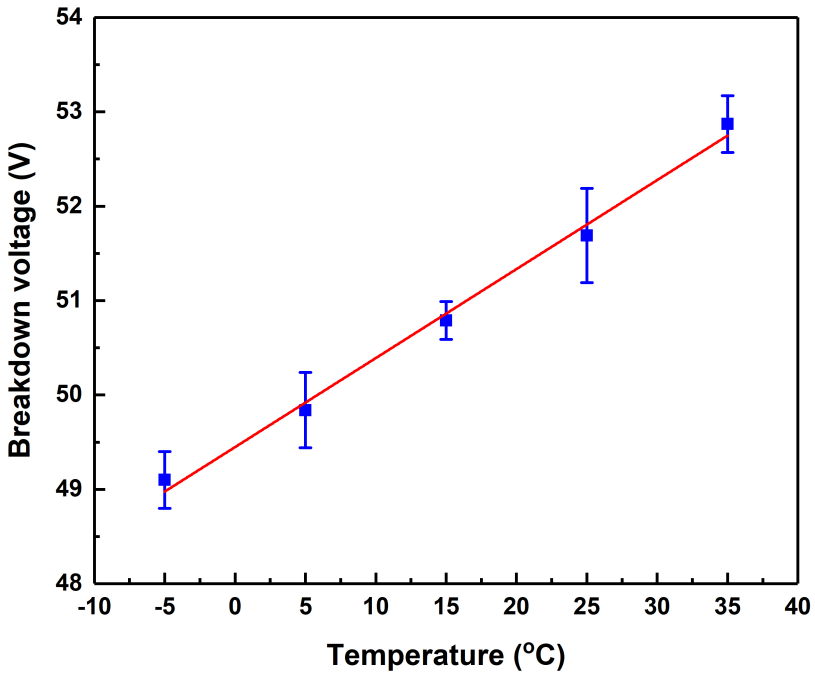

Figure 5.4: The relation between the measured break down voltage as a function of temperature with an R^2 value of 0.993. Error bars are the standard errors from the linear regression fitting for each point.

5.3.2 Gain measurement

Using the oscilloscope, the charge-voltage measurement was conducted by illuminating the SiPM with low photon flux at different reverse bias voltages and different temperatures. Figure 5.5 shows a snapshot of the acquired waveform using the oscilloscope in the persistence mode.

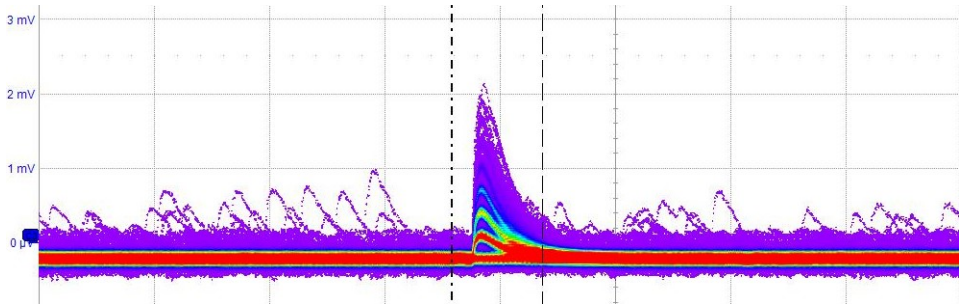

Figure 5.5: Acquired waveform of the SiPM illuminated by the laser source. Different peaks are shown that were corresponding to different discharging levels.

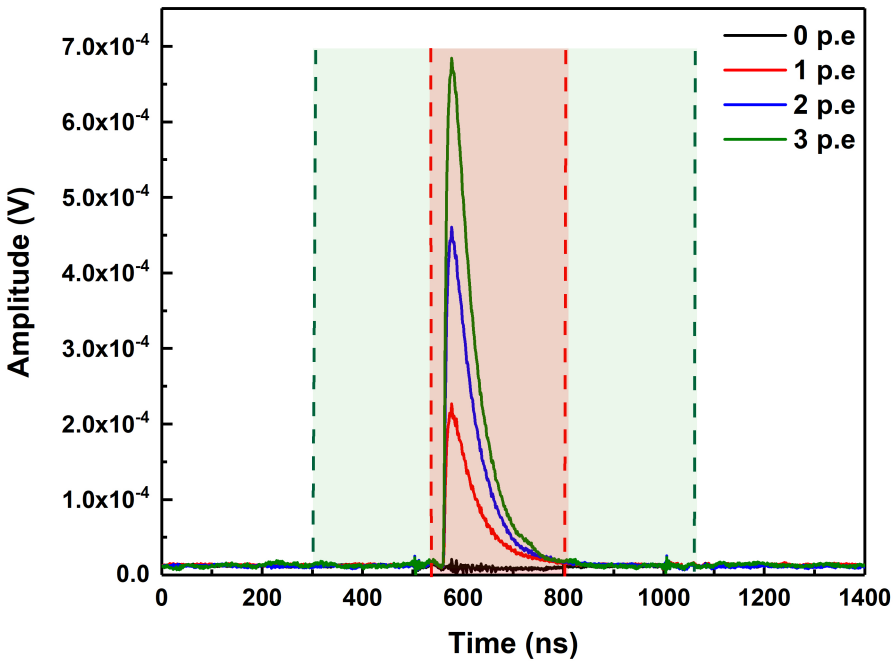

Figure 5.6: Example of the output waveform of the SiPM when illuminated by the laser source that operated at 2V overvoltage and 25 $^{\circ}C$. The different peaks visible correspond to the numbers of photons (one, two, etc.) detected per pulse. Due to the large gain, signal separation between different number of pixel discharging is clearly visible.

Figure 5.6 illustrates an example of the resulting signal amplitudes as a function of time showing the number of pixels that encountered a breakdown with different amplitudes as a result of photons detected from the laser source at 25 °C. The flat line, 0 photoelectron peak (0 p.e), corresponds to the noise pedestal where there was no pixel discharging i.e. the readout noise of the setup and electronics. The first smallest pulse (1 p.e) equates a fired microcell to a single photon detection, the second for two microcells discharging and so on. This waveform also provides a method to estimate a single pulse shape of the SiPM under evaluation.

For each acquired waveform an integration gate was chosen manually so that the entire SiPM signal was contained inside (shaded green area) while a peak gate was used to identify the location of the signal peak only (shaded red area) in Figure 5.6. Following this, integration with peak gate limits were used to extract peak height distribution (PHD) as illustrated in Figure 5.7. This pulse

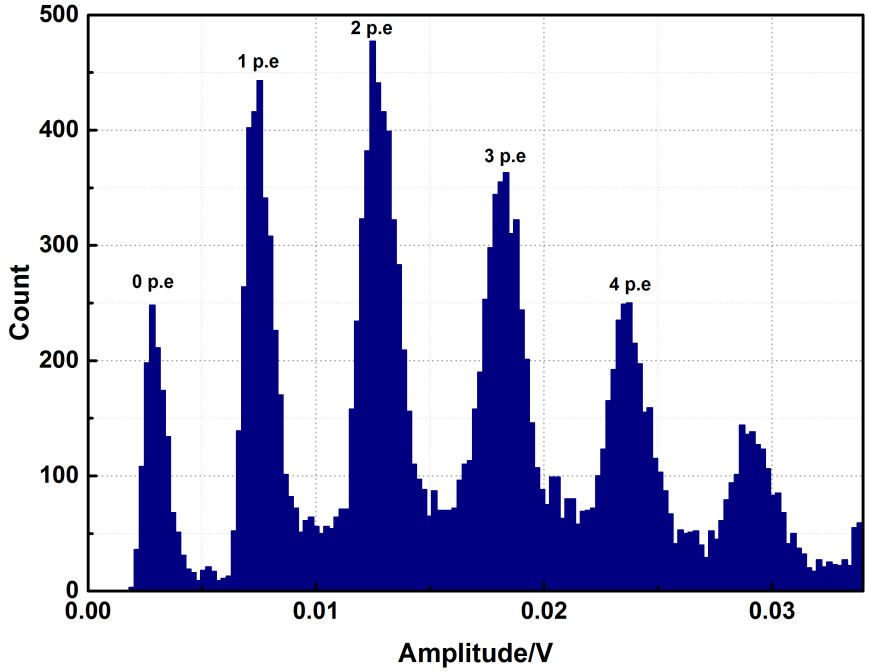

Figure 5.7: An example of pulse height spectrum acquired by illuminating the SiPM with a laser source. This spectrum was obtained at 3V overvoltage and 25 $^{\circ}C$.

height spectrum shows that each microcell in the SiPM is capable of detecting photons independently and can provide information on the magnitude of the instantaneous photon flux. It can be seen that there is a good separation between discrete p.e peaks and a valley exists between the pedestal and 1 p.e. The properties of these peaks can be used to determine the net output charge under the area of the 1 p.e which equals the gain, by definition, of the evaluated SiPM. The next step was to extract the 1 p.e single pulse shape as depicted in Figure 5.8 in order to measure the required parameters. An integration window for the whole peak was determined manually, as described previously, to measure the area (green region in the graph) that represents the collected charge. The resulted gain by unit time was then measured at different overvoltages and temperatures. The gain was measured using the relation between the amplitude (V) and total collected charge (Q) at determined time window (t) divided by the input resistance (R) of the oscilloscope, i.e. 50 Ω, as shown in equation 5.1 [274].

$$Q = \frac{V}{R} \times t \tag{5.1}$$

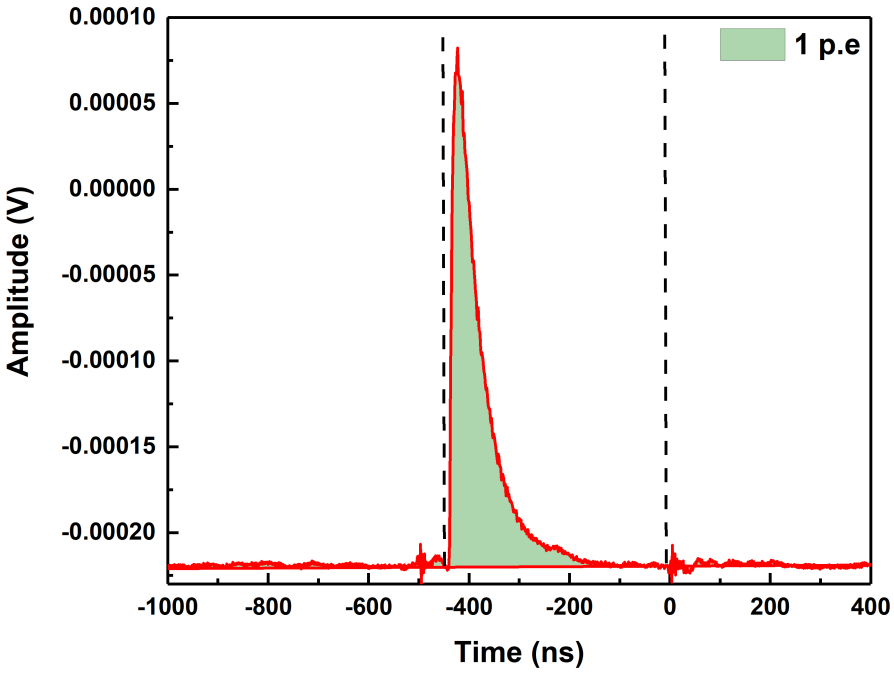

Figure 5.8: The single pulse plot of the 1 p.e at 3V overvoltage and 25 $^{\circ}$C. The green region represents the chosen area.

Three overvoltage values were applied to the SiPM at different temperatures obtaining different waveforms for measuring the gain as a function of overvoltage. Figure 5.9 represents the linear relation between the measured gain of 1 p.e with varying overvoltage at different temperatures. Errors in gain measurements were calculated by varying the integration window (black dashed lines in Figure 5.8) of the area in the single pulse plot for each point.

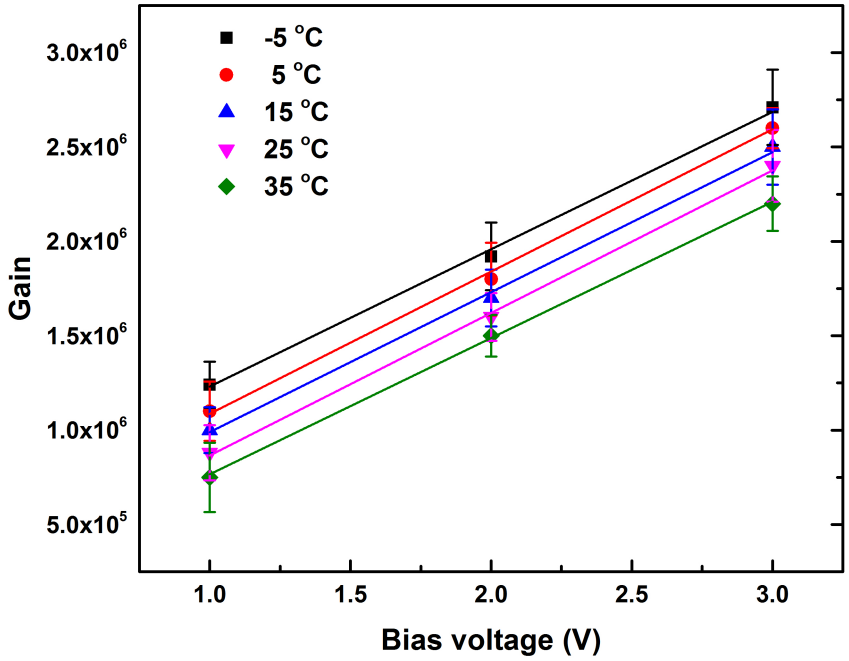

Figure 5.9: Measured gain as a function of the reverse bias at different temperatures. A linear relation between the gain and the overvoltage is obtained with averaged R^2 value of 0.996.

The demonstrated gain properties exhibited the SiPM behaviour as a function of different overvoltages and temperatures. For the tested SiPM type, the measured gain was in the range between 7×10^5 to 2×10^6 depending on the operating overvoltage with varying temperatures. The linear dependence of the gain as a function of the overvoltage is due to the increase of the internal electric field that initiates more avalanches. This leads to more charge stored on the junction at higher overvoltage. These typical high values of gain represents one of the advantageous features of SiPM compared to PMTs which has a similar gain.

The same resultant gain value is also demonstrated as function of the temperature as shown in Figure 5.10. It is demonstrated that SiPM gain decreased as temperature increased by indirect relation. This is due to the increase of V_{BR} as temperature increases, hence, at a fixed overvoltage value, increasing of temperature hampers the impact ionisation rate and consequently reduces the gain.

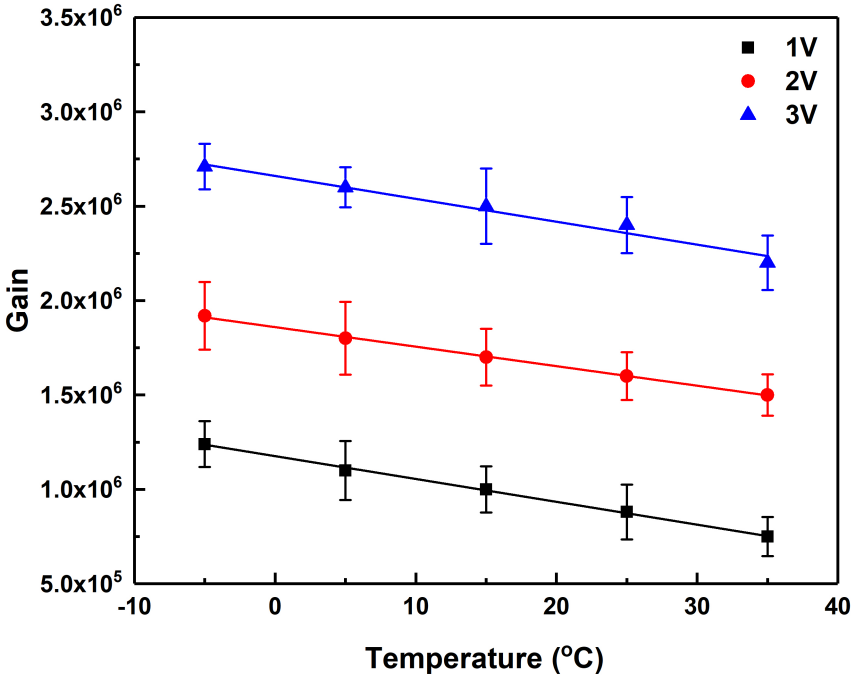

Figure 5.10: The relationship between the gain and temperature at different bias voltages. The gain decreases as temperature increases with a mean coefficient of $-11.5 \pm 5 \times 10^3$ electron/$^{\circ}C$ with varying overvoltages.

Gain variation in SiPM is an undesirable process that may lead to a significant shift in the detected peak pulses which limits energy resolution and result in serious artefacts in reconstructed images [266, 267, 268]. Thus, it is important to stabilise the gain under varying ambient temperature which is a common requirement in SiPM applications. However, in medical use, room temperature can be maintained at low levels and the gain can be stabilised using a built-in temperature compensation driver circuit that senses the SiPM temperature and feeds this information back to compensate with the appropriate operating voltage. This provides a good gain stabilisation of about less than 2% at a temperature of 60 $^{\circ}C$ [269, 270].

5.3.3 Junction capacitance

The junction capacitance C_j is an important parameter in SiPM. To measure this, the collected charge has an impact on the recovery time that needed to complete the recharge phase. The collected charge was extracted from the area

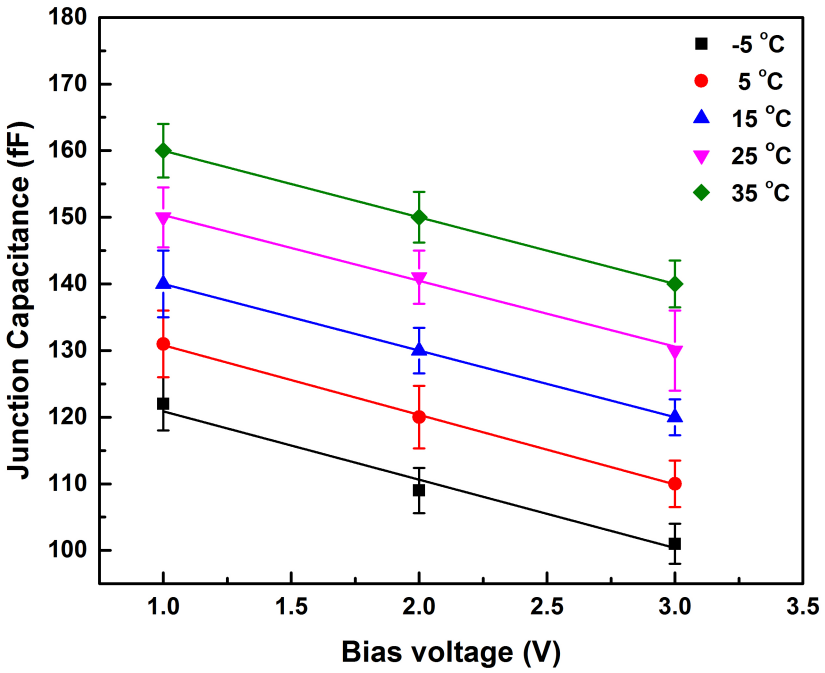

Figure 5.11: A plot shows the junction capacitance measurements as a function of different overvoltages and temperatures.

under 1 p.e curve for each overvoltage $\triangle V$ and temperature. $\triangle V$ is the difference between the applied reverse bias voltage and the breakdown voltage. The C_j was measured using charge collection in a capacitor as in equation 5.2 [67].

$$Q = C_j.\triangle V \tag{5.2}$$

Measured C_j as a function of the increased overvoltage is demonstrated in Figure 5.11. It shows a linear decrease of C_j as the overvoltage increases at different temperatures with a mean voltage coefficient of $-10.1 \pm 0.2 fF/V$. By increasing the reverse bias voltage, the width of the depletion region increases and consequently the junction capacitance decreases [271].

5.3.4 Time response

The time properties of SiPM are of great importance for different applications such as TOF measurements and investigating fast known and unknown scintillation

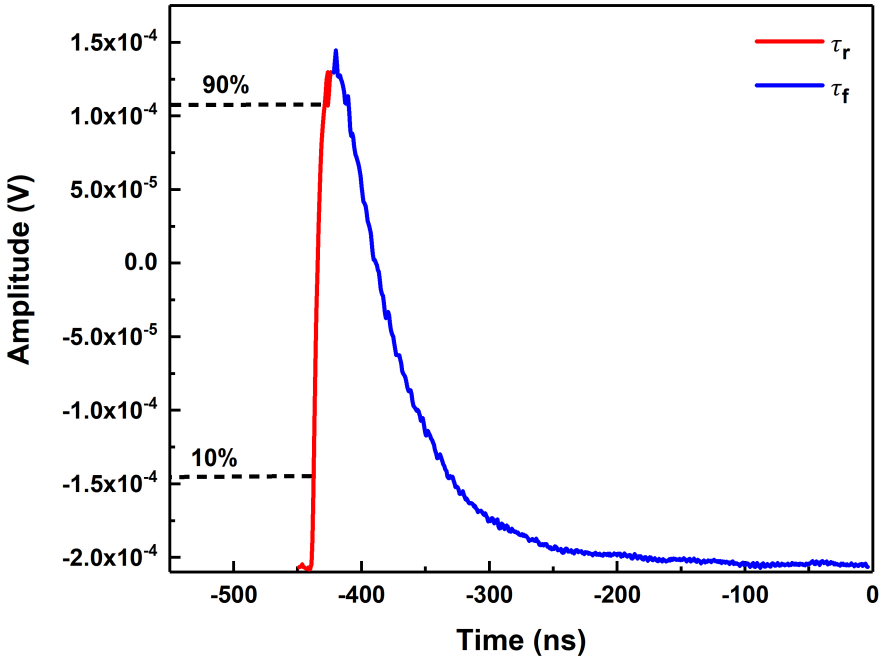

Figure 5.12: An example demonstrating the estimation method of τ_r (red line) and τ_f (blue line) using 1 p.e pulse signal. The τ_r was calculated as the difference between the 10 and 90% of the pulse rising part.

processes. In this configuration, the rise time (τ_r) and fall time (τ_f) of the SiPM were measured using the resultant 1 p.e pulse shape. The τ_r was estimated as the interval between the times at which the pulse rises to 10% and 90% of its highest amplitude, while the τ_f was measured starting from the falling part of the signal as shown in Figure 5.12.

The τ_r does not show any significant changes with varying other parameters in this experimental configuration. The τ_r was found in the range of 3.2±0.7 ns at different temperatures and overvoltages. This is due to the fact that τ_r is related to the charge carriers migration time from the point of their formation across the depletion region [272]. Therefore, τ_r is short and limited by the charge transit time in SiPM where high electric field is applied across the very small width of the depletion region.

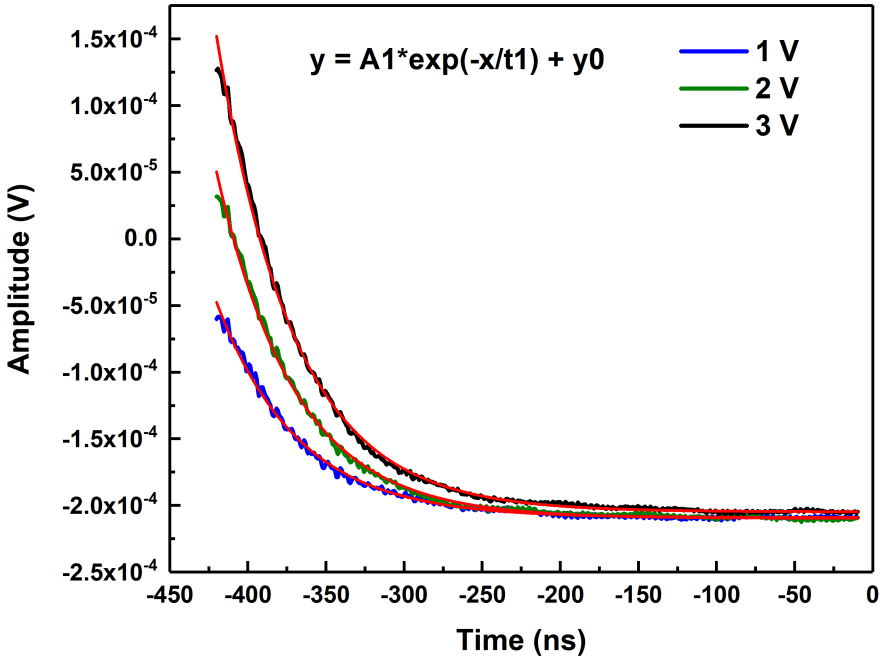

Figure 5.13: Exponential fitting for the slow time component extracted from the 1 p.e waveform obtained by applying different overvoltages at 15 ˚C. The red lines represent the exponential fit to the τ_f. The decay fitting function is shown.

The other parameter is the τ_f, also called time constant; it was calculated using exponential function that fitted to the falling portion of the 1 p.e waveform as illustrated in Figure 5.13. The signal was measured for each 1 p.e at each overvoltage and temperature with obtained error by varying the fitting in ±10 ns. The typical fall time for this type of SiPM is in the range between 31.7±0.3 to 36.3±0.4 ns at different applied overvoltages and temperatures.

The relation between τ_f and temperature is plotted in Figure 5.14 where τ_f decreased as temperature increased with varying overvoltage values. The τ_f is influenced by the dependence on C_j recharging through the quenching resistor R_q. Therefore, τ_f increased as C_j and R_q increased; however; other factors can also delay the fall time including; geometric fill factor, pixel size and R_q doping concentration [272, 273]. Other factors also could degrade the best achievable time resolution properties such as additional photon time transfer spread and imperfection in light transfer efficiency of emitted scintillation light as well as the influence of the electronic readout circuits [274, 275, 276].

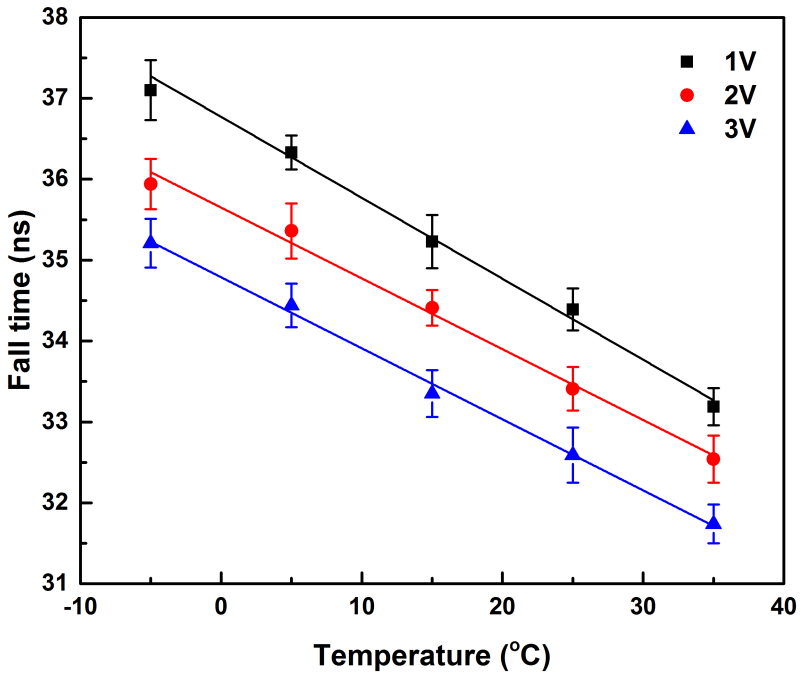

Figure 5.14: The relation between the fall time as a function of temperature at different overvoltages. There is a measured temperature coefficient of $-0.1 \pm 0.003\ ns/^{\circ}C$ for the decreased fall time values.

5.3.5 Quenching resistance

The fall time τ_f represents the time constant of the junction capacitance recharge through the quenching resistance. Therefore, by using the extracted fall time values mentioned above at different overvoltages and temperatures, the quenching resistance R_q can be calculated using equation 5.3 [67]. Figure 5.15 represents the relation between R_q and temperatures at different overvoltages. A linear decrease of R_q is observed with increasing temperature and overvoltage. This is could be due to the effect of the Joule heating at higher temperature that reduce the resistance and would keep R_q in the avalanche process [272, 273].

$$\tau_f = R_q \times C_j \tag{5.3}$$

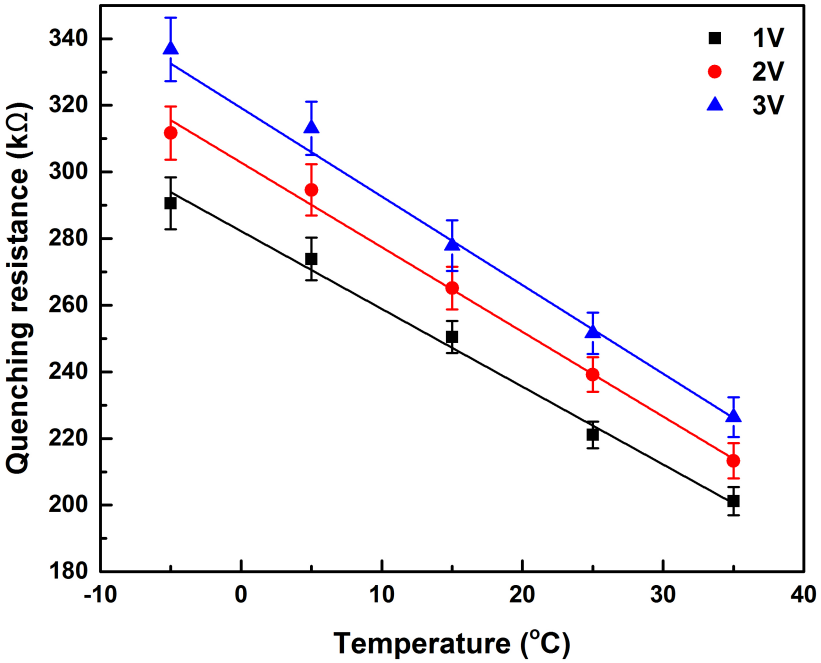

Figure 5.15: Quenching resistance of a single cell as a function of the temperature at different overvoltages. R_q decreases as temperature increases with a temperature coefficient of $-2.65 \pm 0.13\ k\Omega/^{\circ}C$.

5.3.6 Dark counts

As discussed previously in section 2.3.6.5, dark count is considered as one of the main sources of noise in SiPM which generated by thermal electrons. The dark count level depends on the active area, overvoltage and temperature. Therefore, the influence of overvoltages and temperatures on the dark count were investigated for the tested SiPM with no threshold applied. Figure 5.16 demonstrates an example for dark count spectra at 3 V overvoltage and different temperatures in the absence of any light source. Dark counts presumably are generated in the first p.e peak but entries in the second p.e and higher are also considered as dark counts [277]. The first peak to the left in Figure 5.16 is the noise pedestal at all temperature values. The first and second p.e. are also shown to be increasing as temperature increases.

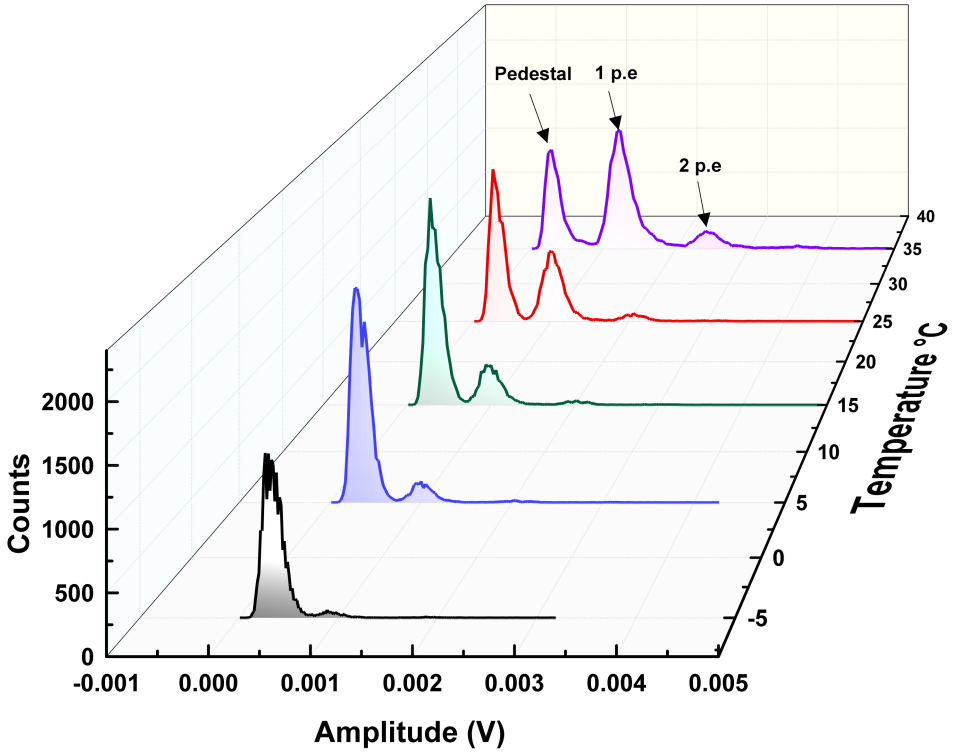

Figure 5.16: An example for the dark count spectra of the SiPM obtained at 3V overvoltage and at different temperatures.

Using the previous method, dark counts at various overvoltages and temperatures were measured. The charge under the area of the 1 p.e and higher was integrated to estimate the dark counts. Figure 5.17 demonstrates the dark count versus increased temperature at different overvoltage. The influence of temperature on the dark counts is shown clearly. For example, at 3V overvoltage, the dark count rate was 172 e^- $pixel^{-1}s^{-1}$ at -5 °C while it significantly increased to 2104 e^- $pixel^{-1}s^{-1}$ at 35 °C. This is because further increase in temperature generated more thermally excited electrons that increased dark counts significantly [265, 266]. Also, at a temperature of 15 °C, the dark count rate was 12 e^- $pixel^{-1}s^{-1}$ at 1 V which was increased to 466 e^- $pixel^{-1}s^{-1}$ at 3 V. This increased dark count is due to the increased probability of breakdown condition which in turn enabled more current growth as discussed in Chapter 2 section 2.3.6.1. It is obvious that temperature has a more dominant influence on the dark count than the applied overvoltage in SiPM.

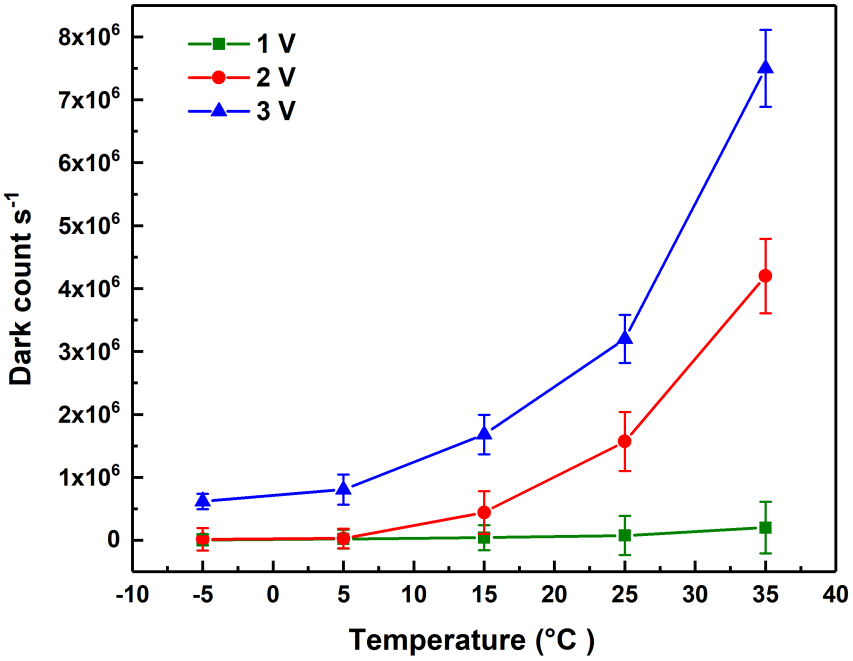

Figure 5.17: Measured dark counts per second at varied temperatures and different overvoltages. Dark counts significantly increase at high temperatures.

5.3.7 Crosstalk probability

Crosstalk is considered as a source of noise; therefore, resultant dark count spectra were used to determine the crosstalk probability at different temperature and overvoltage values. A dark count event around the located 1 p.e can induce a crosstalk photon that fires neighbouring APDs [277]. This process will initiate another event in the second p.e as a crosstalk event which is shown previously in Figure 5.17. The crosstalk probability was calculated as the ratio between events under the second p.e to events under the first p.e. Figure 5.18 illustrates the crosstalk probability as a function of temperature at different operating overvoltages. It is shown that the fraction of crosstalk increases as the temperature and overvoltage increased.

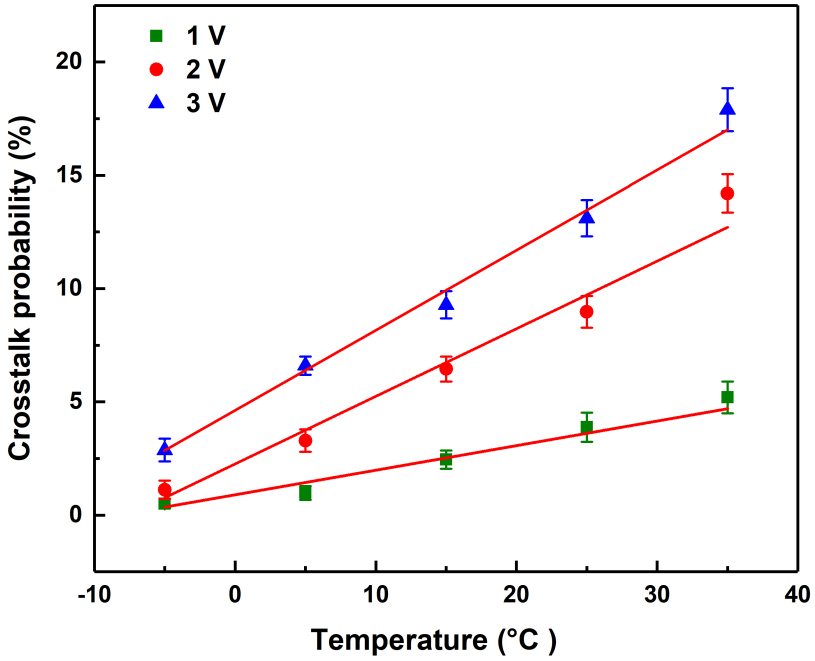

Figure 5.18: Calculated crosstalk probability as a function of temperature and at various operating overvoltages.

It is important to mention that the obtained dark count and crosstalk probability in this setup were almost double the values given by the manufacturer at 25 °C and 3V. This is because of the applied threshold of 0.5 p.e in the manufacturer measurement setup. Therefore, further decrease of the dark count and crosstalk probability can be achieved when applying a threshold based on the required application.

5.4 Conclusion

SiPM technology has emerged as a novel gamma radiation detection device in intraoperative imaging application. In this study, the main properties of SiPM including the break down voltage, gain, diode capacitance, quenching resistor, time response, dark counts and crosstalk probability were investigated to obtain a deep insight in SiPM device physics. Varying temperatures demonstrated to have a significant impact on all SiPM operation parameters. The most strongly

affected parameters are the breakdown voltage, gain and the dark count in particularly at high temperatures. Therefore, it is necessary to operate SiPM at a fixed temperature to ensure a constant breakdown voltage and consequently a stable gain. Cooling down the SiPM may be needed to suppress the dark counts to increase the sensitivity for low-light detection. For a miniature medical device, a stabilising system for the breakdown voltage could be sufficient to operate SiPM-based system at the room temperature to ensure a stable gain performance. The next plan is to test the SiPM as light readout for CsI [TI] and GAGG scintillators using a wide range photon energies from different radiation sources to investigate the effectiveness of the new configuration for different applications.

Chapter 6

Comparison between monolithic GAGG:Ce and columnar CsI:TI coupled to SiPM for intraoperative gamma imaging

6.1 Introduction

SFOV gamma cameras provide surgeons with additional information that enhances their capability to identify and confirm complete removal of intended lesions intraoperatively. These imaging tools have several useful features including more precise delineation of the target, straightforward real-time information and image-based documentation of radioactive distribution of the excised target [278, 15, 279]. The use of SFOV gamma cameras have been reported for various anatomical localizations, including, for example, SLN assessment, breast surgery, head and neck cancers, brain tumours, gastrointestinal malignancies and melanoma [116, 123, 136, 280]. Currently, there are a wide range of SFOV intraoperative gamma camera systems which have been discussed with more details in Chapter 3.

However, when designing an appropriate system, it should be considered that the performance of a gamma camera will be limited by the intrinsic compromise between the sensitivity and spatial resolution [76, 281]. Therefore, the best gamma camera is assumed to be the one having the best trade-off between

these two factors predicted by the specific application. For instance, in SLN biopsy during breast cancer surgery, sensitivity is considered the most important parameter to detect a lymph node due to activity uptake as low as ~20 kBq [282, 283]. On the other hand, spatial resolution could be more important, although always desirable, in complete SLN and tumour resection.

Inorganic scintillators have been the mainstay in majority of medical diagnostic equipment. The ideal scintillation material should possess a high light yield, good energy resolution, high density, fast scintillation time and no intrinsic radioactivity [40, 76]. One of the most versatile and efficient scintillators that has good properties and is widely used in medical imaging is thallium-doped caesium iodide (CsI:TI) [40]. This scintillator features adequate density, good light yield, is relatively inexpensive, widely available and has well-matched spectral response to a number of detector types, eg. PMTs, CCDs and SiPM. Furthermore, CsI:TI can be manufactured in either single crystal or a special micro-columnar form that behaves as an array of isolated scintillators. This columnar structure inhibits lateral light from spreading within the scintillator and improves spatial resolution [40, 284]. For the nuclear medicine application, CsI:TI can be fabricated in a dedicated thickness that ranges between 100 µm to 3 mm [284].

Another relatively new scintillation crystal is Ce doped gadolinium aluminium gallium garnet ($Gd_3Al_2Ga_3O_{12}$:Ce or GAGG:Ce) [46, 49]. This crystal has high luminosity compared, for example, to lutetium-yttrium oxyorthosilicate (LYSO) and bismuth germanate (BGO). It also has higher density, higher light yield and faster rise and decay time constants than that of CsI:TI and NaI:TI crystals. Moreover, GAGG is non-hygroscopic, physically rugged and does not emit natural radioactivity, offering a wide range of applications. Table 1.6 shows the main properties of GAGG compared to the most common scintillators in medical imaging.

Recently, SiPM has become the detector of choice for different medical scanners due to their attractive characteristics [247, 248, 250]. This includes its high gain, small size, good time resolution, lower power consumption, insensitivity to magnetic fields, easy installation and compactness. Despite the fact that SiPM has higher dark count rates compared to PMTs and therefore requires gain control with temperature variations, several studies have demonstrated that SiPM can provide sufficient signal-to-noise levels without the need of a cooling system [242, 243, 244, 245, 266].

Scintillator	**CsI:TI**	**GAGG**	**LYSO**	**BGO**	**NaI:TI**
Density (g/cm^3)	4.5	6.63	7.1	7.1	3.6
Light yield (ph/MeV)	54,000	60,000	30,000	9,000	41,000
Decay time (ns)	1000	90	45	300	230
Peak emission (nm)	545	520	420	480	410
Hygroscopic	Yes	No	No	No	Yes

Table 6.1: Physical characteristics of the most common scintillators used in medical imaging [46, 284, 285].

Different studies have evaluated both scintillators' (CsI:TI and GAGG) performance using SiPM photodetector for a range of applications including medical imaging. Efthimiou et al. studied different scintillator crystal SiPM-based systems, including CsI:TI, for SPECT and PET imaging system [26]. This initial investigation showed an energy resolution of 23% for CsI:TI at 140 keV. Another study by Occhipint et al. coupled a 4 mm thick CsI:TI to SiPM for SPECT imaging, showing 12% energy resolution at 122 keV [286]. On the other hand, various reports show the good performance of GAGG in terms of energy and timing resolutions for gamma spectroscopy and hadron detection [246, 286, 287]. For example, Yamamoto et al. developed a small GAGG pixel (0.1 mm^2) coupled to a SiPM array for beta, alpha and gamma imaging [288]. Their study achieved a spatial resolution of 0.6 mm at ^{241}Am gamma energy. Another study reports an energy resolution of 9.4% at ^{137}Cs (662 keV) for 30 mm thick GAGG crystal for medical imaging [289].

Here, the study is conducted in the framework of the HGC project. It investigated two scintillator materials with different structural features, namely the columnar CsI:TI and continuous GAGG detector systems coupled to SiPM. The aim of the study was to evaluate the performance of a thin layer (1.5 mm) of both scintillators in a SiPM-based system for intraoperative gamma imaging. Intrinsic performance features such as linearity, intrinsic resolution and detection efficiency are described.

6.2 Materials and methods

This experiment investigated both scintillators, CsI:TI and GAGG:Ce. The CsI:TI has a columnar structure with dimensions of 3 × 3 × 1.5 mm^2 and was provided by Hamamatsu, Japan [290]. The GAGG was a monolithic slab with dimensions of 3 × 3 × 1.5 mm^2 and came from Advatech, UK [285]. Figure 6.1 shows microscopic images using scanning electron microscope (SEM) to show the different structure of both scintillators. The microscopic image of CsI:TI shows the existence of gaps between columns, while this defect does not exist in the GAGG layer. Scintillation light was collected by SiPM, which was characterised in the previous chapter, with dimension of 3 × 3 mm^2 and a pixel size of 50 µm manufactured by Hamamatsu, Japan [258].

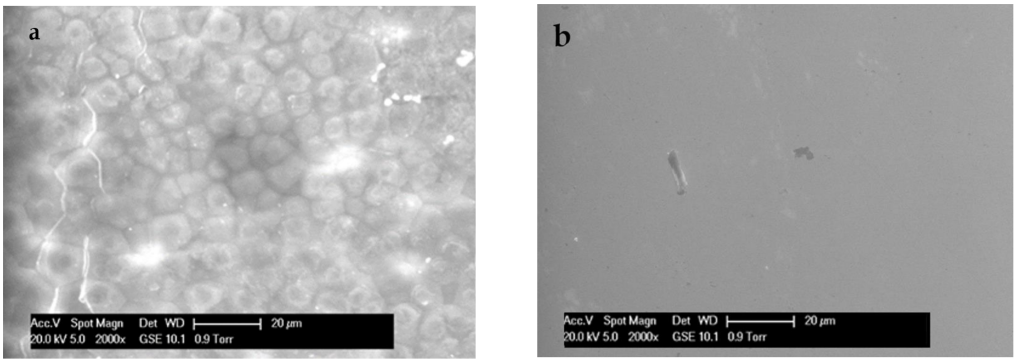

Figure 6.1: Images of the top surface of the samples using a scanning electron microscope (SEM) showing the columnar structure of CsI:TI in (a) and the non-pixelated GAGG layer in (b).

Figure 6.2 depicts the calculated percentage absorption with photon energy dependence of 1.5 mm layers of CsI:TI and GAGG scintillators [293]. For CsI:TI, it can be seen that the K-absorption edges at 33 and 40 keV are significantly decreased while a 50% absorption fraction can be achieved at photon energy of 122 keV. The GAGG exhibits higher K-shell transition effect resulted from Gadolinium (Gd) at around 49 keV but it shows higher absorption probability of ~ 65% at 122 keV compared to CsI:TI.

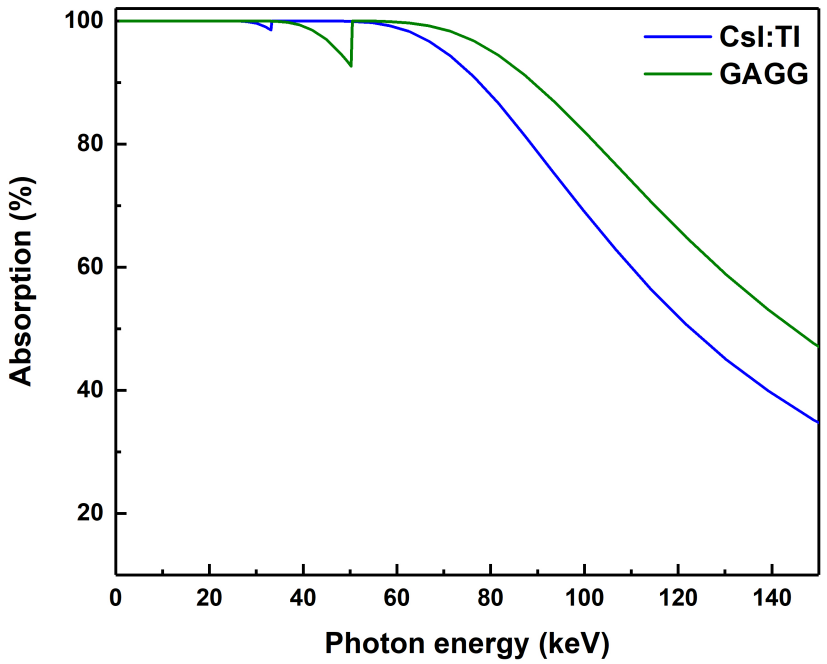

Figure 6.2: Percentage absorption of gamma photons through 1.5 mm thickness of CsI:TI and GAGG scintillators at different energies.

Both scintillators were wrapped with teflon tape to ensure that no light was scattered outside the scintillator through the edges as shown in Figure 6.3 [291, 292]. The exit region was kept uncovered to pass optical light directly to the SiPM surface. Both scintillators were optically attached to the SiPM using silicone oil (a refractive index of 1.403 with a viscosity of 100 k cSt at 25 °C) which was provided by Sigma-Aldrich [294]. The whole detector was then covered by reflective tape and placed in a light-light box to eliminate any possible interference from ambient light.

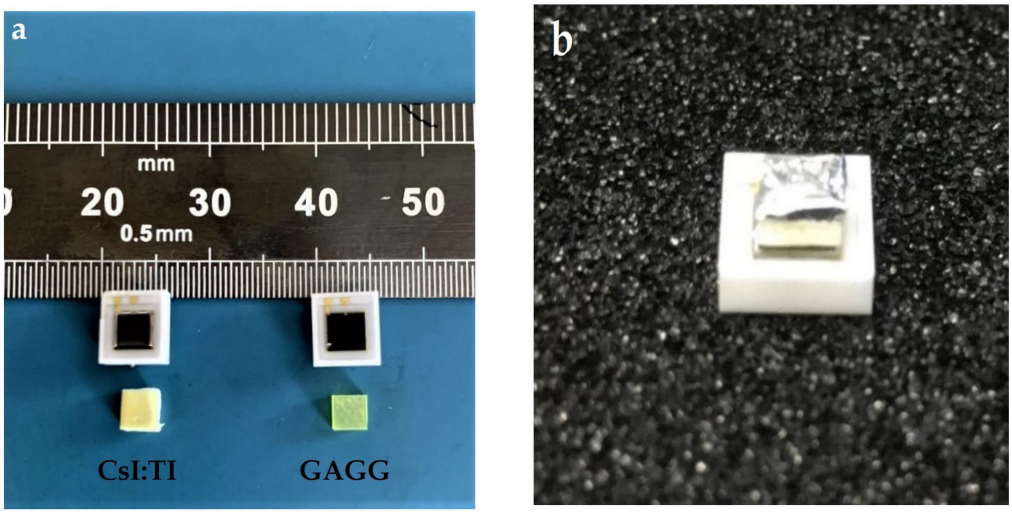

Figure 6.3: Illustration of scintillators and SiPM in (a) which were wrapped with layers of teflon and a layer of Al reflector and coupled to the SiPM using optical grease as shown in (b).

Each detector system then was attached to a circuit board with 1 kΩ bias resistor and a coupling capacitor. The SiPM operated at 54.4 V at room temperature of 18 °C. Both detectors were illuminated by X- or gamma rays using four radioactive sources, ^{55}Fe, ^{109}Cd, ^{241}Am and ^{57}Co. Table 6.2 shows the physical properties of these sources. The output signals were recorded on 12-bit high resolution oscilloscope from Lecroy [263]. The oscilloscope was triggered by the coincidence of incoming events. The threshold level was increased manually reaching 1.8 mV where almost no event was registered on the oscilloscope in the absence of the radioactive source. This was to raise the detection level above the noise contribution in acquired spectra. For each source, a trace of 10 ms contains 2.5×10^7 samples at 400 picosecond/sample was obtained in a trace file format which was then converted to a text file using a python script for further analysis [295]. The setup connection is illustrated in Figure 6.4.

Radioactive source	**Energy (keV)**	**Activity (MBq)**
^{55}Fe	6	150.6
^{109}Cd	22	38.3
^{241}Am	59	70.2
^{57}Co	122	19.6

Table 6.2: Physical properties of the radioactive sources used to evaluate both detector systems.

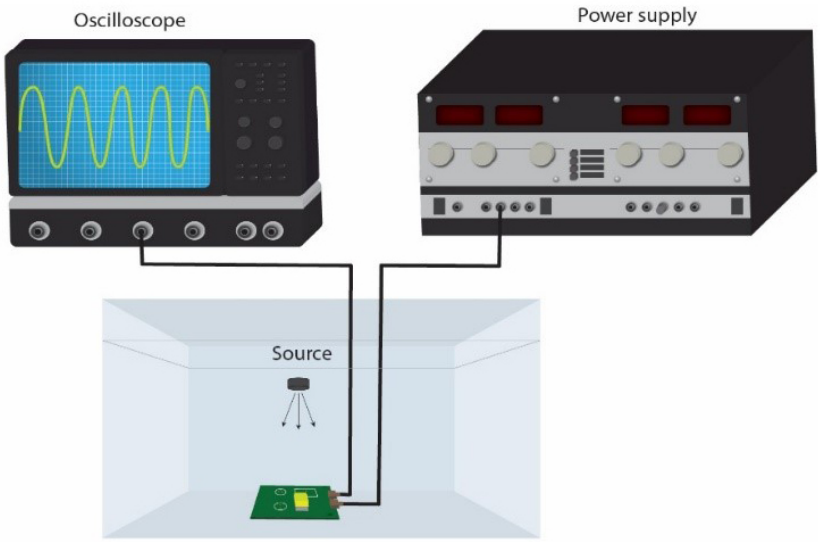

Figure 6.4: Illustration of the experimental setup where the source and the scintillators SiPM samples were placed within a tight-light box.

6.3 Results and discussion

6.3.1 Time response

The time response of both scintillators, CsI:TI and GAGG, was measured. The rise and decay times were determined at different photon energies at room temperature (18 °C). In this setup, all radioactive sources were placed at the same distance from the detector systems for each acquisition. Figure 6.5 represents the measured averaged pulse shape (100 k pulses) as a function of time in µs for both scintillators in the energy range between 6-122 keV. It can be seen that the variation in amplitude is a result of the variation of the light yield with increased photon energy for both scintillators. As a consequence of the increased amplitude, i.e increased charge, larger time is expected for charge collection. The rise time was estimated as the the interval between the times at which the pulse rises to 10% and 90% of its highest amplitude value.

Measured rise times for both scintillators produced from various photon energies are shown in Table 6.3. It is observed that the rise time decreased as photon energy increased because of the increased surge of charges within the SiPM.

Radioactive source	CsI:TI	GAGG
	Rise time (ns)	
^{55}Fe	304±9	139±6
^{109}Cd	236±6	91±3
^{241}Am	178±5	56±4
^{57}Co	151±7	37±3

Table 6.3: Measured rise times for CsI:TI and GAGG SiPM-based detectors for different photon energies.

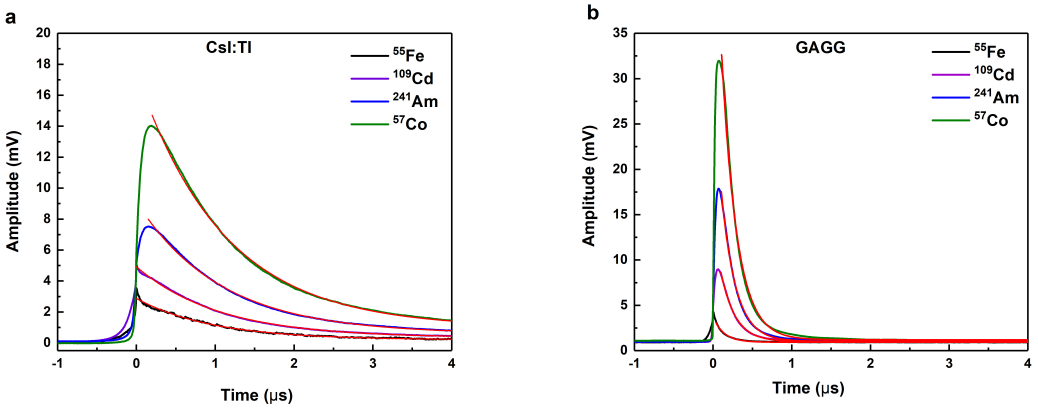

Figure 6.5: Averaged scintillation decay profiles for CsI:TI in (a) and GAGG in (b) produced by different radioactive sources. Red lines represent the exponential fit for the decay time.

CsI:TI showed slower rise time than GAGG; that could be due to the longer rise time of CsI:TI for the initial appearance of light (luminescent states) that subsequently produces slower decay times between these states [40, 41].

On the other hand, the decay time was estimated from the exponential function that fitted to the falling part of the pulse profile for each scintillator at each radioactive source as shown previously in Figure 6.5. The measured decay time for both scintillators are shown in Figure 6.6. The CsI:TI layer exhibited longer response time compared to GAGG at all tested radioactive sources. For example, the decay time of CsI:TI was about 740 ns compared to 150 ns for GAGG at ^{57}Co (122 keV). This larger decay time is combined with a persistent afterglow component which can be as high as 5% of the peak value for CsI:TI causing pulse pileup. Pulse pileup is an undesirable effect for high count rate applications [296].

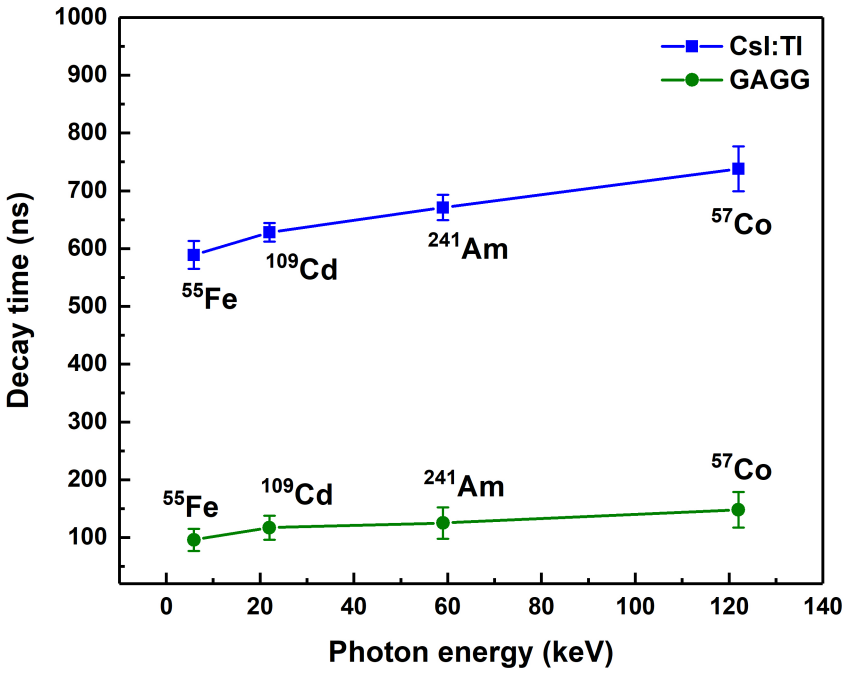

Figure 6.6: The dependence of decay time characteristics of CsI:TI and GAGG on energy deposited by X- and $\gamma-$rays ranging from 6 to 122 keV.

Unlike CsI:TI, the presence of Ce and Gd in GAGG improved scintillation time characteristics by shortening the rise time and suppressing slow decay and afterglow [49, 297]. Also, the higher density and the absence of intrinsic radioactivity of GAGG could increase the detection efficiency and, hence, a shorter scan time would be needed to generate the required statistics of signals compared to CsI:TI [298].

6.3.2 Pulse height distribution

Pulse height distribution (PHD) is considered the most common method used to deduce the fundamental characteristics of the radiation source and the detector output [40, 76]. Each individual pulse amplitude has important details regarding the differences in the energy of the incident radiation or the inherent fluctuations in the detector response. In this experiment, CsI:TI and GAGG coupled-SiPM were exposed to radioactive sources using an identical setup where pulse height spectra were obtained.

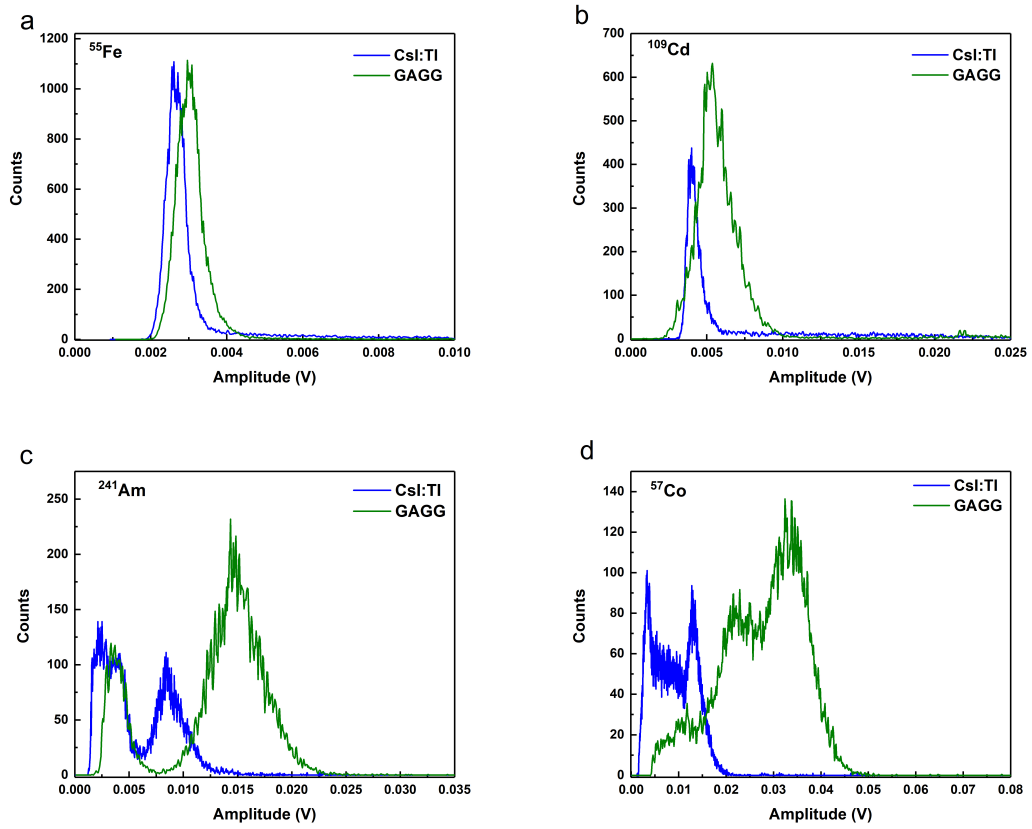

Figure 6.7: Pulse height spectra before correction for CsI:TI and GAGG of the radionuclides (a) ^{55}Fe, (b) ^{109}Cd, (c) ^{241}Am and (d) ^{57}Co.

Using a discriminator threshold of 1.8 mV, the PHD spectra features of different radioactive sources were obtained. These features were then used to evaluate the linearity of gamma radiation, determine the energy resolution and detection efficiency for each scintillator. Figure 6.7 shows obtained PHD before calibration for both scintillators using different radioactive sources in the energy range between 6 and 122 keV.

The energy calibration lines of both scintillation crystals were measured to evaluate the linearity of pulse height vs γ-rays energy. Figure 6.8 demonstrates the correlation between the measured amplitude versus the known energy of incident photons. The relation between the measured signal and the photon energy is well described by a linear function. The R^2 value for these fitted linear equations were found to be 0.995 and 0.997 for CsI:TI and GAGG, respectively. The resultant linear regression equation 6.1 was used to calibrate the energy spectrum for each scintillator and each energy from the radioactive source.

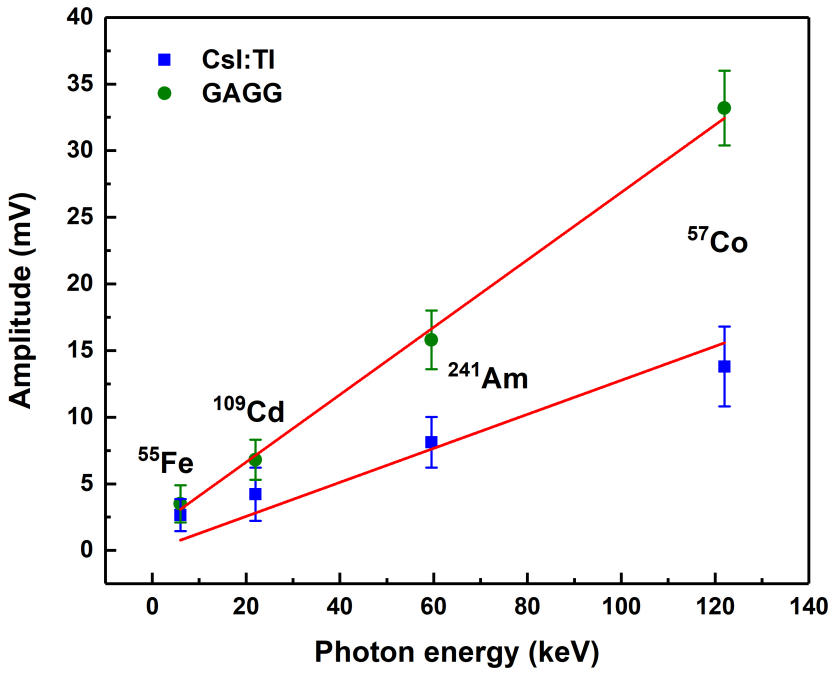

Figure 6.8: The correlation between the measured amplitude as a function of the known energy of different radioactive sources.

$$y = a + bx \tag{6.1}$$

where y is the output voltage, x is the incident photon energy, a and b are the intercept and the slope for each linear fit.

6.3.3 Energy resolution

An important aspect in radiation detection is the energy resolution at which the detector is able to distinguish between two energy lines that lie near each other. The linearity of γ-rays energy for the CsI:TI and GAGG was used to calibrate each energy spectrum for each source using equation 6.1. Figure 6.9 shows the calibrated energy spectrum of the ^{55}Fe source generated for the CsI:TI and GAGG SiPM-based systems. Both peaks were fitted to a Gaussian function at two energy lines, i.e. 5.9 and 6.5 keV. These peaks are a combination of different energies from the collected charges produced by incident characteristic X-ray of K_α and K_β shells of manganese (Mn).

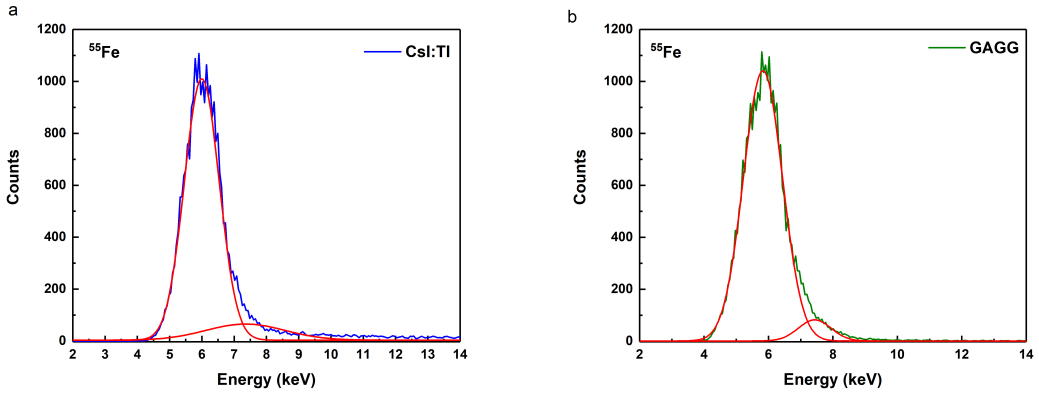

Figure 6.9: Measured energy spectra for (a) CsI:TI and (b) GAGG produced from ^{55}Fe fitted with multiple Gaussian fitting functions at 5.9 and 6.5 keV.

The GAGG and CsI:TI showed a slight difference in photon counts that could be due to the similar photoelectric fraction of the absorption coefficient at this energy range (6 keV) and 1.5 mm scintillator layer thickness. It can also be seen that CsI:TI has larger tail pile-up than GAGG which could be a result of the superposition of new pulses on the longer-duration tail of preceding pulses. This can be attributed to the longer decay time of the CsI:TI compared to GAGG that has been already discussed in the previous sections.

Both scintillators based-SiPM were exposed to higher energy photons emitted from ^{109}Cd source. Figure 6.10 describes the response function for CsI:TI and GAGG, showing the principle full-energy-peaks emitted by K_α (22 keV) and K_β (25 keV) X-rays of silver (Ag). Both PHDs were fitted to multiple Gaussian functions at both photon energy lines (i.e. 22 and 25 keV). The tail pile-up effect is also shown in the CsI:TI curve to be higher than that of GAGG.

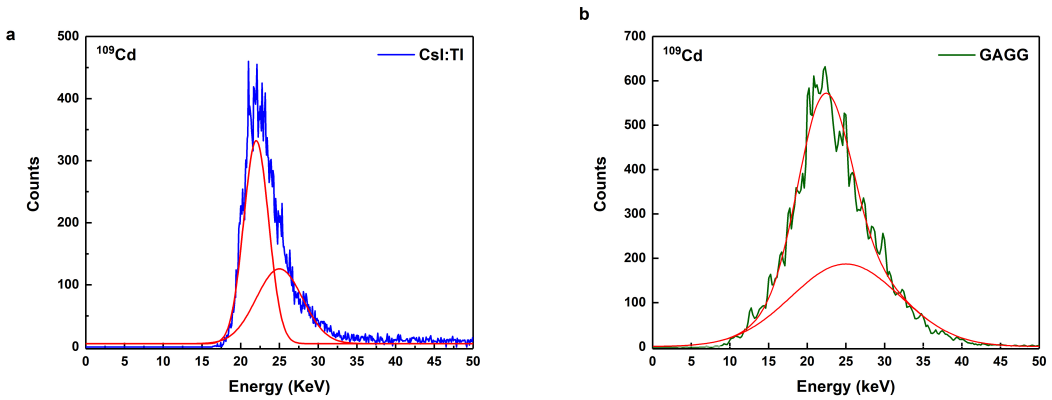

Figure 6.10: Pulse height distribution showing the main photopeaks for ^{109}Cd produced from (a) CsI:TI and (b) GAGG. Both photopeaks fitted to a Gaussian function at energy lines of 22 and 25 keV.

The energy spectra of CsI:TI and GAGG resulting from ^{241}Am source are diagrammed in Figure 6.11. For both scintillators, the expected full energy photopeak from the excited state of neptunium (Np) is shown at around 59.6 keV. The peaks between 10 to 22.5 keV are more likely to be generated by the ^{241}Am source which emits X-ray L-shell transitions of Np. In the CsI:TI curve, further peaks were observed at energy higher than 20 keV which could be initiated from the detector itself, i.e. the secondary fluorescence X-ray from I K-shell at 28 keV and Cs K-shell at 31 keV.

It is apparent that the fluorescence effect is more pronounced for CsI:TI than GAGG, particularly at energy range 28–31 keV. It is known that the mean free path of Cs and I secondary K-shell X-rays can extend typically from 300 µm to few millimetres apart from the primary interaction site [175, 233]. Consequently, and due to the thin layer (1.5 mm) of the scintillator, secondary photons contribute more to the energy spectrum. These curve features can be a drawback of CsI:TI particularly when considering clinical imaging in the proximity of this energy range such as ^{125}I source (27 keV).

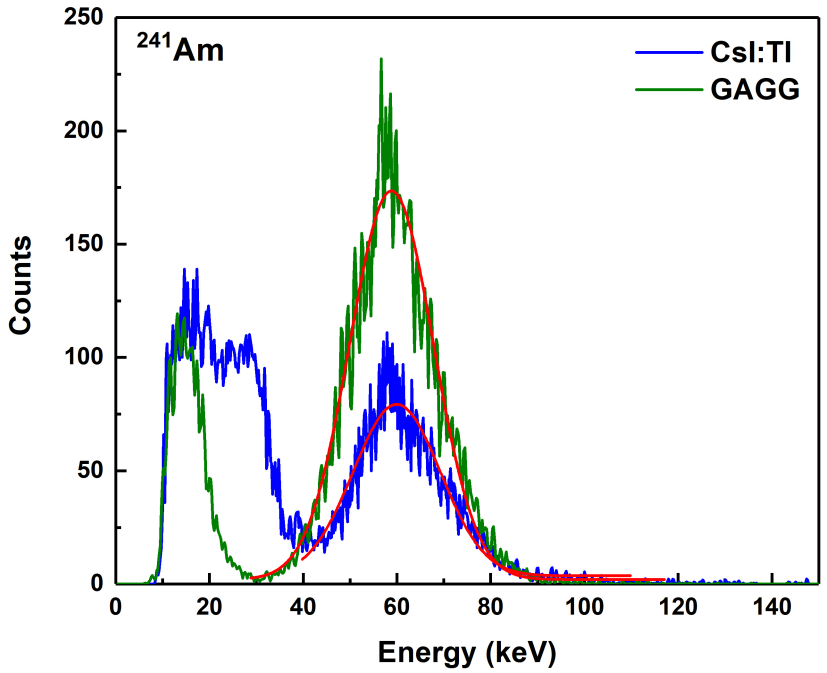

Figure 6.11: The main photopeaks of CsI:TI and GAGG at 59.6 keV using ^{241}Am source with a Gaussian fitting for the main photopeaks.

Similar findings were also discussed by different studies that used CsI:TI coupled with EMCCD including simulations and experimental configurations for ^{241}Am and higher energy sources [175, 233, 297, 298].

Figure 6.12 illustrates calibrated PHD curves produced for both scintillators using ^{57}Co. The full energy peak is shown at 122 keV. This peak is formed by emitted photons from the internal conversion of ^{55}Fe. Similar to ^{241}Am, multiple low energy peaks were recorded at around 28 and 30 keV corresponding to the CsI fluorescence effect. This effect was less pronounced for the GAGG crystal.

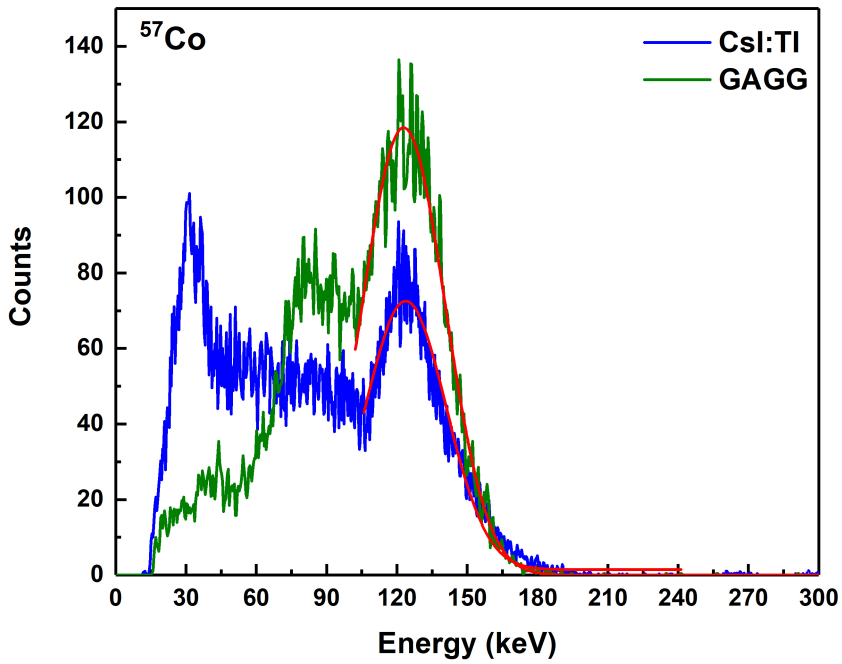

Figure 6.12: Energy spectrum recorded with CsI:TI and GAGG-SiPM from ^{57}Co shown with a Gaussian fitting function.

Based on the obtained PHDs, energy resolution was then calculated using the relation between the measured full width at half maximum (FWHM) from the Gaussian distribution fitting of the main photopeak divided by the peak centroid as follows (12):

$$Resolution = \frac{FWHM}{Peak\,Centroid} \tag{6.2}$$

Figure 6.13 illustrates the calculated energy resolution as a function of the radioactive source energy. For the ^{55}Fe source, calculated intrinsic resolution showed an energy resolution of 61.7% and 54.2% for CsI:TI and GAGG, respectively. The poorer energy resolution of CsI:TI could be a consequence of the larger tail pile-up effect on the pulse height measurement in comparison to GAGG. Tail pile-up effect can worsen the energy resolution by adding a wing-like shape to the recorded peak which in turn leads to a broader FWHM [40]. The measured energy resolution was at 71.6% and 68.3% for CsI:TI and GAGG at ^{109}Cd, respectively. It can be seen that the resolution worsened at this photon energy

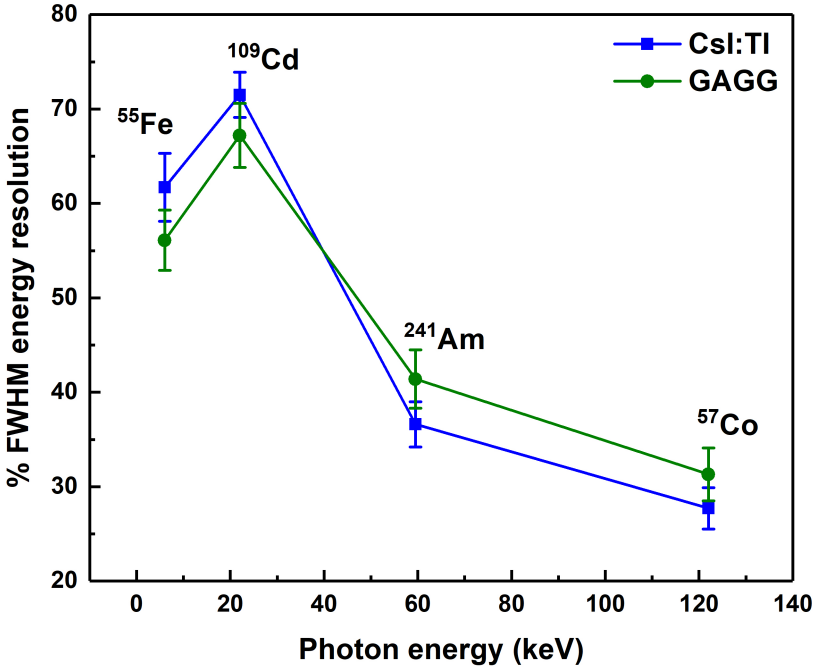

Figure 6.13: The calculated energy resolution for CsI:TI and GAGG at different radioactive sources in the energy range between 6 to 122 keV.

due to the added broader FWHM that was fitted to 25 keV energy line. At this energy line, the tail pile-up also has a negative influence on the measured energy resolution, in particular for the CsI:TI. At ^{241}Am source, energy resolution of 36.6% and 41.2% was obtained for CsI:TI and GAGG, respectively. Finally, the calculated energy resolution for ^{57}Co was 27.4% and 31.3% for CsI:TI and GAGG, respectively.

In this experiment, GAGG crystal recorded slightly better energy resolution than CsI:TI at lower photon energy sources, i.e. ^{55}Fe and ^{109}Cd. This can be attributed to the faster time characteristic response of GAGG that reduced the tail pile-up effect compared to CsI:TI. However, CsI:TI exhibited better intrinsic resolution, although with slight differences, in comparison to GAGG for ^{241}Am and ^{57}Co.

In general, scintillation γ-ray detectors have relatively poorer energy resolution in comparison to semiconductors. This poorer capability is assumed to be a result of the limited resolution that is mainly originated from the assumption that

scintillation photons are Poisson distributed [40, 299, 300]. Therefore, the energy resolution will be influenced by the Poisson statistics of formed electrons in the SiPM which are essentially proportional to the light yield. This can explain the poorer energy resolution at lower photon energy sources (^{55}Fe and^{109}Cd), i.e lower light yield that was associated with higher statistical fluctuations that may resulted from the noise contribution. The noise pulse may arise from the SiPM or associated electronics that can be difficult to discriminate from small pulses produced by low gamma energy photons [67]. Other parameters that also affect the intrinsic energy resolution include non-uniformity of the light collection, quality of the crystal wrapping, optical coupling, readout device and SiPM bias overvoltage.

The intrinsic energy resolution of CsI:TI and GAGG was also investigated as a function of the SiPM operating overvoltage. In this configuration, ^{109}Cd was used while the operating overvoltage varied between 1 to 4 V for both scintillators. The overvoltage of the SiPM was determined by subtracting the breakdown voltage from the operating voltage. The variation of the non-calibrated energy resolution at different overvoltage for ^{109}Cd is shown in Figure 6.14. It can be seen that at lower overvoltage, the efficiency of triggering the initial avalanche is low and the correlated noise from different sources, such as electronic noise, dark counts and optical crosstalk, is high. This strongly influenced the PDE leading to lower photon counts and hence, poorer energy resolution. The best achieved energy resolutions for both scintillators were between 2.5 and 3.5 V, which comply with the recommended operating voltage by the manufacturer. At higher applied overvoltage, the PDE reached saturation as the trigger efficiency reached its maximum. While PDE is saturated, high gain is associated with very high level of dark count rates and optical crosstalk probability which eventually contributed again to the low photon counting and worsen energy resolution. Thus, a careful compromise between these parameters should be useful in order to obtain the maximum energy resolution.

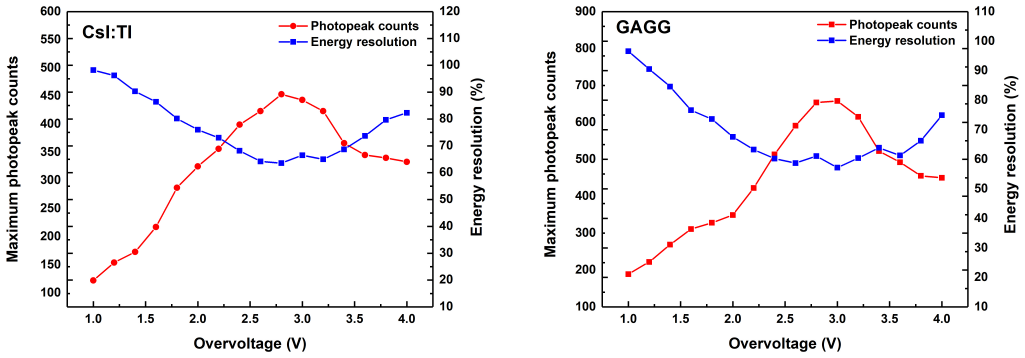

Figure 6.14: Variation of obtained energy spectra as a function of the applied SiPM overvoltage using ^{109}Cd source for CsI:TI and GAGG.

6.3.4 Full energy peak efficiency

Photon detection efficiency (PDE) provides a precise value for the scintillator in order to relate the number of counted pulses to the number of emitted photon by the radioactive source [40]. The intrinsic full energy peak efficiency principle was used to measure the probability that incident photons on the scintillator surface will deposit their energy in the detector. The number of photons impinging the detector surface was estimated using the solid angle (Ω) between the source and the detector via the following equation [301]:

$$\Omega = 4\,tan^{-1}\frac{ab}{2r\sqrt{a\,(r)^{\,2} + a^2 + b^2}} \tag{6.3}$$

where a and b are the detector dimensions, and r is the source-detector-distance. Using the resultant solid angle value, the number of incident counts on the detector was calculated using this equation for each source [40]:

$$Incident\,counts = \frac{\Omega}{4\pi} \times Activity \tag{6.4}$$

The ratio between the number of counts under the full-energy peak and the number of incident photons on the detector was calculated for all sources. Figure 6.15 shows the variation of the intrinsic photo-peak efficiency within the energy

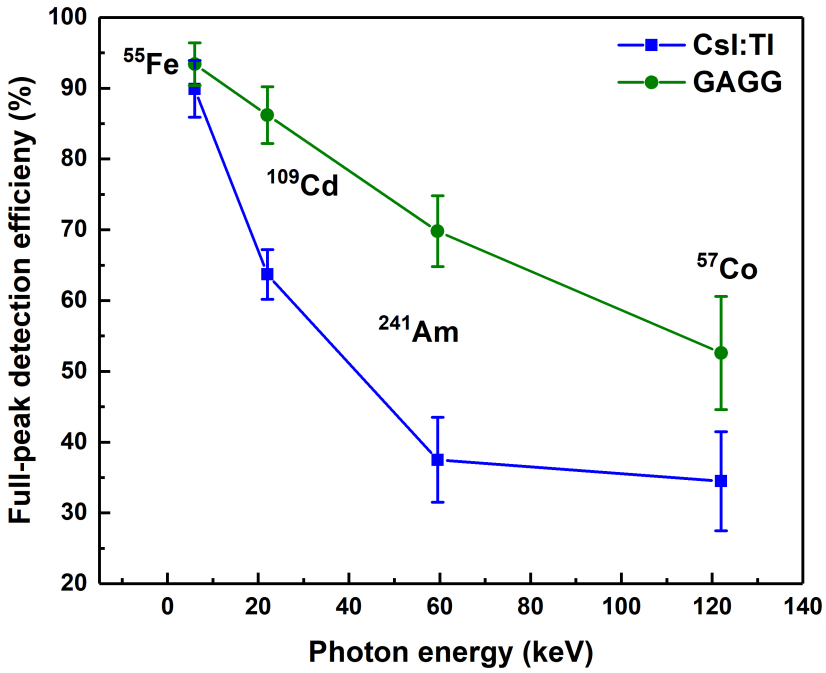

Figure 6.15: Calculated full-energy peak efficiency for CsI:TI and GAGG for energies between 6 and 122 keV.

range between 6-122 keV for CsI:TI and GAGG scintillators. The plot exhibited decreasing PDE with increasing photon energy due to the dominant photoelectric absorption interaction at lower energies which contributed to a larger number of pulses at the photopeak position. At higher energy photons, the photoelectric effect decreases, while Compton scattering probability increases, leading to a partial contribution to the full-energy peak. Nevertheless, higher energy photons have higher penetrating ability and can pass through the whole detector system without undergoing any interaction, particularly when thin scintillator layer is used leading to lower count probabilities.

The CsI:TI scintillator showed lower intrinsic DE than GAGG at all energies which could be due to the larger density of GAGG and the existing dead-spaces between the adjacent columns in CsI:TI. There was a percentage difference of 6.7% in DE between both materials at ^{55}Fe which then increased to 67% and 47% at ^{241}Am and ^{57}Co, respectively. This showed that intrinsic efficiency is a parameter dependant primarily on the incident photon energy and detector material and structure. However, the resulted DE was lower than the theoretical

calculation that have been shown previously in Figure 6.2 for both types. This can be attributed to the fact that scintillation light will spread isotropically from the primary interaction point [40, 300]. Therefore, there will be lost fractions of light due to the emitted fraction in the opposite direction to the SiPM region, absorbed fraction in the scintillator material and reflected fraction in the optical connecting material.

Both scintillator materials SiPM-based gamma detection could provide valuable properties to an intraoperative imaging camera in terms of size, cost and physical performance. The columnar structure of CsI:TI showed poorer energy resolution at lower energy ranges due to the longer timing properties. This caused tail pile-up effect to be more pronounced for the CsI:TI than the GAGG layer. The GAGG presented better sensitivity at all tested energy ranges.

One of the main limitation of columnar CsI:TI could be the production of stacks with thickness of more than 3 mm, therefore, and with the advent of ultra-high resolution GAGG with a pixel size of (0.1 mm) and larger thicknesses, a dual intraoperative SPECT/PET GAGG-based design with a removable collimation system could be more achievable for preclinical studies. This may ensure a good spatial resolution without sensitivity detriment, leading to extended application for wider energy ranges in medical application. Contrary to CsI:TI, GAGG crystal is not hygroscopic; therefore, detector housing within a pressurised chamber may not be required. A common challenging point of using a monolithic crystal with collimators in SPECT application is the relatively poorer spatial resolution. This is due to errors in localising the depth of interaction (DOI) of gamma events within the scintillator layer [302, 303]. However, development of various position DOI algorithms could improve the imaging capability in different medical imaging modalities [304, 305, 306].

6.4 Conclusion

Intraoperative gamma imaging has been widely introduced to visualise activity distribution in the anatomic region of interest. Such an imaging system requires a small, lightweight and compact design that produces high quality images. In this study, a columnar CsI:TI and non-pixelated GAGG SiPM-based detector samples were investigated within energy range between 6 to 122 keV in terms of linearity, energy resolution and detection efficiency. Both detectors showed

good linearity within the studied energy range with thickness as low as 1.5 mm. The CsI:TI showed slower rise and decay times compared to GAGG due its inherent scintillation properties. The GAGG exhibited better sensitivity and intrinsic energy resolution at low photon energy, while the CsI:TI showed better intrinsic energy resolution at 59.6 and 122 keV. Both materials could be good candidates for intraoperative SFOV gamma camera. Improvement of intrinsic resolution and sensitivity parameters can be achieved based on the intended design and imaging photon energy range. Therefore, to design such an imaging system further investigations are required, taking into account the influence of different parameters such as crystal inherent properties, required thickness, wrapping method, optical coupling, variations in SiPM operating voltage and using sophisticated readout circuit.

Chapter 7

Conclusion and future work

The HGC has been developed to aid various diagnostic and therapeutic nuclear medicine procedures. The HGC capability has been evaluated previously via several theoretical, experimental and clinical studies by testing various designs and different radioactive concentrations in regions around the human body. These studies have suggested that the HGC has the potential to be a powerful imaging tool not only for clinical use but also for environmental radiation protection.

The aim of this thesis was to investigate possible developments that could enhance the use of the HGC in surgical oncology. NIRF imaging can provide high-resolution and high sensitivity feedback with a real-time aid about tumour margins and vital structures during oncologic surgery. The first project was to exploit an intraoperative NIRF system through an experimental characterisation of different fluorescent cameras (XS and CP) and different fluorophore (ICG and 800CW) using different configurations. Phantom studies have been used to evaluate the performance of the fluorescent systems for imaging different fluorescent dyes. ICG could be detected at a minimum concentration of 1 μM while the lower thresholds for 800CW were 10^{-2} and 10^{-3} μM for the XS and CP cameras, respectively. Higher CNR values were observed when the excitation light was placed in an angled position to the target. Both cameras were unable to detect small-sized targets within a 3 mm depth, but were able to identify larger targets as deep as 7 mm. Further development of this system is required to merge the NIRF to the HGC providing a simultaneous NIRF-gamma imaging system.

This thesis also has studied the possible application of SiPM-based gamma detection system for intraoperative imaging. Thus, the main physical properties

of SiPM such as the break down voltage, gain, diode capacitance, quenching resistor, time response and dark counts and crosstalk probability were explored to obtain a deep insight in the physics of this device. The influence of temperature on SiPM performance has been shown to be significant on all measured parameters.

Moreover, a method for evaluating the intrinsic performance of scintillator-SiPM gamma detection system was developed to aid designs of the instrumentation. A comparative study was conducted to investigate thin layers of monolithic GAGG and columnar CsI:TI. The GAGG crystal showed better gamma energy response, energy resolution and detection efficiency.

The research has resulted in a number of different contributions that may lead to enhance the multimodality gamma-NIRF imagining system:

- Development of an experimental method to characterise the performance of NIRF imaging systems using bespoke phantoms.
- Characterisation of SiPM parameters to build the knowledge and understand their requirements for designing an imaging system.
- Designing an experimental setup to analyse the various properties of scintillators SiPM-based gamma detecting systems.

7.1 Limitation of this work

The work described in this thesis is characterised by a number of limiting factors that are discussed in this section. The performance of the NIRF imaging system was not evaluated using medical phantoms with different geometry such as breast, brain and head and neck regions. Moreover, the fluorescence dyes were dissolved in deionised water and PBS. A more practical situation can be achieved by diluting the fluorescence samples with albumin-enriched physiological salt solution (APSS). This is to mimic the fluorescence properties in the lymphatic system i.e. for sentinel lymph node mapping. Despite providing an *in vitro* evaluation method, the NIRF system was not validated using *in vivo* imaging or clinical trials.

The comparative study of the scintillator SiPM-based detectors was also limited as it only investigated samples of scintillators and SiPM. The experimental setup did not include a larger scaled detector system with the required electronic components. The oscilloscope used was sufficient enough to acquire the pulse signals. However, electronic components such as the preamplifier, amplifier, spectrum stabilisers, pileup rejection circuit, etc., will provide more accurate representation of the pulse-height spectrum leading eventually to the construction of a prototype camera. The scintillators intrinsic performance will also be influenced by the intended application, collimator type, reconstruction algorithm, electronics, wrapping method, encasing and shielding. Therefore, a complete design that exemplifies the whole gamma imaging characteristics could be more desirable.

7.2 Future work

The present work has mainly focused on two field, NIRF imaging and SiPM-based gamma detection systems. In this section, future technological development and possible clinical applications related to this work will be described. The ultimate aim of this improvement is to enhance cancer prognosis and reduce iatrogenic effects typically associated with therapy. The proposed areas of further studies can be divided into two directions, NIRF imaging and SFOV gamma camera using SiPM.

7.2.1 Visible-NIRF multispectral camera

Recently, a new design paradigm of CCD and CMOS has been developed to image coloured and NIRF images simultaneously. This new system can capture red, green, blue (RGB) and NIRF spectral bands providing rich image information about the location of cancerous tissue and SLN [169, 307, 308]. Therefore, the optical imaging system could be replaced by an RGB-NIRF customised imaging sensor. This potential solution would be extremely beneficial to improve the performance of the HGC in intraoperative procedures by combining the RGB-NIRF system with the gamma imaging modality.

7.2.2 Medical phantoms

With the advent of 3D printing technology and advanced software capability, more realistic anthropomorphic phantoms can be constructed. Tissue-equivalent phantoms should be used to evaluate not only the NIRF system but also the gamma imaging performance. This represents another area of improvement in order to validate and optimise both imaging systems.

7.2.3 Hybrid Compton camera

Compton imaging camera has been introduced as a promising gamma-ray detection method for astronomy, environmental radiation measurements, high energy physics and medical applications [309]. Compton camera has several advantages include imaging of high gamma energy (up to 10 MV), wide FOV, 3D imaging and can be designed without the need of a collimator [310, 311, 312]. In this modality two consecutive layers of a scintillator combined to two SiPM arrays can be constructed as a Compton camera.

This research direction can have a significant potential to improve the HGC application for various applications. The implementation of Compton principle in the HGC imaging system would require significant development work through the investigation of various scintillator size, scintillator thickness, readout circuits and imaging algorithms. The HGC can be designed without the need of the pinhole collimator which could reduce it's weight, increase imaging FOV and improve detection efficiency and spatial resolution. Combined Compton camera with visible or NIRF imaging system could have huge benefits for patients undergoing different medical procedures.

Such a hybrid system can be used for simultaneous visualization of various nuclides with photon energy range between a several of keV to a few MV. Compton camera with an optical reference could be of great importance in imaging prompt gamma (1-7 MeV) during proton therapy. As a consequence, range verification could be achievable leading to more precise dose deposition and improved therapy outcome. The proposed camera could also be used to visualise emitted X- and gamma ray produced in radionuclide therapy, preclinical studies, radiation environmental protection and monitoring.

Bibliography

[1] Crosby D, Lyons N, Greenwood E, Harrison S, Hiom S, Moffat J, et al. A roadmap for the early detection and diagnosis of cancer. The Lancet Oncology. 2020;21(11):1397-9.

[2] Frangioni JV. New technologies for human cancer imaging. J Clin Oncol. 2008;26(24):4012-21.

[3] Cancer Research UK. Cancer incidence 2020 [Available from: https://www.cancerresearchuk.org/health-professional/cancer-statistics-for-the-uk#heading-Zero].

[4] McLaughlin SA. Surgical management of the breast: breast conservation therapy and mastectomy. Surg Clin North Am. 2013 Apr;93(2):411-28. doi: 10.1016/j.suc.2012.12.006. Epub 2013 Feb 1. PMID: 23464693.

[5] Liu X-Y, Pestka S, Shi Y-F. Preface. In: Liu X-Y, Pestka S, Shi Y-F, editors. Recent Advances in Cancer Research and Therapy. Oxford: Elsevier; 2012. p. xvii-xviii.

[6] Kubben PL, ter Meulen KJ, Schijns OEMG, ter Laak-Poort MP, van Overbeeke JJ, Santbrink Hv. Intraoperative MRI-guided resection of glioblastoma multiforme: a systematic review. The Lancet Oncology. 2011;12(11):1062-70.

[7] Besana-Ciani I, Greenall MJ. The importance of margins status after breast conservative surgery and radiotherapy in node positive patients: a follow-up of 10–15 years. International seminars in surgical oncology. ISSO: 2008;5-13.

[8] Sharma R, Wendt JA, Rasmussen JC, Adams KE, Marshall MV, Sevick-Muraca EM. New Horizons for Imaging Lymphatic Function. Annals of the New York Academy of Sciences. 2008;1131(1):13-36.

[9] Folkman, J. Tumor Angiogenesis: Therapeutic Implications. New England Journal of Medicine, 1971;285(21): 1182–1186.

[10] Rosenthal EL, Warram JM, Bland KI, Zinn KR. The status of contemporary image-guided modalities in oncologic surgery. Ann Surg. 2015;261(1):46-55.

[11] Zanzonico P, Heller S. The intraoperative gamma probe: Basic principles and choices available. Seminars in Nuclear Medicine. 2000;30(1):33-48.

[12] Heller S, Zanzonico P. Nuclear probes and intraoperative gamma cameras. Seminars in nuclear medicine. 2011;41(3):166-81.

[13] Moffat FL. Targeting gold at the end of the rainbow: Surgical gamma probes in the 21st century. J Surg Oncol. 2007;96(4):286-9.

[14] Woolfenden JM, Barber HB. Radiation Detector Probes for Tumor-Localization Using Tumor-Seeking Radioactive-Tracers. Am J Roentgenol. 1989;153(1):35-9.

[15] Perkins AC, Lees JE. Gamma Cameras for Interventional and Intraoperative Imaging. 1st ed: CRC Press; 2016.

[16] Gambini JP, Quinn TP. Hybrid tracers and devices for intraoperative imaging: the future for radioguided surgery? Clinical and Translational Imaging. 2016;4(5):343-51.

[17] Dip FD, Ishizawa T, Kokudo N, Rosenthal R, editors. Fluorescence Imaging for Surgeons; Concepts and Applications. 1 ed. Switzerland: Springer International Publishing 2015.

[18] Vahrmeijer AL, Hutteman M, van der Vorst JR, van de Velde CJH, Frangioni JV. Image-guided cancer surgery using near-infrared fluorescence. Nature reviews Clinical oncology. 2013;10(9):507-18.

[19] Bugby SL, Lees JE, Perkins AC. Hybrid intraoperative imaging techniques in radioguided surgery: present clinical applications and future outlook. Clinical and Translational Imaging. 2017;5(4):323-41.

[20] Hussain T, and Nguyen QT. 2014. Molecular imaging for cancer diagnosis and surgery. Advanced Drug Delivery Reviews, 66: 90–100.

[21] Solomon M, Liu Y, Berezin MY, Achilefu S. Optical imaging in cancer research: basic principles, tumor detection, and therapeutic monitoring. Med Princ Pract. 2011;20(5):397-415.

[22] Hebden JC, Arridge SR, Delpy DT: Optical imaging in medicine. I. Experimental techniques. Phys Med Biol 1997;42:825–840.

[23] Jaffer FA, and Weissleder R. 2005. Molecular imaging in the clinical arena. Journal of the American Medical Association, 293(7): 855–62.

[24] Cox CE, Salud C, Whitehead GF, Reintgen DS. Sentinel lymph node biopsy for breast cancer: combined dye-isotope technique. Breast Cancer. 2000; 7(4):389–397.

[25] Lees JE, Fraser GW, Keay A, Bassford D, Ott R, Ryder W. The high resolution gamma imager (HRGI): a CCD based camera for medical imaging. Nuclear Instruments and Methods in Physics Research Section A: Accelerators, Spectrometers, Detectors and Associated Equipment. 2003;513(1-2):23-6.

[26] Efthimiou N, Argyropoulos G, Panayiotakis G, Georgiou M, Loudos G. Initial results on SiPM performance for use in medical imaging2010. 256-60 p.

[27] Seitz B, Stewart A, O'Neill K, Wall L, Jackson C. Performance evaluation of novel SiPM for medical imaging applications. IEEE Nuclear Science Symposium Conference Record. 2013.

[28] Acerbi F, Gundacker S. Understanding and simulating SiPMs. Nuclear Instruments and Methods in Physics Research Section A: Accelerators, Spectrometers, Detectors and Associated Equipment. 2019;926:16-35.

[29] Queiroz MA, Delso G, Wollenweber S, Deller T, Zeimpekis K, Huellner M, et al. Dose Optimization in TOF-PET/MR Compared to TOF-PET/CT. PLOS ONE. 2015;10(7):0128842.

[30] Zeimpekis KG, Barbosa F, HÃŒllner M, ter Voert E, Davison H, Veit-Haibach P, et al. Clinical Evaluation of PET Image Quality as a Function of Acquisition Time in a New TOF-PET/MRI Compared to TOF-

PET/CT—Initial Results. Molecular Imaging and Biology. 2015;17(5):735-744.

[31] Melsaether AN, Raad RA, Pujara AC, Ponzo FD, Pysarenko KM, Jhaveri K, et al. Comparison of Whole-Body 18F FDG PET/MR Imaging and Whole-Body 18F FDG PET/CT in Terms of Lesion Detection and Radiation Dose in Patients with Breast Cancer. Radiology. 2016;281(1):193-202.

[32] Sonni I, Baratto L, Park S, Hatami N, Srinivas S, Davidzon G, et al. Initial experience with a SiPM-based PET/CT scanner: influence of acquisition time on image quality. EJNMMI Physics. 2018;5(1):9.

[33] Sekine T, Delso G, Zeimpekis KG, de Galiza Barbosa F, Ter Voert E, Huellner M, et al. Reduction of (18)F-FDG Dose in Clinical PET/MR Imaging by Using Silicon Photomultiplier Detectors. Radiology. 2018;286(1):249-259.

[34] Carminati M, D'Adda I, Morahan A, Erlandsson K, Nagy K, Nyitrai Z, et al. A SiPM-Based Clinical MRI-Compatible SPECT Insert2019. 1-3 p.

[35] Trigilio P, Busca P, Quaglia R, Occhipinti M, Fiorini C. A SiPM-Readout ASIC for SPECT Applications. IEEE Transactions on Radiation and Plasma Medical Sciences. 2018;2:404-10. 6.

[36] Brown JMC. In-silico optimisation of tileable Philips digital SiPM based thin monolithic scintillator detectors for SPECT applications. Applied Radiation and Isotopes. 2020:109368. 7.

[37] Popovic K, McKisson JE, Kross B, Lee S, McKisson J, Weisenberger AG, et al. Development and characterization of a round hand-held silicon photomultiplier based gamma camera for intraoperative imaging. IEEE Trans Nucl Sci. 2014;61(3):1084-91.

[38] Goertzen A, Thiessen J, McIntosh B, Simpson M, Schellenberg J. Characterization of a handheld gamma camera for intraoperative use for sentinel lymph node biopsy. IEEE Nuclear Science Symposium Conference Record. 2013.

[39] Bizzozero G. Development of high resolution compact detector using silicon photomultiplier. Milan, Italy: The Polytechnic University of Milan; 2015.

[40] Knoll GF. Radiation detection and measurement: 3rd edition. New York: Wiley; 1999.

[41] Lilley J. Nuclear Physics, Principle and Applications: 1st ed. John Wiley & Sons, Ltd; 2001.

[42] Brooks FD. Development of organic scintillators. Nuclear Instruments and Methods. 1979;162(1):477-505.

[43] Seco J, Clasie B, Partridge M. Review on the characteristics of radiation detectors for dosimetry and imaging. Phys Med Biol. 2014;59(20):R303-47.

[44] Yanagida T. Inorganic scintillating materials and scintillation detectors. Proceedings of the Japan Academy Series B, Physical and biological sciences. 2018;94(2):75-97.

[45] Derenzo SE, Weber MJ, Bourret-Courchesne E, Klintenberg MK. The quest for the ideal inorganic scintillator. Nuclear Instruments and Methods in Physics Research Section A: Accelerators, Spectrometers, Detectors and Associated Equipment. 2003;505(1):111-7.

[46] Lecoq P. Development of new scintillators for medical applications. Nuclear Instruments and Methods in Physics Research Section A: Accelerators, Spectrometers, Detectors and Associated Equipment. 2016;809:130-9.

[47] Michail CM, Fountos GP, Liaparinos PF, Kalyvas NE, Valais I, Kandarakis IS, et al. Light emission efficiency and imaging performance of $Gd_2\ O_2$ S: Eu powder scintillator under x-ray radiography conditions. Med Phys. 2010;37(7):3694-703.

[48] Gorokhova E, Rodnyi P, Anan'eva G, Demidenko V, Eron'ko S, Oreshchenko E, et al. Scintillation optical ceramics based on Gd2O2S doped with Pr, Tb, or Eu. Journal of Optical Technology. 2012;79.

[49] Yanagida T, Kamada K, Fujimoto Y, Yagi H, Yanagitani T. Comparative study of ceramic and single crystal Ce:GAGG scintillator. Optical Materials. 2013;35(12):2480-5.

[50] Zalipska J, Balcerzyk M, Kapusta M, Mengesha W, Valentine JD. Intrinsic energy resolution of NaI(Tl)11Support for this work was provided by the

Polish Committee for Scientific Research, Grant No 8 T10C 002 20. Nuclear Instruments and Methods in Physics Research Section A: Accelerators, Spectrometers, Detectors and Associated Equipment. 2002;484(1):259-69.

[51] Klanner R. Silicon detectors. Nuclear Instruments and Methods in Physics Research Section A: Accelerators, Spectrometers, Detectors and Associated Equipment. 1985;235(2):209-215.

[52] Lesser M. Charge coupled device (CCD) image sensors. In: Durini D, editor. High Performance Silicon Imaging: Woodhead Publishing; 2014. p. 78-97.

[53] Janesick JR, Elliott T, Collins S, Blouke MM, Freeman J, editors. Scientific Charge-Coupled Devices 1987: SPIE.

[54] Garnir HP, LefÃšbvre PH. Quantum efficiency of back-illuminated CCD detectors in the VUV region (30–200nm). Nuclear Instruments and Methods in Physics Research Section B: Beam Interactions with Materials and Atoms. 2005;235(1):530-540

[55] Robbins MS, Hadwen BJ. The noise performance of electron multiplying charge-coupled devices. IEEE Transactions on Electron Devices. 2003;50(5):1227-1232.

[56] Bigas M, Cabruja E, Forest J, Salvi J. Review of CMOS image sensors. 2006;37(5):433-51.

[57] Hillebrand M, Stevanovic N, Hosticka BJ, Conde JES, Teuner A, Schwarz M, editors. High speed camera system using a CMOS image sensor. Proceedings of the IEEE Intelligent Vehicles Symposium 2000 (Cat No00TH8511); 2000 5-5 Oct. 2000.

[58] Evans DA, Allport PP, Casse G, Faruqi AR, Gallop B, Henderson R, et al. CMOS active pixel sensors for ionising radiation. Nuclear Instruments and Methods in Physics Research Section A: Accelerators, Spectrometers, Detectors and Associated Equipment. 2005;546(1):281-5.

[59] Janesick JR, editor Charge-coupled CMOS and hybrid detector arrays. Optical Science and Technology, SPIE's 48th Annual Meeting; 2004: SPIE.

[60] Sze M, Ng K. Physics of Semiconductor Devices: 3rd edition. Wiley-Interscience; 2006.

[61] Neamen D. Semiconductor Physics And Devices: McGraw-Hill, Inc.; 2003.

[62] Dummer GWA. Electronic Inventions and Discoveries: Electronics from Its Earliest Beginnings to the Present Day: Elsevier Science; 2013.

[63] Barbarino G, Asmundis R, De Rosa G, Mollo CM, Russo S, Vivolo D. Silicon Photo Multipliers Detectors Operating in Geiger Regime: an Unlimited Device for Future Applications. 2011.

[64] Dinu N. Silicon photomultipliers (SiPM). In: Nabet B, editor. Photodetectors: Woodhead Publishing; 2016. p. 255-94.

[65] Ikagawa T, Kataoka J, Yatsu Y, Saito T, Kuramoto Y, Kawai N, et al. Study of large area Hamamatsu avalanche photodiode in a γ-ray scintillation detector. Nuclear Instruments and Methods in Physics Research Section A: Accelerators, Spectrometers, Detectors and Associated Equipment. 2005;538(1):640-50.

[66] Renker D. Geiger-mode avalanche photodiodes, history, properties and problems. Nuclear Instruments and Methods in Physics Research Section A: Accelerators, Spectrometers, Detectors and Associated Equipment. 2006;567(1):48-56.

[67] Ghassemi A, Sato K, Kobayashi K. Hamamatsu Technical Note 2017.

[68] Buzhan P, Dolgoshein B, Ilyin A, Kantserov V, Kaplin V, Karakash A, et al. The Advanced Study of Silicon Photomultiplier. Advanced Technology and Particle Physics. Astroparticle, Particle, Space Physics, Radiation Interaction, Detectors and Medical Physics Applications. Volume 1: WORLD SCIENTIFIC; 2002. p. 717-28.

[69] Buzhan P, Dolgoshein B, Filatov L, Ilyin A, Kantzerov V, Kaplin V, et al. Silicon photomultiplier and its possible applications. Nuclear Instruments and Methods in Physics Research Section A: Accelerators, Spectrometers, Detectors and Associated Equipment. 2003;504(1):48-52.

[70] Vinogradov S. The Silicon Photomultiplier (SiPM) Concept and Design Development. Astroparticle Physics European Consortium. 2020 [Available from: https://www.appec.org/news/the-silicon-photomultiplier-sipm-concept-and-design-development].

[71] Eckert P, Schultz-Coulon H-C, Shen W, Stamen R, Tadday A. Characterisation studies of silicon photomultipliers. Nuclear Instruments and Methods in Physics Research Section A: Accelerators, Spectrometers, Detectors and Associated Equipment. 2010;620(2):217-26.

[72] Piemonte C. A new Silicon Photomultiplier structure for blue light detection. Nuclear Instruments and Methods in Physics Research Section A: Accelerators, Spectrometers, Detectors and Associated Equipment. 2006;568(1):224-232.

[73] Gulinatti A, Rech I, Zappa F, Cova S. Progress in Silicon Single-Photon Avalanche Diodes. IEEE Journal of Selected Topics in Quantum Electronics. 2007;13(4):852-862.

[74] Ward MA, and Vacheret A. Impact of after-pulse, pixel crosstalk and recovery time in multi-pixel photon counter response. Nuclear Instruments and Methods in Physics Research. 2009;610, 370-373.

[75] Rosado J, Hidalgo S. Characterization and modelling of crosstalk and afterpulsing in Hamamatsu silicon photomultipliers. 2015.

[76] Dowsett D, Kenny P, Johnston R. The Physics of Diagnostic Imaging. London: CRC Press; 2006.

[77] Khalil MM, Tremoleda JL, Bayomy TB, Gsell W. Molecular SPECT Imaging: An Overview. Int J Mol Imaging. 2011;2011:796025.

[78] Histed SN, Lindenberg ML, Mena E, Turkbey B, Choyke PL, Kurdziel KA. Review of functional/anatomical imaging in oncology. Nucl Med Commun. 2012;33(4):349-61.

[79] Shefer E, Altman A, Behling R, Goshen R, Gregorian L, Roterman Y, et al. State of the Art of CT Detectors and Sources: A Literature Review. Current Radiology Reports. 2013;1(1):76-91.

[80] Ladd ME, Bachert P, Meyerspeer M, Moser E, Nagel AM, Norris DG, et al. Pros and cons of ultra-high-field MRI/MRS for human application. Progress in Nuclear Magnetic Resonance Spectroscopy. 2018;109:1-50.

[81] Abu-Zidan FM, Hefny AF, Corr P. Clinical ultrasound physics. J Emerg Trauma Shock. 2011;4(4):501-3.

[82] Carovac A, Smajlovic F, Junuzovic D. Application of ultrasound in medicine. Acta Inform Med. 2011;19(3):168-71.

[83] Rahmim A, Zaidi H. PET versus SPECT: strengths, limitations and challenges. Nucl Med Commun. 2008;29(3):193-207.

[84] Vassaux G, Groot-Wassink T. In Vivo Noninvasive Imaging for Gene Therapy. J Biomed Biotechnol. 2003;2003(2):92-101.

[85] Pauleit D, Floeth F, Tellmann L, Hamacher K, Hautzel H, MÃŒller H-W, et al. Comparison of O-(2-18F-fluoroethyl)-L-tyrosine PET and 3- 123I-iodo-α-methyl-L-tyrosine SPECT in brain tumors.

[86] Jolesz F. Intraoperative Imaging and Image-Guided Therapy. Springer; 2014.

[87] van Velthoven V. Intraoperative ultrasound imaging: comparison of pathomorphological findings in US versus CT, MRI and intraoperative findings. Acta Neurochir Suppl. 2003;85:95-9.

[88] Sipos EP, Heisey J. Intraoperative CT Scanner Combined With Image-Guided Neurosurgery. Journal of Radiology Nursing. 2015;34(2):73-9.

[89] Gandhe RU, Bhave CP. Intraoperative magnetic resonance imaging for neurosurgery - An anaesthesiologist's challenge. Indian J Anaesth. 2018;62(6):411-7.

[90] Hoffman EJ, Tornai MP, Janecek M, Patt BE, Iwanczyk JS. Intraoperative probes and imaging probes. Eur J Nucl Med. 1999;26(8):913-35.

[91] Povoski SP, Neff RL, Mojzisik CM, O'Malley DM, Hinkle GH, Hall NC, et al. A comprehensive overview of radioguided surgery using gamma detection probe technology. World J Surg Oncol. 2009;7.

[92] Kopelman D, Blevis I, Iosilevsky G, Hatoum OA, Zaretzki A, Shofti R, et al. Sentinel node detection in an animal study: evaluation of a new portable gamma camera. International surgery. 2007;92(3):161-6.

[93] Sarikaya I, Sarikaya A, Reba RC. Gamma probes and their use in tumor detection in colorectal cancer. International seminars in surgical oncology: ISSO. 2008;5:25.Tsuchimochi M, Hayama K, Oda T, Togashi M, Sakahara H. Evaluation of the efficacy of a small CdTe gamma-camera for sentinel lymph node biopsy. J Nucl Med. 2008;49(6):956-62.

[94] Tsuchimochi M, Hayama K, Oda T, Togashi M, Sakahara H. Evaluation of the efficacy of a small CdTe gamma-camera for sentinel lymph node biopsy. J Nucl Med. 2008;49(6):956-62.

[95] Mammatome. Neoprobe Gamma Detection System 2017 [Available from: https://www.mammotome.com/neoprobe/].

[96] Zamburlini M, Keymeulen K, Bemelmans M, Brans B, Kemerink GJ. Comparison of sentinel gamma probes for 99mTc breast cancer surgery based on NEMA NU3-2004 standard. Nucl Med Commun. 2009;30(11):854-61.Medico D.

[97] Kaviani S, Zeraatkar N, Sajedi S, Gorjizadeh N, Farahani MH, Ghafarian P, et al. Development and characterization of a compact hand-held gamma probe system, SURGEOGUIDE, based on NEMA NU3-2004 standards. Journal of Instrumentation. 2016;11(12):T12004-T.

[98] Faxitron TruNode 2019 [Available from: https://datecmedico.dk/en/products/item/tr].

[99] Itikawa EN, Santos LA, Trevisan AC, Pitella FA, Kato M, Moraes ER, et al. Characterization of resolution, sensitivity, and shielding of a gamma-probe for sentinel lymph node localization: an experimental study. Nucl Med Commun. 2017;38(10):837-42.

[100] Burak WE, Agnese DM, Povoski SP. Advances in the surgical management of early stage invasive breast cancer. Curr Probl Surg. 2004;41:877–936.

[101] Krag DN, Weaver DL, Alex JC, Fairbank JT. Surgical resection and radiolocalization of the sentinel lymph node in breast cancer using a gamma probe. Surg Oncol. 1993;2:335–339. discussion 340.

[102] Carrera D, Fernandez A, Estrada J, Martin-Comin J, Gamez C. Detection of occult malignant melanoma by 18F-FDG PET-CT and gamma probe, Rev Esp Med Nucl. 2005;24:410–413.

[103] Delgado ML, Busam K, Cody HS, 3rd, Athanasian EA, Coit D, La Quaglia MP. Experience with 31 sentinel lymph node biopsies for sarcomas and carcinomas in pediatric patients. Cancer. 2008;112:2052–2059.

[104] Michl C, Starz H, Bachter D, Balda BR. Sentinel lymphonodectomy in nonmelanoma skin malignancies. Br J Dermatol. 2003;149:763–769.

[105] Filho O, Carneiro Filho O. Gamma probe-assisted brain tumor microsurgical resection: a new technique. Arq Neuropsiquiatr. 2002;60:1042–1047.

[106] De Boeck H, Casteleyn PP, Bossuyt A, Jacobs A. Intraoperative radioactive localization of small bone tumours. Int Orthop.

[107] Bembenek A, Gretschel S, Schlag PM. Sentinel lymph node biopsy for gastrointestinal cancers. J Surg Oncol. 2007;96:342–352.

[108] Kovacs AF, Landes CA, Hamscho N, Risse JH, Berner U, Menzel C. Sentinel node biopsy as staging tool in a multi-modality treatment approach to cancer of the oral cavity and oropharynx. Otolaryngol Head Neck Sug. 2005;132:570–576.

[109] Schmidt FE, Woltering EA, Webb WR, Garcia OM, Cohen JE, Rozans MH. Sentinel nodal assessment in patients with carcinoma of the lung. Ann Thorac Surg. 2002;74:870–874. discussion 874–875.

[110] Loar PV, 3rd, Reynolds RK. Sentinel lymph node mapping in gynecologic malignancies. Int J Gynaecol Obstet. 2007;99:69–74.

[111] Fowler JE Jr. Sentinel lymph node biopsy for staging penile cancer. Urology. 1984;23:352–353.

[112] Goyal A, Newcombe RG, Mansel RE, Chetty U, Ell P, Fallowfield L, et al. Role of routine preoperative lymphoscintigraphy in sentinel node biopsy for breast cancer. European journal of cancer. 2005;41(2):238-43.

[113] Seddon B, Cook A, Gothard L, Salmon E, Latus K, Underwood SR, et al. Detection of defects in myocardial perfusion imaging in patients with early breast cancer treated with radiotherapy. Radiother Oncol. 2002;64(1):53-63.

[114] Heller S, Zanzonico P. Nuclear probes and intraoperative gamma cameras. Seminars in nuclear medicine. 2011;41(3):166-81. Britten AJ. A method to evaluate intra-operative gamma probes for sentinel lymph node localisation. European Journal of Nuclear Medicine. 1999;26(2):8.

[115] Kopelman D, Blevis I, Iosilevsky G, Hatoum OA, Zaretzki A, Shofti R, et al. Sentinel node detection in an animal study: evaluation of a new portable gamma camera. International surgery. 2007;92(3):161-6.

[116] Tsuchimochi M, Hayama K. Intraoperative gamma cameras for radioguided surgery: technical characteristics, performance parameters, and clinical applications. Phys Med. 2013;29(2):126-38.

[117] Hellingman D, Vidal-Sicart S. The Use of Intraoperative Small and Large Field of View Gamma Cameras for Radioguided Surgery. 2016. p. 35-56.

[118] Tsuchimochi M, Hayama K, Oda T, Togashi M, Sakahara H. Evaluation of the efficacy of a small CdTe gamma-camera for sentinel lymph node biopsy. J Nucl Med. 2008;49(6):956-62.

[119] Oncovision. Sentinella 2019 [Available from: https://www.oncovision.com/sentinella/].

[120] Rietbergen D, Van den Berg N, Leeuwen FWB, Olmos R. Hybrid techniques for intraoperative sentinel lymph node imaging: Early experiences and future prospects. Imaging in Medicine. 2013;5:147-59.

[121] Crystal Photonics. Handheld USB-Gamma Camera "CrystalCam" 2018 [Available from: https://crystal-photonics.com/enu/products/cam-crystalcam--enu.htm].

[122] Sånchez F, Benlloch JM, Escat B, Pavon N, Porras E, Kadi-Hanifi D, et al. Design and tests of a portable mini gamma camera. Medical physics. 2004;31(6):1384-97.

[123] Ozkan E, Eroglu A. The Utility of Intraoperative Handheld Gamma Camera for Detection of Sentinel Lymph Nodes in Melanoma. Nucl Med Mol Imaging. 2015;49(4):318-20. 12.

[124] Zuhayra M, Dierck S, Marx M, Zhao Y, Wilhelm R, Assam I, LÃŒtzen U. Is the portable gamma camera" Crystal Cam" equal to the conventional gamma camera for the detection of SLNs of malignant melanoma. Journal of Nuclear Medicine. 2015 May 1;56(supplement 3):1866.

[125] Crystal Photonics. Clinical cases CrystalCam; A comparison of SPECT/CT (and standard gamma camera) and CrystalCam. 2015 [Available from: https://jrtassociates.com/crystalcamhandheldgammacamera.aspx].

[126] Abe A, Takahashi N, Lee J, Oka T, Shizukuishi K, Kikuchi T, Inoue T, Jimbo M, Ryuo H, Bickel C. Performance evaluation of a hand-held, semiconductor (CdZnTe)-based gamma camera. Eur J Nucl Med Mol Imaging. 2003 Jun;30(6):805-11. doi: 10.1007/s00259-002-1067-z. Epub 2003 Apr 3. PMID: 12677308.

[127] Kopelman D, Blevis I, Iosilevsky G, Hatoum OA, Zaretzki A, Shofti R, Salmon T, Israel O, Hashmonai M. Sentinel node detection in an animal study: evaluation of a new portable gamma camera. Int Surg. 2007 May-Jun;92(3):161-6. PMID: 17972472.

[128] Russo P, Mettivier G, Pani R, Pellegrini R, Cinti MN, Bennati P. Imaging performance comparison between a LaBr3: Ce scintillator based and a CdTe semiconductor based photon counting compact gamma camera. Med Phys. 2009 Apr;36(4):1298-317. doi: 10.1118/1.3081412. PMID: 19472638.

[129] Oda T, Hayama K, Tsuchimochi M. [Evaluation of small semiconductor gamma camera–simulation of sentinel lymph node biopsy by using a trial product of clinical type gamma camera]. Kaku Igaku. 2009 Mar;46(1):1-12. Japanese. PMID: 19413190.

[130] Goertzen AL, Thiessen JD, McIntosh B, Simpson MJ, and Schellenberg J. 2013. Characterization of a handheld gamma camera for intraoperative use for sentinel lymph node biopsy. in IEEE Nuclear Science Symposium Conference Record.

[131] Fujii T, Yamaguchi S, Yajima R, Tsutsumi S, Uchida N, Asao T, Oriuch N, Kuwano H. Use of a handheld, semiconductor (cadmium zinc telluride)-based gamma camera in navigation surgery for primary hyperparathyroidism. Am Surg. 2011 Jun;77(6):690-3. PMID: 21679634.

[132] Mathelin C, Salvador S, Bekaert V, Croce S, Andriamisandratsoa N, LiÃ©geois P, Prados E, Guyonnet JL, Grucker D, Brasse D. A new intraoperative gamma camera for the sentinel lymph node procedure in breast cancer. Anticancer Res. 2008 Sep-Oct;28(5B):2859-64. PMID: 19031925.

[133] Aarsvod JN, Greene CM, Mintzer RA, Grant SF, Styblo TM, Alazraki NP, et al. Intraoperative gamma imaging of axillary sentinel lymph nodes in breast cancer patients. Phys Med. 2006;21 Suppl 1:76-9.

[134] McAreavey LH, Harkness-Brennan LJ, Colosimo SJ, Judson DS, Boston AJ. 2017. Characterisation of a CZT detector for dosimetry of molecular radiotherapy. Journal of Instrumentation, 12(03): P03001.

[135] Ferretti A, Chondrogiannis S, Marcolongo A, Rubello D. Phantom study of a new hand-held g-imaging probe for radio-guided surgery. Nucl Med Commun. 2013;34(1):86-90.

[136] Olcott P, Pratx G, Johnson D, Mittra E, Niederkohr R, Levin CS. Clinical evaluation of a novel intraoperative handheld gamma camera for sentinel lymph node biopsy. Phys Med. 2014 May;30(3):340-5. doi: 10.1016/j.ejmp.2013.10.005. Epub 2013 Nov 14. PMID: 24239343.

[137] Netter E, Pinot L, Menard L, Duval MA, Janvier B, Lefebvre F, et al. The Tumor Resection Camera (TReCam), a multipixel imaging probe for radio-guided surgery. IEEE Nuclear Science Symposium Conference Record (NSS/MIC) 2009:2573-6.

[138] James ML, Gambhir SS. A Molecular Imaging Primer: Modalities, Imaging Agents, and Applications. Physiological Reviews. 2012;92(2):897- 965.

[139] Weissleder R, Pittet MJ. Imaging in the era of molecular oncology. Nature. 2008;452(7187):580-9.

[140] Arridge SR. Optical tomography in medical imaging. Inverse Problems. 1999;15(2):R41-R93.

[141] de Boer E, Harlaar NJ, Taruttis A, Nagengast WB, Rosenthal EL, Ntziachristos V, et al. Optical innovations in surgery. Br J Surg. 2015;102(2):e56-72.

[142] Kriss TC, Kriss VM. History of the operating microscope: from magnifying glass to microneurosurgery. Neurosurgery. 1998;42(4):899-907; discussion -8.

[143] Schmitt JM, Knuttel A, Yadlowsky M, Eckhaus MA. Optical-coherence tomography of a dense tissue: statistics of attenuation and backscattering. Phys Med Biol. 1994;39(10):1705-20.

[144] Fujimoto JG, Pitris C, Boppart SA, Brezinski ME. Optical coherence tomography: an emerging technology for biomedical imaging and optical biopsy. Neoplasia. 2000;2(1-2):9-25.

[145] Fujisawa Y, Nakamura Y, Kawachi Y, Otsuka F. Indocyanine green fluorescence-navigated sentinel node biopsy showed higher sensitivity than the radioisotope or blue dye method, which may help to reduce false-negative cases in skin cancer. Journal of Surgical Oncology. 2012;106(1):41-50.

[146] Badr CE, Tannous BA. Bioluminescence imaging: progress and applications. Trends Biotechnol. 2011;29(12):624-33.

[147] Sadikot RT, Blackwell TS. Bioluminescence imaging. Proc Am Thorac Soc. 2005;2(6):537-12.

[148] Liu H, Carpenter CM, Jiang H, Pratx G, Sun C, Buchin MP, et al. Intraoperative imaging of tumors using Cerenkov luminescence endoscopy: a feasibility experimental study. Journal of nuclear medicine : official publication, Society of Nuclear Medicine. 2012;53(10):1579-84.

[149] Holland JP, Normand G, Ruggiero A, Lewis JS, Grimm J. Intraoperative Imaging of Positron Emission Tomographic Radiotracers Using Cerenkov Luminescence Emissions. Molecular Imaging. 2011;10(3):7290.2010.00047.

[150] Liu, J. Two-photon microscopy in pre-clinical and clinical cancer research. Front. Optoelectron. 8, 141–151 (2015). https://doi.org/10.1007/s12200-014-0415-5.

[151] Haka AS, Volynskaya Z, Gardecki JA, Nazemi J, Lyons J, Hicks D, Fitzmaurice M, Dasari RR, Crowe JP, Feld MS. In vivo margin assessment during partial mastectomy breast surgery using raman spectroscopy. Cancer Res. 2006 Mar 15;66(6):3317-22. doi: 10.1158/0008-5472.CAN-05-2815. PMID: 16540686.

[152] Wachsmann-Hogiu S, Weeks T, Huser T. Chemical analysis in vivo and in vitro by Raman spectroscopy-from single cells to humans. Current Opinion in Biotechnology. 2009;20(1):63-73.

[153] Eggebrecht AT, Ferradal SL, Robichaux-Viehoever A, Hassanpour MS, Dehghani H, Snyder AZ, Hershey T, Culver JP. Mapping distributed brain function and networks with diffuse optical tomography. Nat Photonics. 2014 Jun;8(6):448-454. doi: 10.1038/nphoton.2014.107. PMID: 25083161; PMCID: PMC4114252.

[154] Allen TJ, Hall A, Dhillon AP, Owen JS, Beard PC. Spectroscopic photoacoustic imaging of lipid-rich plaques in the human aorta in the 740 to 1400 nm wavelength range. J Biomed Opt. 2012 Jun;17(6):061209. doi: 10.1117/1.JBO.17.6.061209. PMID: 22734739.

[155] Oscar MG, Cecilia Spagnuolo C. Basic Concepts of Fluorescence and Fluorescent Probes. 2015; 3-18.

[156] Gioux S, Choi HS, Frangioni JV. Image-guided surgery using invisible near-infrared light: fundamentals of clinical translation. Mol Imaging. 2010;9(5):237-255.

[157] Ballardini B, Santoro L, Sangalli C, Gentilini O, Renne G, Lissidini G. The indocyanine green method is equivalent to the ^{99m}Tc-labeled radiotracer method for identifying the sentinel node in breast cancer: A concordance and validation study. European Journal of Surgical Oncology (EJSO). 2013;39(12):1332-1346.

[158] Luo S, Zhang E, Su Y, Cheng T, Shi C. A review of NIR dyes in cancer targeting and imaging. Biomaterials. 2011;32(29):7127-7138.

[159] Biosciences L. IRDye 800CW. [Internet]. Licor.com. 2018 [cited 5 February 2018]. Available from: https://www.licor.com/bio/products/reagents/irdye/800cw/.

[160] Jolesz FA, editor. Intraoperative Imaging and Image-Guided Therapy 1ed: Springer Science+Business Media New York; 2014.

[161] Marshall MV, Draney D, Sevick-Muraca EM, Olive DM. Single-Dose Intravenous Toxicity Study of IRDye 800CW in Sprague-Dawley Rats. Molecular Imaging and Biology. 2010;12(6):583-594.

[162] Sjoback R, Nygren J, Kubista M. Absorption and fluorescence properties of fluorescein. Spectrochimica Acta Part A: Molecular and Biomolecular Spectroscopy. 1995;51(6):L7-L21.

[163] Philip R, Penzkofer A, BÃ€umler W, Szeimies RM, Abels C. Absorption and fluorescence spectroscopic investigation of indocyanine green. Journal of Photochemistry and Photobiology A: Chemistry. 1996;96(1):137-48.

[164] Tuite EM, Kelly JM. Photochemical interactions of methylene blue and analogues with DNA and other biological substrates. J Photochem Photobiol B. 1993 Dec;21(2-3):103-24. doi: 10.1016/1011-1344(93)80173-7. PMID: 8301408.

[165] Azhdarinia A, Wilganowski N, Robinson H, Ghosh P, Kwon S, Lazard ZW, Davis AR, Olmsted-Davis E, Sevick-Muraca EM. Characterization of chemical, radiochemical and optical properties of a dual-labeled MMP-9 targeting peptide. Bioorg Med Chem. 2011 Jun 15;19(12):3769-76. doi: 10.1016/j.bmc.2011.04.054. Epub 2011 May 6. PMID: 21612930; PMCID: PMC3148023.

[166] Umezawa K, Matsui A, Nakamura Y, Citterio D, Suzuki K. Bright, color-tunable fluorescent dyes in the Vis/NIR region: establishment of new "tailor-made" multicolor fluorophores based on borondipyrromethene. Chemistry. 2009;15(5):1096-106. doi: 10.1002/chem.200801906. PMID: 19117043.

[167] Orosco RK, Tsien RY, Nguyen QT. Fluorescence Imaging in Surgery. IEEE reviews in biomedical engineering. 2013;6:178-187.

[168] Dsouza AV, Lin H, Henderson ER, Samkoe KS, Pogue BW. Review of fluorescence guided surgery systems: identification of key performance capabilities beyond indocyanine green imaging. J. Biomed. Opt. 2016;21:080901.

[169] Garcia M, Edmiston C, York T, Marinov R, Mondal S, Zhu N, et al. Bio-inspired imager improves sensitivity in near-infrared fluorescence image-guided surgery. Optica. 2018;5(4):413-22

[170] van Driel PB, van de Giessen M, Boonstra MC, Snoeks TJ, Keereweer S, Oliveira S, van de Velde CJ, Lelieveldt BP, Vahrmeijer AL, Lowik CW, Dijkstra J. Characterization and evaluation of the artemis camera for fluorescence-guided cancer surgery. Mol Imaging Biol. 2015 Jun;17(3):413-23. doi: 10.1007/s11307-014-0799-z. PMID: 25344146; PMCID: PMC4422838.

[171] Marti-Bonmati L, Sopena R, Bartumeus P, Sopena P. Multimodality imaging techniques. Contrast Media & Molecular Imaging. 2010;5(4):180-9.

[172] Boss A, Bisdas S, Kolb A, Hofmann M, Ernemann U, Claussen CD, et al. Hybrid PET/MRI of intracranial masses: initial experiences and comparison to PET/CT. J Nucl Med. 2010;51(8):1198-205.

[173] Trifiro G, Viale G, Gentilini O, Travaini LL, Paganelli G. Sentinel node detection in pre-operative axillary staging. Eur J Nucl Med Mol Imaging. 2004 Jun;31 Suppl 1:S46-55. doi: 10.1007/s00259-004-1526-9. Epub 2004 Apr 22. PMID: 15103506.

[174] Hsueh E. Melanoma : Sentinel Lymph Node Biopsy 2020 [cited 2020. Available from: https://www.webpathology.com/image.asp?case=1025&n=42].

[175] Lees JE, Bassford D, Fraser GW, Monk D, Early M, Ott RJ, et al. Investigation of scintillator coated CCDs for medical imaging. IEEE Transactions on Nuclear Science. 2006;53(1):9-13.

[176] Bugby SL. Development of a hybrid portable medical gamma camera. Leicester, UK: University of Leicester; 2015.

[177] Alqahtani MS. Assessment of a novel small field of view medical hybrid gamma camera. Leicester, UK: University of Leicester; 2017.

[178] Lees JE, Bassford DJ, Blake OE, Blackshaw PE, Perkins AC. A high resolution Small Field Of View (SFOV) gamma camera: a columnar scintillator coated CCD imager for medical applications. Journal of Instrumentation. 2011;6(12):C12033-C.

[179] Lees JE, Bassford DJ, Blake OE, Blackshaw PE, Perkins AC. A Hybrid Camera for simultaneous imaging of gamma and optical photons. Journal of Instrumentation. 2012;7(06):P06009-P.

[180] Bugby SL, Lees JE, Bhatia BS, Perkins AC. Characterisation of a high resolution small field of view portable gamma camera. Phys Med. 2014;30(3):331-9.

[181] Alqahtani MS, Lees JE, Bugby SL, Jambi LK, Perkins AC. Lymphoscintigraphic imaging study for quantitative evaluation of a small field of view (SFOV) gamma camera. Journal of Instrumentation. 2015;10(07):P07011-P.

[182] Alqahtani MS, Lees JE, Bugby SL, Samara-Ratna P, Ng AH, Perkins AC. Design and implementation of a prototype head and neck phantom for the performance evaluation of gamma imaging systems. EJNMMI Phys. 2017 Dec;4(1):19. doi: 10.1186/s40658-017-0186-3. Epub 2017 Jul 6. PMID: 28685477; PMCID: PMC5500602.

[183] Bugby SL, Lees JE, Ng AH, Alqahtani MS, Perkins AC. Investigation of an SFOV hybrid gamma camera for thyroid imaging. Phys Med. 2016;32(1):290-6.

[184] Lees JE, Bugby SL, Alqahtani MS, Jambi LK, Dawood NS, McKnight WR, et al. A Multimodality Hybrid Gamma-Optical Camera for Intraoperative Imaging. Sensors (Basel). 2017;17(3).

[185] Pogue BW, Patterson MS. Review of tissue simulating phantoms for optical spectroscopy, imaging and dosimetry. J Biomed Opt. 2006;11(4):041102.

[186] Berg R, Andersson-Engels S, Jarlman O and Svanberg S. Time-gated viewing studies on tissuelike phantoms Appl. Opt. 1996; 35 3432–40.

[187] Jiang S, Pogue BW, McBride TO and Paulsen KD. Quantitative analysis of near-infrared tomography: sensitivity to the tissue-simulating precalibration phantom J. Biomed. Opt. 2003;8 308–15

[188] Srinivasan R, Kumar D and Singh M. Optical tissue-equivalent phantoms for medical imaging Trends Biomater. Artif. Organs 2002; 15 42–7.

[189] Cubeddu R, Pifferi A, Taroni P, Torricelli A and Valentini G. A solid tissue phantom for photon migration studies Phys. Med. Biol. 1997;42 1971–9.

[190] De Grand AM, Lomnes SJ, Lee DS, Pietrzykowski M, Ohnishi S, Morgan T G, Gogbashian A, Laurence R G and Frangioni. Tissue-like phantoms for near-infrared fluorescence imaging system assessment and the training of surgeons J. Biomed. Opt. 2006;11 014007.

[191] Firbank M and Delpy DT. A design of a stable and reproducible phantom for use in near infrared imaging and spectroscopy Phys. Med. Biol. 1993;38 847–53.

[192] Sukowski U, Schubert F, Grosenick D and Rinneberg H. Preparation of solid phantoms with defined scattering and absorption properties for optical tomography Phys. Med. Biol. 1996; 41 1823–44.

[193] Hebden JC, Price BD, Gibson AP, Royle G. A soft deformable tissue-equivalent phantom for diffuse optical tomography. Physics in Medicine and Biology. 2006;51(21):5581-90.

[194] Lualdi M, Colombo A, Farina B, Tomatis S, Marchesini R. A phantom with tissue-like optical properties in the visible and near infrared for use in photomedicine. Lasers Surg Med. 2001;28(3):237-43.

[195] Dempsey LA, Persad M, Powell S, Chitnis D, Hebden JC. Geometrically complex 3D-printed phantoms for diffuse optical imaging. Biomed Opt Express. 2017;8(3):1754-62.

[196] Larsson J, Liao P, Lundin P, Krite Svanberg E, Swartling J, Lewander Xu M, et al. Development of a 3-dimensional tissue lung phantom of a preterm infant for optical measurements of oxygen—Laser-detector position considerations. Journal of Biophotonics. 2018;11(3):e201700097.

[197] Demos SG, Radousky HB, Alfano RR. Deep subsurface imaging in tissues using spectral and polarization filtering. Opt Express. 2000;7(1):23-8.

[198] Cheong WF, Prahl SA, Welch AJ. A review of the optical properties of biological tissues. IEEE Journal of Quantum Electronics. 1990;26(12):2166-85.

[199] Jaeger M, Preisser S, Kitz M, Ferrara D, Senegas S, Schweizer D, et al. Improved contrast deep optoacoustic imaging using displacement-compensated averaging: breast tumour phantom studies. Physics in Medicine and Biology. 2011;56(18):5889-901.

[200] Pleijhuis RG, Langhout GC, Helfrich W, Themelis G, Sarantopoulos A, Crane LMA, et al. Near-infrared fluorescence (NIRF) imaging in breast-conserving surgery: Assessing intraoperative techniques in tissue-simulating breast phantoms. European Journal of Surgical Oncology (EJSO). 2011;37(1):32-9.

[201] Anastasopoulou M, Koch M, Gorpas D, Karlas A, Klemm U, Garcia-Allende PB, et al. Comprehensive phantom for interventional fluorescence molecular imaging. Journal of Biomedical Optics. 2016;21(9):091309.

[202] Howlader N, Noone AM, Krapcho M, Miller D, Brest A, Yu M, Ruhl J, Tatalovich Z, Mariotto A, Lewis DR, Chen HS, Feuer EJ, Cronin KA

(eds). SEER Cancer Statistics Review, 1975-2016, National Cancer Institute. Bethesda, MD, https://seer.cancer.gov/csr/1975_2016/, based on November 2018 SEER data submission, posted to the SEER web site, April 2019

[203] Alander JT, Kaartinen I, Laakso A, Patila T, Spillmann T, Tuchin VV, et al. A review of indocyanine green fluorescent imaging in surgery. Int J Biomed Imaging. 2012;2012:940585.

[204] Murawa D, Hirche C, Dresel S, HÃŒnerbein M. Sentinel lymph node biopsy in breast cancer guided by indocyanine green fluorescence. BJS (British Journal of Surgery). 2009;96(11):1289-94.

[205] Hojo T, Nagao T, Kikuyama M, Akashi S, Kinoshita T. Evaluation of sentinel node biopsy by combined fluorescent and dye method and lymph flow for breast cancer. The Breast. 2010;19(3):210-3.

[206] Alford R, Simpson HM, Duberman J, Hill GC, Ogawa M, Regino C, et al. Toxicity of Organic Fluorophores Used in Molecular Imaging: Literature Review. Molecular Imaging. 2009;8(6):7290.2009.00031.

[207] Hamamatsu, PDE Near Infrared Fluorescence Imager, https://www.selectscience.net/products/pde-neo-ii-near-infrared-fluorescence-imager/?prodID=206439. 2019.

[208] Gurtner GC, Jones GE, Neligan PC, Newman MI, Phillips BT, Sacks JM, et al. Intraoperative laser angiography using the SPY system: review of the literature and recommendations for use. Annals of Surgical Innovation and Research. 2013;7(1):1.

[209] Lee BT, Hutteman M, Gioux S, Stockdale A, Lin SJ, Ngo LH, et al. The FLARE Intraoperative Near-Infrared Fluorescence Imaging System: A First-in-Human Clinical Trial in Perforator Flap Breast Reconstruction. Plastic and Reconstructive Surgery. 2010;126(5):1472-81.

[210] Fluoptics, Fluobeam, https://fluoptics.com/en/fluobeam-us/. 2019.

[211] Biosciences, Pearl Small Animal Imagers for in vivo Optical Imaging Studies, Licor. 2018.

[212] Polom K, Murawa D, Polom W. Re: Henk G. van der Poel, Tessa Buckle, Oscar R. Brouwer, Renato A. ValdÃ©s Olmos, Fijs W.B. van Leeuwen. Intraoperative Laparoscopic Fluorescence Guidance to the Sentinel Lymph Node in Prostate Cancer Patients: Clinical Proof of Concept of an Integrated Functional Imaging Approach Using a Multimodal Tracer. Eur Urol 2011;60:826–33. European Urology. 2012;61(3):e18.

[213] Brouwer OR, Klop WMC, Buckle T, Vermeeren L, van den Brekel MWM, Balm AJM, et al. Feasibility of Sentinel Node Biopsy in Head and Neck Melanoma Using a Hybrid Radioactive and Fluorescent Tracer. Annals of Surgical Oncology. 2012;19(6):1988-94.

[214] van den Berg NS, Brouwer OR, Klop WMC, Karakullukcu B, Zuur CL, Tan IB, et al. Concomitant radio- and fluorescence-guided sentinel lymph node biopsy in squamous cell carcinoma of the oral cavity using ICG-99mTc-nanocolloid. European Journal of Nuclear Medicine and Molecular Imaging. 2012;39(7):1128-36.

[215] Jeschke S, Lusuardi L, Myatt A, Hruby S, Pirich C, Janetschek G. Visualisation of the Lymph Node Pathway in Real Time by Laparoscopic Radioisotope- and Fluorescence-guided Sentinel Lymph Node Dissection in Prostate Cancer Staging. Urology. 2012;80(5):1080-7.

[216] Kang HG, Song SH, Han YB, Lee H-Y, Kim KM, Hong SJ. Proof-of-concept of a multimodal laparoscope for simultaneous NIR/gamma/visible imaging using wavelength division multiplexing. Opt Express. 2018;26(7):8325-39.

[217] Bugby SL, Lees JE, Perkins AC. Modelling image profiles produced with a small field of view gamma camera with a single pinhole collimator. Journal of Instrumentation. 2012;7(11):P11025-P.

[218] Bugby SL, Lees JE, Ng AH, Alqahtani MS, Perkins AC. Investigation of an SFOV hybrid gamma camera for thyroid imaging. Phys Med. 2016;32(1):290-6.

[219] IDS, uEye XS USB mini camera, https://en.ids-imaging.com/store/products/cameras/usb-2-0-cameras/ueye-xs.html. 2017.

[220] IDS, uEye CP USB camera, https://en.ids-imaging.com/usb3-camera-ueye-cp.html?m-layered=1. 2017.

[221] Ferreira T. and W. Rasband, ImageJ User Guide, 2012.

[222] Edmund Optics Ltd. LED Ring Light, Edmund Optics Inc, https://www.edmundoptics.com/. 2018.

[223] Optical filter shop, Near Infrared Bandpass Filter 850nm FWHM 100nm, https://opticalfiltershop.com/shop/bandpass-filter/near-infrared-bandpass-filter-850nm-fwhm-100nm. 2018.

[224] P.S. Composites, T-3 addition-cure silicone, 2018.

[225] Sigma-Aldrich, Aluminium oxide (1344-28-1), 2018.

[226] Max-FactorX, Max Factor CrÃšme Puff Deep Beige, 2018.

[227] Chance B. Near-Infrared Images Using Continuous, Phase-Modulated, and Pulsed Light with Quantitation of Blood and Blood Oxygenationa. Annals of the New York Academy of Sciences. 1998;838(1):29-45. 15.

[228] Weiler M, Kassis T, Dixon JB. Sensitivity analysis of near-infrared functional lymphatic imaging: SPIE; 2012. 16.

[229] Marshall MV, Rasmussen JC, Tan IC, Aldrich MB, Adams KE, Wang X, et al. Near-Infrared Fluorescence Imaging in Humans with Indocyanine Green: A Review and Update. Open Surg Oncol J. 2010;2(2):12-25.

[230] Hwang K, Houston JP, Rasmussen JC, Joshi A, Ke S, Li C, et al. Improved Excitation Light Rejection Enhances Small-Animal Fluorescent Optical Imaging. Molecular Imaging. 2005;4(3):15353500200505142.

[231] Houston JP, Thompson AB, Gurfinkel M, Sevick-Muraca EM. Sensitivity and Depth Penetration of Continuous Wave Versus Frequency-domain Photon Migration Near-infrared Fluorescence Contrast–enhanced Imaging. Photochemistry and Photobiology. 2003;77(4):420-30.

[232] Keereweer S, Van Driel PBAA, Snoeks TJA, Kerrebijn JDF, Baatenburg de Jong RJ, Vahrmeijer AL, et al. Optical Image-Guided Cancer Surgery: Challenges and Limitations. Clinical Cancer Research. 2013;19(14):3745.

[233] Nagarkar VV, Shestakova I, Gaysinskiy V, Singh B, Miller BW, Bradford Barber H. Fast X-ray/γ-ray imaging using electron multiplying CCD-based detector. Nuclear Instruments and Methods in Physics Research Section A: Accelerators, Spectrometers, Detectors and Associated Equipment. 2006;563(1):45-8.

[234] Heemskerk JW, Westra AH, Linotte PM, Ligtvoet KM, Zbijewski W, Beekman FJ. Front-illuminated versus back-illuminated photon-counting CCD-based gamma camera: important consequences for spatial resolution and energy resolution. Phys Med Biol. 2007;52(8):N149-62.

[235] Vree GAd, Westra AH, Moody I, Have Fvd, Ligtvoet KM, Beekman FJ. Photon-counting gamma camera based on an electron-multiplying CCD. IEEE Trans Nucl Sci. 2005;52(3):580-8.

[236] Gruner SM, Tate MW, Eikenberry EF. Charge-coupled device area x-ray detectors. Review of Scientific Instruments. 2002;73(8):2815-42.

[237] Heemskerk J, Korevaar M, Huizenga J, Kreuger R, Schaart D, Goorden M, et al. An enhanced high-resolution EMCCD-based gamma camera using SiPM side detection. Physics in medicine and biology. 2010;55:6773-84.

[238] Roncali E, Cherry SR. Application of silicon photomultipliers to positron emission tomography. Ann Biomed Eng. 2011;39(4):1358-1377. doi:10.1007/s10439-011-0266-9

[239] Ullah MN, Pratiwi E, Cheon J, Choi H, Yeom JY. Instrumentation for Time-of-Flight Positron Emission Tomography. Nucl Med Mol Imaging. 2016;50(2):112-22.

[240] Zhang J, Maniawski P, Knopp MV. Performance evaluation of the next generation solid-state digital photon counting PET/CT system. EJNMMI Res. 2018 Nov 6;8(1):97. doi: 10.1186/s13550-018-0448-7. PMID: 30402779; PMCID: PMC6219999.

[241] Zhang J, Knopp MI, Knopp MV. Sparse Detector Configuration in SiPM Digital Photon Counting PET: a Feasibility Study. Mol Imaging Biol. 2019;21(3):447-53.

[242] Ferri A, Acerbi F, Gola A, Paternoster G, Piemonte C, Zorzi N. A comprehensive study of temperature stability of Silicon PhotoMultiplier. Journal of Instrumentation. 2014;9(06):P06018-P.M.

[243] Ivanovs V, Gushchin S, Ivanovs V, Fjodorovs V, Kuznecovs D, Loutchanski A, et al. Temperature stabilization of SiPM-based gamma-radiation scintillation detectors. RAD Association Journal. 2019;3.

[244] Gong P, Han Z, Gao L, Wang P, Zhang J, Tang X. Development of a SiPM-based CsI(Tl) spectrometer with gain stabilisation designs for rapid temperature variations. Nuclear Instruments and Methods in Physics Research Section A: Accelerators, Spectrometers, Detectors and Associated Equipment. 2019;927:301-305.

[245] Eigen G. Gain Stabiliz,m ation of SiPMs and Afterpulsing. Journal of Physics: Conference Series. 2019;1162:12013.

[246] Shimazoe K, Uenomachi M, Mizumachi Y, Takahashi H, Masao Y, Shoji Y, et al. Double Photon Emission Coincidence Imaging using GAGG-SiPM pixel detectors. Journal of Instrumentation. 2017;12(12):C12055-C.

[247] Babichev EA, Baru SE, Grigoriev DN, Oleynikov VP, Porosev VV, Savinov GA, et al. SiPM based photon counting detector for scanning digital radiography. Journal of Instrumentation. 2015;10(03):C03002-C.

[248] Slomka PJ, Pan T, Berman DS, Germano G. Advances in SPECT and PET Hardware. Progress in Cardiovascular Diseases. 2015;57(6):566-78.

[249] Yoon HS, Ko GB, Kwon SI, Lee CM, Ito M, Chan Song I, Lee DS, Hong SJ, Lee JS. Initial results of simultaneous PET/MRI experiments with an MRI-compatible silicon photomultiplier PET scanner. J Nucl Med. 2012 Apr;53(4):608-14. doi: 10.2967/jnumed.111.097501. Epub 2012 Mar 13. PMID: 22414638.

[250] Schaart D, Dam H, Seifert S, Vinke R, Dendooven P, Loehner H, et al. A novel, SiPM-array-based, monolithic scintillator detector for PET. Physics in medicine and biology. 2009;54:3501-12.

[251] Wagatsuma K, Miwa K, Sakata M, Oda K, Ono H, Kameyama M, et al. Comparison between new-generation SiPM-based and conventional PMT-based TOF-PET/CT. Physica Medica. 2017;42:203-10.

[252] Amirrashedi M, Sarkar S, Ghafarian P, Hashemi Shahraki R, Geramifar P, Zaidi H, et al. NEMA NU-4 2008 performance evaluation of Xtrim-PET: A prototype SiPM-based preclinical scanner. Med Phys. 2019;46(11):4816-25.

[253] Kwon SI, Lee JS, Yoon HS, Ito M, Ko GB, Choi JY, Lee SH, Chan Song I, Jeong JM, Lee DS, Hong SJ. Development of small-animal PET prototype using silicon photomultiplier (SiPM): initial results of phantom and animal imaging studies. J Nucl Med. 2011 Apr;52(4):572-9. doi: 10.2967/jnumed.110.079707. Epub 2011 Mar 18. PMID: 21421723.

[254] Sånchez F, Orero A, Soriano A, Correcher C, Conde P, González A, et al. ALBIRA: a small animal PET/SPECT/CT imaging system. Med Phys. 2013;40(5):051906.

[255] González AJ, Aguilar A, Conde P, Hernandez L, Sånchez F, Moliner L, et al., editors. Next generation of the Albira small animal PET based on high density SiPM arrays. 2015 IEEE Nuclear Science Symposium and Medical Imaging Conference (NSS/MIC); 2015 31 Oct.-7 Nov. 2015.

[256] Castro IF, Soares AJ, Moutinho LM, Ferreira MA, Ferreira R, Combo A, et al. Characterization of a small CsI(Na)-WSF-SiPM gamma camera prototype using ^{99m}Tc. Journal of Instrumentation. 2013;8(03):C03008-C.

[257] David S, Fysikopoulos E, Kalyvas N. Evaluation of a small field of view SiPM array detector based on a LGSO:Ce pixellated scintillator. Physica Medica. 2016;32:312.

[258] Hamamatsu. MPPCs for precision measuremnet 2020 [Available from: https://www.hamamatsu.com/eu/en/product/optical-sensors/mppc/index.html]

[259] Duara A, Lapington JS, Williams JOD, Leach SA, Ross D, Rawlins T. Experimental and extraction procedure for the electrical characterisation of silicon photomultiplier detectors. Nuclear Instruments and Methods in Physics Research Section A: Accelerators, Spectrometers, Detectors and Associated Equipment. 2020;979:164483.

[260] Meerstetter engineering. TEC Controllers, Temperature regulators for Peltier elements and resistive heaters 2020 [Available from: https://www.meerstetter.ch/products/tec-controllers.

[261] Photek. Pulse laser, LPG-405 2020 [Available from: https://www.photek.co.uk/products/pulsed-laser.html.

[262] Thorlabs. Absorptive and Reflective Neutral Density Filter Kits 2020 [Available from: https://www.thorlabs.com/newgrouppage9.cfm?objectgroup_id=689].

[263] TeledyneLecroy. LeCroy HDO4000 Series Oscilloscope 2020 [Available from: https://teledynelecroy.com/oscilloscope/hdo4000a-high-definition-oscilloscopes].

[264] Bruschini C, Homulle H, Antolovic IM, Burri S, Charbon E. Single-photon avalanche diode imagers in biophotonics: review and outlook. Light Sci Appl. 2019 Sep 18;8:87. doi: 10.1038/s41377-019-0191-5. Erratum in: Light Sci Appl. 2020 Jan 28;9:12. PMID: 31645931; PMCID: PMC6804596.

[265] Acerbi F, Gundacker S. Understanding and simulating SiPMs. Nuclear Instruments and Methods in Physics Research Section A: Accelerators, Spectrometers, Detectors and Associated Equipment. 2019;926:16-35.

[266] Ramilli M. Characterization of SiPM: Temperature dependencies. 2008; 2467-70.

[267] Otte AN, Garcia D, Nguyen T, Purushotham D. Characterization of three high efficiency and blue sensitive silicon photomultipliers. Nuclear Instruments and Methods in Physics Research Section A: Accelerators, Spectrometers, Detectors and Associated Equipment. 2017;846:106-125.

[268] Du J, Bai X, Gola A, Acerbi F, Ferri A, Piemonte C, et al. Performance of a high-resolution depth-encoding PET detector module using linearly-graded SiPM arrays. Physics in Medicine & Biology. 2018;63(3):035035.

[269] Slawomir S. Piatek, Physics and Operation of a MPPC, Hamamatsu Corporation & New Jersey Institute of Technology, 2014.

[270] Baszczyk M, Dorosz P, Głąb S, Kucewicz W, Mik Ł, Sapor M. Silicon Photomultiplier Gain Compensation Algorithm in Multidetector Measurements. Metrology and Measurement Systems. 2013;20.

[271] Boschini MJ, Consolandi C, Fallica PG, Gervasi M, Grandi D, Mazzillo M, et al. Electrecal charactrization of SiPM as a function of test frequency and temperature. Astroparticle, Particle, Space Physics and Detectors for Physics Applications. Radiation Interaction, Detectors and Medical Physics Applications. Volume 7: World Scientific; 2012. p. 663-75.

[272] Du J, Yang Y, Bai X, Judenhofer MS, Berg E, Di K, et al. Characterization of Large-Area SiPM Array for PET Applications. IEEE Trans Nucl Sci. 2016;63(1):8-16.

[273] Jiang J, Jia J, Zhao T, Liang K, Yang R, Han D. Recovery Time of Silicon Photomultiplier with Epitaxial Quenching Resistors. Instruments. 2017; 1(1):5.

[274] Gundacker S, Acerbi F, Auffray E, Ferri A, Gola A, Nemallapudi MV, et al. State of the art timing in TOF-PET detectors with LuAG, GAGG and LYSO scintillators of various sizes coupled to FBK-SiPMs. Journal of Instrumentation. 2016;11(08):P08008-P.

[275] Gundacker S, Turtos RM, Auffray E, Paganoni M, Lecoq P. High-frequency SiPM readout advances measured coincidence time resolution limits in TOF-PET. Physics in Medicine & Biology. 2019;64(5):055012.

[276] Derenzo SE, Choong W-S, Moses WW. Fundamental limits of scintillation detector timing precision. Physics in Medicine and Biology. 2014;59(13):3261-86.

[277] Renschler M, Painter W, Bisconti F, Haungs A, Huber T, Karus M, et al. Characterization of Hamamatsu 64-channel TSV SiPMs. Nuclear Instruments and Methods in Physics Research Section A: Accelerators, Spectrometers, Detectors and Associated Equipment. 2018;888:257-67.

[278] Valdes Olmos RA, Vidal-Sicart S. Introducing new perspectives in radioguided intervention. Clinical and Translational Imaging. 2016;4(5):307-11.

[279] Van Oosterom MN, Rietbergen DDD, Welling MM, Van Der Poel HG, Maurer T, Van Leeuwen FWB. Recent advances in nuclear and hybrid detection modalities for image-guided surgery. Expert Review of Medical Devices. 2019;16(8):711-34.

[280] Vermeeren L, Valdes Olmos RA, Meinhardt W, Bex A, van der Poel HG, Vogel WV, et al. Intraoperative radioguidance with a portable gamma camera: a novel technique for laparoscopic sentinel node localisation in urological malignancies. Eur J Nucl Med Mol Imaging. 2009;36(7):1029-36.

[281] Van Audenhaege K, Van Holen R, Vandenberghe S, Vanhove C, Metzler SD, Moore SC. Review of SPECT collimator selection, optimization, and fabrication for clinical and preclinical imaging. Med Phys. 2015;42(8):4796-813.

[282] Giammarile F, Alazraki N, Aarsvold JN, Audisio RA, Glass E, Grant SF, et al. The EANM and SNMMI practice guideline for lymphoscintigraphy and sentinel node localization in breast cancer. Eur J Nucl Med Mol Imaging. 2013;40(12):1932-47.

[283] Mathelin C, Salvador S, Huss D, Guyonnet JL. Precise Localization of Sentinel Lymph Nodes and Estimation of Their Depth Using a Prototype Intraoperative Mini -Camera in Patients with Breast Cancer. Journal of Nuclear Medicine. 2007;48(4):623-9.

[284] Miller S, Gaysinskiy V, Shestakova I, Nagarkar V. Recent advances in columnar CsI(TI) scintillator screens. Proc SPIE. 2005;5923.

[285] Advatech. Radiation Detection/Imaging and Photonics 2020 [Available from: https://www.advatech-uk.co.uk/index.html].

[286] Occhipinti M, Busca P, Butt AD, Cozzi G, Fiorini C, Perali I, et al., editors. A compact SiPM photodetector array for SPECT applications. 2014 IEEE Nuclear Science Symposium and Medical Imaging Conference (NSS/MIC); 2014 8-15 Nov. 2014.

[287] Jeong M, Hammig M. Development of hand-held coded-aperture gamma ray imaging system based on GAGG(Ce) scintillator coupled with SiPM array. Nuclear Engineering and Technology. 2020;52(11):2572-80.

[288] Yamamoto S, Watabe H, Kanai Y, Kato K, Hatazawa J. Development of an ultrahigh-resolution SiPM-based dual-head GAGG coincidence imaging system. Nuclear Instruments and Methods in Physics Research Section A: Accelerators, Spectrometers, Detectors and Associated Equipment. 2013;703:183-9.

[289] Seitz B, Rivera NC, Stewart AG. Energy Resolution and Temperature Dependence of Ce:GAGG Coupled to 3mm × 3mm Silicon Photomultipliers. IEEE Trans Nucl Sci. 2016;63(2):503-8.

[290] Hamamatsu. X-ray scintillator 2020 [Available from: https:https://www.hamamatsu.com/eu/en/product/optical-sensors/x-ray-sensor/scintillator-plate/index.html].

[291] Roncali E, Stockhoff M, Cherry SR. An integrated model of scintillator-reflector properties for advanced simulations of optical transport. Physics in medicine and biology. 2017;62(12):4811-30.

[292] Weele D, Schaart D, Dorenbos P. Picosecond Time Resolved Studies of Photon Transport Inside Scintillators. IEEE Trans Nucl Sci. 2015;62:1-11.

[293] Hubbell, J.H. and Seltzer, S.M. (2004), Tables of X-Ray Mass Attenuation Coefficients and Mass Energy-Absorption Coefficients (version 1.4). [Online] Available: http://physics.nist.gov/xaamdi [2020, October]. National Institute of Standards and Technology, Gaithersburg, MD.

[294] Aldrich Silicon. Silicon oil 2020 [Available from: https://www.sigmaaldrich.com/united-kingdom.html].

[295] Betz M. Read Trc file.py 2015 [Available from: https://github.com/yetifrisstlama/readTrc/blob/master/readTrc.py].

[296] Ovechkina EE, Gaysinskiy V, Miller SR, Brecher C, Lempicki A, Nagarkar VV. Multiple doping of CsI:Tl crystals and its effect on afterglow. Radiat Meas. 2007;42(4-5):541-4.

[297] Lucchini MT, Babin V, Bohacek P, Gundacker S, Kamada K, Nikl M, et al. Effect of Mg2+ ions co-doping on timing performance and radiation tolerance of Cerium doped Gd3Al2Ga3O12 crystals. Nuclear Instruments and Methods in Physics Research Section A: Accelerators, Spectrometers, Detectors and Associated Equipment. 2016;816:176-83.

[298] Yeom JY, Yamamoto S, Derenzo SE, Spanoudaki VC, Kamada K, Endo T, et al. First Performance Results of Ce:GAGG Scintillation Crystals With Silicon Photomultipliers. IEEE Trans Nucl Sci. 2013;60:988.

[299] Bocci V, Chao D, Chiodi G, Faccini R, Ferroni F, Lunadei R, et al. Dependence of the energy resolution of a scintillating crystal on the readout integration time. Journal of Instrumentation. 2012;7. 3.

[300] Bora VJS. Photon statistics in scintillation crystals. 2015.

[301] Jambi L, Lees J, Bugby S, Tipper S, Alqahtani M, Perkins A. Evaluation of XRI-UNO CdTe detector for nuclear medical imaging. Journal of Instrumentation. 2015;10:P06012-P.

[302] Hwang AB, Iwata K, Hasegawa BH, editors. Simulation of depth of interaction effects for pinhole SPECT. 2001 IEEE Nuclear Science Symposium Conference Record (Cat No01CH37310); 2001 4-10 Nov. 2001.

[303] Bettiol M, Preziosi E, Cinti MN, Borrazzo C, Fabbri A, Cassano B, et al. A Depth-of-Interaction encoding method for SPECT monolithic scintillation detectors. Journal of Instrumentation. 2016;11(12):C12054-C.

[304] Green MV, Seidel J, Vaquero JJ, Jagoda E, Lee I, Eckelman WC. High resolution PET, SPECT and projection imaging in small animals. Computerized Medical Imaging and Graphics. 2001;25(2):79-86.

[305] Pani R, Bettiol M, Preziosi E, Borrazzo C, Pellegrini R, Gonzålez AJ, et al. A Novel Method for $\gamma -$ photons Depth-of-Interaction Detection in Monolithic Scintillation Crystals. IEEE Trans Nucl Sci. 2016;63(5):2487-95.

[306] Morrocchi M, Ambrosi G, Bisogni MG, Bosi F, Boretto M, Cerello P, et al. Depth of interaction determination in monolithic scintillator with double side SiPM readout. EJNMMI Physics. 2017;4(1):11.

[307] Soria X, Sappa AD, Hammoud RI. Wide-Band Color Imagery Restoration for RGB-NIR Single Sensor Images. Sensors (Basel). 2018;18(7):2059. Published 2018 Jun 27. doi:10.3390/s18072059.

[308] Zheng H, Cheng T, Li D, Zhou X, Yao X, Tian Y, et al. Evaluation of RGB, Color-Infrared and Multispectral Images Acquired from Unmanned Aerial Systems for the Estimation of Nitrogen Accumulation in Rice. Remote Sensing. 2018;10:824.

[309] Phillips GW. Gamma-ray imaging with Compton cameras. Nuclear Instruments and Methods in Physics Research Section B: Beam Interactions with Materials and Atoms. 1995;99(1):674-7.

[310] Fontana M, Dauvergne D, Letang JM, Ley JL, Testa E. Compton camera study for high efficiency SPECT and benchmark with Anger system. Phys Med Biol. 2017 Nov 9;62(23):8794-8812. doi: 10.1088/1361-6560/aa926a. PMID: 28994664.

[311] Omata A, Kataoka J, Fujieda K, Sato S, Kuriyama E, Kato H, Toyoshima A, Teramoto T, Ooe K, Liu Y, Matsunaga K, Kamiya T, Watabe T, Shimosegawa E, Hatazawa J. Performance demonstration of a hybrid Compton camera with an active pinhole for wide-band X-ray and gamma-ray imaging. Sci Rep. 2020 Aug 20;10(1):14064. doi: 10.1038/s41598-020-71019-5. PMID: 32820211; PMCID: PMC7441182.

[312] Sakai, M., Kubota, Y., Parajuli, R.K. et al. Compton imaging with $^{9}9m$Tc for human imaging. Sci Rep 9, 12906 (2019). https://doi.org/10.1038/s41598-019-49130-z.